CHALMERS
UNIVERSITY OF TECHNOLOGY

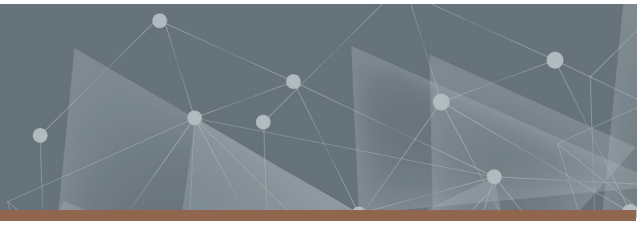

Ship radiated sound computation in a constrained domain

Master's thesis in Sound and Vibration

TOMASZ BAGINSKI

Department of Architecture and Civil Engineering

CHALMERS UNIVERSITY OF TECHNOLOGY
Gothenburg, Sweden 2023
www.chalmers.se

Master's thesis 2023

Ship radiated sound computation in a constrained domain

TOMASZ BAGINSKI

CHALMERS
UNIVERSITY OF TECHNOLOGY

Department of Architecture and Civil Engineering
Division of Applied Acoustics
Chalmers University of Technology
Gothenburg, Sweden 2023

Ship radiated sound computation in a constrained domain
TOMASZ BAGINSKI

Supervisor: Rickard Bensow,Department of Mechanics and Maritime Sciences
Examiner: Jens Forssén, Department of Civil and Environmental Engineering

Master's Thesis 2023
Department of Architecture and Civil Engineering
Division of Applied Acoustics
Chalmers University of Technology
SE-412 96 Gothenburg
Telephone +46 31 772 1000

Cover: Simulated wave propagation, calculated using FDTD

Typeset in LaTeX
Printed by Chalmers Reproservice
Gothenburg, Sweden 2023

Ship radiated sound computation in a constrained domain
Tomasz BAGINSKI
Department of Civil and Environmental Engineering
Chalmers University of Technology

Abstract

Nowadays, many computational methods are used to predict propeller-radiated noise. Nevertheless, the results from physical measurements and computer models show significant discrepancies. The difference between the results is due to the capabilities and limitations of measurement methods and simulation models. Therefore, approaches that mimic actual environments are needed. Bearing in mind that today's seas and oceans are polluted by sound, understanding the underwater sound propagation phenomenon can help set appropriate points for real-scale physical measurements and support the silent design of propellers.

The thesis purpose is to design a three-dimensional Finite Difference Time Domain model for calculating underwater sound propagation with features of fully reflective and semi-reflective boundary conditions and free space propagation. The code is implemented in Matlab and validated by different experiments and comparisons with analytical solutions. Essentially, these simulations imitate environments like open seas, shallow waters, water canals, and cavitation tunnels.

Keywords: Finite-Difference Time-Domain, Perfectly Matched Layers, underwater sound propagation, discretization, cavitation tunnel, canal, impedance, three-dimensional, propeller noise, shallow water

Acknowledgements

Firstly, I would like to thank Professor Rickard Bensow for proposing this interesting topic and for his help and support, in particular incomparable coding process aid.

I would also thank the examiner, professor Jens Forssén, for taking the time to answer my questions and provide valuable comments.

Finally, I would like to thank all the lecturers, teachers, friends and colleagues for the time spent together, the priceless teamwork and for good company during our studies.

Tomasz Baginski, Gothenburg, August 2022

List of Acronyms

Below is the list of acronyms that have been used throughout this thesis listed in alphabetical order:

ABC	Absorbing Boundary Condition
BC	Boundary Condition
CPA	Closest Point of Approach
DC	Direct Current
FDTD	Finite Difference Time Domain
FFT	Fast Fourier Transform
FWHM	Full Width at Half Maximum
PML	Perfectly Matched Layer
PSU	Practical Salinity Unit
RMS	Root Mean Square
NPML	Nearly Perfectly Matched Layer
SPL	Sound Pressure Level

Nomenclature

Below is the nomenclature of indices, sets, parameters, and variables that have been used throughout this thesis.

Indices

i,j,k	Indices for distribution
x,y,z	Indices for distribution
1,2	Indices for mediums
s	Index for sediment

Sets

v	Velocity of medium
w	Particle velocity
p	Acoustic pressure

Parameters and Variables

α	Attenuation coefficient
Δt	Time discretization step (time interval)
Δx	Spatial discretization step (spatial interval)
λ	Wavelength
ρ	Density of the main medium
σ	Static flow resistivity
τ	Typical ground surface
ϕ	Attenuation coefficient matrix

ψ	Auxiliary variable
Ω	Material porosity
A	Control coefficient
b	Mass buoyancy factor
C_r	Courant condition
c	Sound velocity
D	Force source
K	Adiabatic bulk modulus
$N_{x,y,z}$	Nodes number
N	Number of divisions
Q	Mass source
R	Reflection coefficient
w_g	Full width at half maximum
v	Particle Velocity

Contents

List of Figures

List of Tables

1

Introduction

Many methods can be used to predict the propagation of underwater acoustic waves. Wave propagation models are typically designed to solve wave equations. There are several methods for solving these equations, for example, Finite Difference, Finite Element, Parabolic Equations, Normal Mode, Energy Flux, and Fast Field Program [1].

This report discusses the Finite Difference Method (FDTD) in an underwater application. The Finite Difference Method is based on the fundamental motion equation and continuity equation. The wave equation is solved by spatial and temporal discretization. This method allows for the appliance of different boundary conditions and mimics various sea models [2]. The FDTD is a robust tool for dealing with real-scale problems in a complex environment. However, FDTD for solving complex boundary conditions requires a relatively large amount of memory and increases computational effort. Due to that fact, 2-dimensional FDTD simulations are commonly in use.

1.1 Background

Today's seas and oceans are polluted with sound. Excessive human activity generates a considerable increase in emitted sound and consequently affects marine animals' behaviour, movements, and migratory patterns [3]. The main contributors to noise pollution in the sea are ongoing vessels [4].

Cavitation of the ship propeller is generally indicated as the main noise source [5]. Currently, Currently, propeller sound can be assessed in two ways: either by using a cavitation tunnel with a hull, rudder and propeller on a modelled scale or by full-scale measurements in the open sea. However, the results from both methods deliver quite significant discrepancies. Most of all, noise levels and the general noise spectrum trends differ significantly even though the compared cavitation patterns match well [6].

Considering the differences between the results of the above methods, it is essential to gain a better understanding of the propagation of underwater sound. Such capability can help with silent design and noise reduction. As a result, the impact of human activity on the marine environment can be minimized.

1.2 Aim

The main aim of this study is to design the 3-d Finite Difference Time Domain computational method and investigate if it can be representative of propeller sound propagation physic. In particular, the tests will focus on the constrained domain by simulating environmental conditions, e.g. a cavitation channel or shallow water.

2
Theory

The following sections describe the fundamentals of the acoustic FDTD method in terms of application for underwater sound propagation. The physical environments are described and established in the numerical model. The essential properties of the 3-d FDTD approach are described as, 3-d spatial and temporal discretization, absorbing boundary conditions, ground boundary conditions and impedance boundary conditions.

2.1 FDTD

The Finite different time domain is a method introduced by Kane Yee in 1966 and used for modelling electromagnetic fields. The simulation is based on Maxwell equations, engaging finite differences as approximations to both the spatial and temporal derivatives [7]. Over the years, the FDTD has found applications in several engineering fields. For example, FDTD was adopted for different areas of acoustic, e.g. outdoor/urban acoustic, room acoustic or underwater acoustic [8],[9].
Recently, it has been shown that the FDTD method is easy to develop, which can be advantageous in designing more complex source arrangements. Moreover, the FDTD is a good tool for transient simulation and non-linear and anisotropic behaviour. The FDTD seems to be the compliant application for inhomogeneous moving media. Moreover, research proved that the FDTD methods are functional for simulating complex interactions of sound waves with various boundary conditions. Despite unprecedented advantages, the FDTD has a few flaws and limitations resulting from the simulation accuracy being dependent on the number of nodes, the distance between them and the time step. The time step is dependent on the wavelength. It is crucial, especially when considering the higher frequency of interest with shorter wavelengths, which causes an increase in calculation burden [8].

2.1.1 Fundamental Sound Propagation equations

In principle, the FDTD method includes the discretization of first-order differential equations derived from the linearized fluid dynamic equations with approximations appropriate to sound waves. It couples pressure variable p and particle velocity $\mathbf{w}$. In many studies, a common starting point for FDTD equations with moving medium in temporal derivatives is expressed as [8],[10]:

$$\frac{\partial p}{\partial t} = -\left(\mathrm{v}\cdot\nabla\right)p - K\nabla\cdot\mathrm{w} + KQ, \tag{2.1}$$

and

$$\frac{\partial \mathrm{w}}{\partial t} = -\left(\mathrm{v}\cdot\nabla\right)\mathrm{w} - \left(\mathrm{w}\cdot\nabla\right)\mathrm{v} - b\nabla p + bD, \tag{2.2}$$

where $\mathbf{v}$ is the medium velocity, K is the adiabatic bulk modulus as $K = \rho_0 c_0^2$, ρ_0 is the density of the medium and c_0 is the speed of sound, b is the mass buoyancy expressed as $b = 1/\rho_0$, and Q is mass source and D is force source. In the equations (2.1) and (2.2) the components $\mathbf{v}$ and $\mathbf{w}$ and D are presented as two-dimensional vectors. By expanding the given expression to a 3-dimensional grid the spatial z component is added. Writing out the derivatives for a three-dimensional example results as

$$\frac{\partial p}{\partial t} = -v_x\frac{\partial p}{\partial x} - v_y\frac{\partial p}{\partial y} - v_z\frac{\partial p}{\partial z} - K\frac{\partial w_x}{\partial x} - K\frac{\partial w_y}{\partial y} - K\frac{\partial w_z}{\partial z} - KQ, \tag{2.3}$$

$$\frac{\partial w_x}{\partial t} = -v_x\frac{\partial w_x}{\partial x} - v_y\frac{\partial w_x}{\partial y} - v_z\frac{\partial w_x}{\partial z} - w_x\frac{\partial v_x}{\partial x} - w_y\frac{\partial v_x}{\partial y} - w_z\frac{\partial v_x}{\partial z} - b\frac{\partial p}{\partial x} + bD_x, \tag{2.4}$$

$$\frac{\partial w_y}{\partial t} = -v_x\frac{\partial w_y}{\partial x} - v_y\frac{\partial w_y}{\partial y} - v_z\frac{\partial w_y}{\partial z} - w_x\frac{\partial v_y}{\partial x} - w_y\frac{\partial v_y}{\partial y} - w_z\frac{\partial v_y}{\partial z} - b\frac{\partial p}{\partial y} + bD_y, \tag{2.5}$$

and

$$\frac{\partial w_z}{\partial t} = -v_x\frac{\partial w_z}{\partial x} - v_y\frac{\partial w_z}{\partial y} - v_z\frac{\partial w_z}{\partial z} - w_x\frac{\partial v_z}{\partial x} - w_y\frac{\partial v_z}{\partial y} - w_z\frac{\partial v_z}{\partial z} - b\frac{\partial p}{\partial z} + bD_z. \tag{2.6}$$

The graphical representation of a 3-d spatial finite grid for an acoustic wave is shown in the figure 2.1.

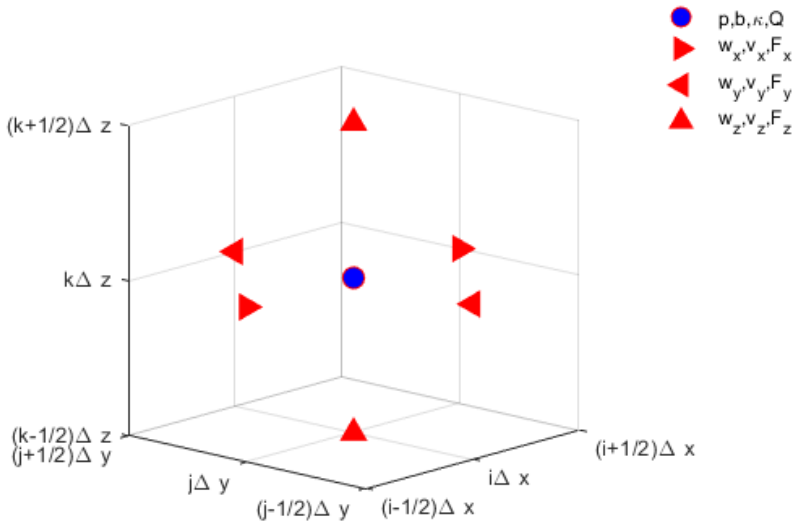

Figure 2.1: 3-d FDTD spatial staggered finite grid of pressure and velocity for acoustic wave propagation.

The way to solve the listed wave equation 3-d in space is to discretize it. In order to achieve that the FDTD method should be employed.

2.1.2 Discretization

Spatial and temporal discretizations are crucial steps in solving FDTD equations. Well-described definitions of discretization are given by Ostashev [8] or Wilson, and Liu [10] for both spatial and temporal discretization. In this section, most mathematical formulations are based on their findings.

2.1.2.1 Spatial Discretization

As reported in [8], the assumption for a spatial discretization should embrace the absence of the nonlinear terms involving the medium velocity **w**, which are well established as the starting point for a moving media. The FDTD grid for motionless media implies offsetting the acoustic velocity nodes from the pressure grid. It shows in the figure 2.1. The acoustic velocity is stored at the integer position, while the acoustic pressure is staggered by offsetting $\Delta x/2$ in the x-direction, $\Delta y/2$ in the y-direction and $\Delta z/2$ in the z-direction. By building a finite-difference grid presented in the figure 2.1, the suitable base, such as centred spatial derivatives, is ensured. Due to an approximation for the derivatives from equations (2.1),(2.2) can be evaluated. The solving process estimates each term on the right side of equations (2.1),(2.2), while the field variable of the left side is stored. Typically, each term of velocity or pressure is evaluated by averaging the two neighbouring halfway nodes of the node where the value is stored. In general, the second-order accurate, centre approximation partial derivatives are calculated as,

$$\begin{aligned}&\frac{\partial p}{\partial x}\left(\left(i+1/2\right)\Delta x, j\Delta y, k\Delta z, t\right) \simeq \\ &\quad\frac{p\left(\left(i+1\right)\Delta x, j\Delta y, k\Delta z, t\right) - p\left(i\Delta x, j\Delta y, k\Delta z, t\right)}{\Delta x},\end{aligned} \tag{2.7}$$

likewise pressure for the y and z components. For velocity it is denoted as,

$$\begin{aligned}&\frac{\partial w_x}{\partial x}\left(i\Delta x, j\Delta y, k\Delta z, t\right) \simeq \\ &\quad\frac{w_x\left(\left(i+1/2\right)\Delta x, j\Delta y, k\Delta z, t\right) - w_x\left(\left(i-1/2\right)\Delta x, j\Delta y, k\Delta z, t\right)}{\Delta x},\end{aligned} \tag{2.8}$$

$$\begin{aligned}&\frac{\partial w_y}{\partial y}\left(i\Delta x, j\Delta y, k\Delta z, t\right) \simeq \\ &\quad\frac{w_y\left(i\Delta x, \left(j+1/2\right)\Delta y, k\Delta z, t\right) - w_y\left(i\Delta x, \left(\left(j-1/2\right)\Delta y, k\Delta z, t\right)\right.}{\Delta y},\end{aligned} \tag{2.9}$$

$$\begin{aligned}&\frac{\partial w_z}{\partial z}\left(i\Delta x, j\Delta y, k\Delta z, t\right) \simeq \\ &\quad\frac{w_z\left(\Delta x, j\Delta y, \left(\left(k+1/2\right)\Delta z, t\right) - w_z\left(i\Delta x, j\Delta y, \left(\left(k-1/2\right)\Delta z, t\right)\right.\right.}{\Delta z},\end{aligned} \tag{2.10}$$

where the pressure partial derivatives $\partial p/\partial x$ are evaluated at the half-integer position of the average of two neighbouring integer positions, while the particle velocity partial derivatives $\partial v/\partial x$, $\partial v/\partial y$ and $\partial v/\partial z$, are calculated in the integer positions and averaged between half-integer nodes.
Considering scalar quantities as. e.g. b stored in a pressure grid is easy to determine as an average of two neighbouring points, for example:

$$\begin{aligned} &b\left(\left(i+1/2\right)\Delta x, j\Delta y, k\Delta z, t\right) \simeq \\ &\left(b\left(\left(i+1\right)\Delta x, j\Delta y, k\Delta z, t\right) + \left(b\left(i\Delta x, j\Delta y, k\Delta z, t\right)\right)/2. \end{aligned} \tag{2.11}$$

For evaluation of the propagation in the moving medium for the terms (2.3)-(2.6), the velocities of the moving medium are estimated in a few steps that vary based on where each quantity is stored. To estimate the average difference around $v_x\partial p/\partial x$ at $(x, y, z) = (i\Delta x, j\Delta y, k\Delta z, t)$, [8] suggests estimation of the $v_x\partial p/\partial x$ at the same node position as

$$\begin{aligned} &\left(v_x\frac{\partial p}{\partial x}\right)\left(i\Delta x, j\Delta y, k\Delta z, t\right) \simeq \\ &\frac{1}{2\Delta x}\left(v_x\left(\left(i+1/2\right)\Delta x, j\Delta y, k\Delta z, t\right)\right. \\ &\times\left(p\left(\left(i+1\right)\Delta x, j\Delta y, k\Delta z, t\right) - p\left(i\Delta x, j\Delta y, k\Delta z, t\right)\right) \\ &+ v_x\left(\left(i-1/2\right)\Delta x, j\Delta y, K\Delta z, t\right) \\ &\left.\times\left(p\left(i+1\Delta x, j\Delta y, k\Delta z, t\right) - p\left(\left(i-1\right)\Delta x, j\Delta y, k\Delta z, t\right)\right), \end{aligned} \tag{2.12}$$

where the pressure $v_x\partial p/\partial x$ is averaged at neighbouring integer half-steps, to get particle velocity v_x.
Later, the same scheme is used for $(x, y, z) = (i\Delta, j\Delta, z\Delta, t)$ to achieve $(v_x\partial w_x/\partial x)$, thus

$$\begin{aligned} &\left(v_x\frac{\partial w_x}{\partial x}\right)\left(\left(i+1/2\right)\Delta x, j\Delta y, k\Delta z, t\right) \simeq \frac{1}{4\Delta x} \\ &\left(v_x\left(\left(i+3/2\right)\Delta x, j\Delta y, k\Delta z, t\right) + v_x\left(\left(i+1/2\right)\Delta x, j\Delta y, k\Delta z, t\right)\right) \\ &\times\left(w_x\left(\left(i+3/2\right)\Delta x, j\Delta y, k\Delta z, t\right) - w_x\left(\left(i+1/2\right)\Delta x, j\Delta y, k\Delta z, t\right)\right) \\ &+\left(v_x\left(\left(i+1/2\right)\Delta x, j\Delta y, k\Delta z, t\right) + v_x\left(\left(i-1/2\right)\Delta x, j\Delta y, k\Delta z, t\right)\right) \\ &\times\left(w_x\left(\left(i+1/2\right)\Delta x, j\Delta y, k\Delta z, t\right) - w_x\left(\left(i-1/2\right)\Delta x, j\Delta y, k\Delta z, t\right)\right). \end{aligned} \tag{2.13}$$

Evaluation of the centre difference for $v_y\partial w_x/\partial y$ is handled similarly. Hence,

$$\begin{aligned} &\left(v_y\frac{\partial w_x}{\partial y}\right)\left(\left(i+1/2\right)\Delta x, j\Delta y, k\Delta z, t\right) \simeq \frac{1}{4\Delta x} \\ &\left(v_y\left(\left(i+1\right)\Delta x, \left(j+1/2\right)\Delta y, k\Delta z, t\right) + v_y\left(i+1\Delta x, \left(j+1/2\right)\Delta y, k\Delta z, t\right)\right) \\ &\times\left(w_x\left(\left(i+1/2\right)\Delta x, \left(j+1/2\right)\Delta y, k\Delta z, t\right) - w_x\left(\left(i+1/2\right)\Delta x, j\Delta y, k\Delta z, t\right)\right) \\ &+\left(v_y\left(\left(i+1\right)\Delta x, \left(j-1/2\right)\Delta y, k\Delta z, t\right) + v_y\left(i\Delta x, \left(j+1/2\right)\Delta y, k\Delta z, t\right)\right) \\ &\times\left(w_x\left(i\Delta x, \left(j+1/2\right)\Delta y, k\Delta z, t\right) - w_x\left(\left(i+1/2\right)\Delta x, \left(j-1\right)\Delta y, k\Delta z, t\right)\right). \end{aligned} \tag{2.14}$$

By using the same procedure, the expression for $v_z\partial w_x/\partial z$ can be obtained.

2.1.2.2 Temporal Discretization

This subsection treats the second discretization, namely temporal discretization. The scholars in [8] and [10], distinguish two approaches for temporal discretization. The first is based on an unstaggered-in-time grid, and the second corresponds to a staggered-in-time grid. The difference between these approaches is that the pressure and acoustic particle velocities are stored on the same time level for the unstaggered grid, while pressure and particle velocities are kept on alternating half-time steps for the staggered grid.
The main idea of the staggered grid is presented in figure 2.2. It is established on the same principle as spatial staggering.

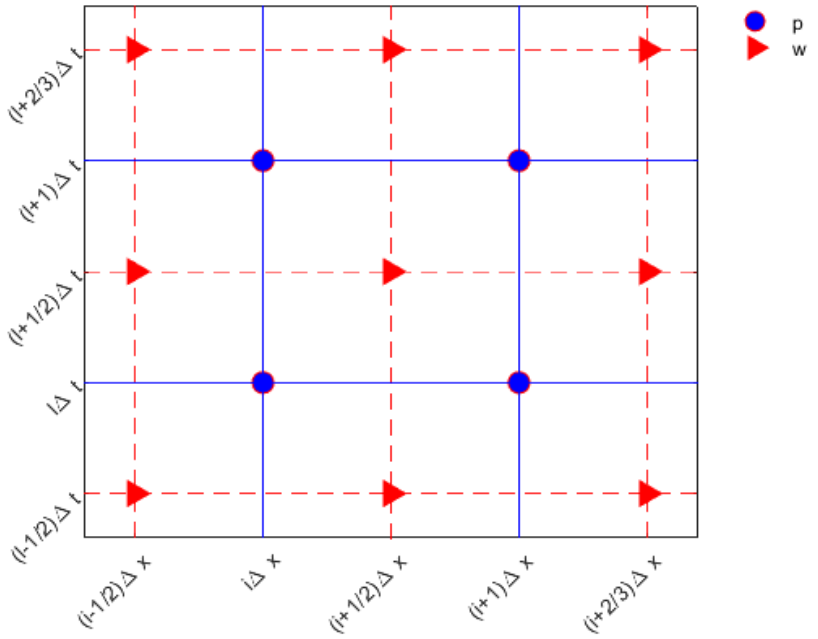

Figure 2.2: One spatial dimension FDTD; time staggered finite grid of pressure and velocity for acoustic wave propagation.

According to [8] by defending the function f_p as the rigid side of equation (2.1) and f_x, f_y, f_z as rigid component of equation (2.2). Hence,

$$\frac{\partial p\left(i\Delta x, j\Delta y, k\Delta z, t\right)}{\partial t} = f_p\left(i\Delta x, j\Delta y, k\Delta z, t\right), \tag{2.15}$$

where

$$f_p\left(x, y, z, t\right) = -\left(\mathrm{v}\cdot\nabla\right)p - K\nabla\cdot\mathrm{w} + KQ, \tag{2.16}$$

and

$$\frac{\partial w_x\left(\left(i+1/2\right)\Delta x, j\Delta y, k\Delta z, t\right)}{\partial t} = f_x\left(\left(i+1/2\right)\Delta x, j\Delta y, k\Delta z, t\right), \tag{2.17}$$

where

$$f_x\left(x, y, z, t\right) = -\left(\mathrm{v}\cdot\nabla\right)w_x - \left(\mathrm{w}\cdot\nabla\right)v_x - b\nabla p + bD_x. \tag{2.18}$$

Due to the pressure variables stored at the integer nodes express as

$$\begin{aligned} &p\left(i\Delta x, j\Delta y, k\Delta z, (l+1)\,\Delta t\right) \simeq \\ &\quad p\left(i\Delta x, j\Delta y, k\Delta z, l\Delta t\right) + \Delta t f_p\left(i\Delta x, j\Delta y, k\Delta z, (l+1/2)\,\Delta t\right) \end{aligned} \tag{2.19}$$

where $t = l\Delta$ for the pressure field, while for the particle velocity components $t = (l + 1/2)$. The velocity fields in 3-d space are represented by the following equations

$$\begin{aligned} &w_x\left((i+1/2)\,\Delta x, j\Delta y, k\Delta z, (l+1/2)\,\Delta t\right) \simeq \\ &\quad w_x\left((i+1/2)\,\Delta x, j\Delta y, k\Delta z, (l-1/2)\,\Delta t\right) + \Delta t f_x\left((i+1/2)\,\Delta x, j\Delta y, k\Delta z, l\Delta t\right), \end{aligned} \tag{2.20}$$

$$\begin{aligned} &w_y\left(i\Delta x, (j+1/2)\,\Delta y, k\Delta z, (l+1/2)\,\Delta t\right) \simeq \\ &\quad w_y\left(i\Delta x, (j+1/2)\,\Delta y, k\Delta z, (l-1/2)\,\Delta t\right) + \Delta t f_y\left(i\Delta x, (j+1/2)\,\Delta y, k\Delta z, l\Delta t\right), \end{aligned} \tag{2.21}$$

and

$$\begin{aligned} &w_z\left(i\Delta x, j\Delta y, (k+1/2)\,\Delta z, (l+1/2)\,\Delta t\right) \simeq \\ &\quad w_z\left(i\Delta x, j\Delta y, (k+1/2)\,\Delta z, (l-1/2)\,\Delta t\right) + \Delta t f_z\left(i\Delta x, j\Delta y, (k+1/2)\,\Delta z, l\Delta t\right). \end{aligned} \tag{2.22}$$

When considering a moving medium the equations mentioned above are abbreviated to the following form

$$W_{l+1/2} = W_{l-1/2} + \Delta t \dot{W}\left(P_l, W_l\right), \tag{2.23}$$

and

$$P_{l+1} = P_l + \Delta t \dot{P}_{l+1/2}\left(P_{l+1/2}, W_{l+1/2}\right). \tag{2.24}$$

The derived equations for moving medium represent the staggering leapfrog approach. However, this scheme does not provide an explicit update for the acoustic field at all time steps. In [8] and [10] some alternative solution models are performed, such as the Aldridge method or Heun's method. However, the most straightforward to implement is the unstaggered leapfrog method. As mentioned before, the unstaggered method is characterized by saving the pressure and particle velocity using the same time level. The concept of unstaggered method presented in figure 2.3.

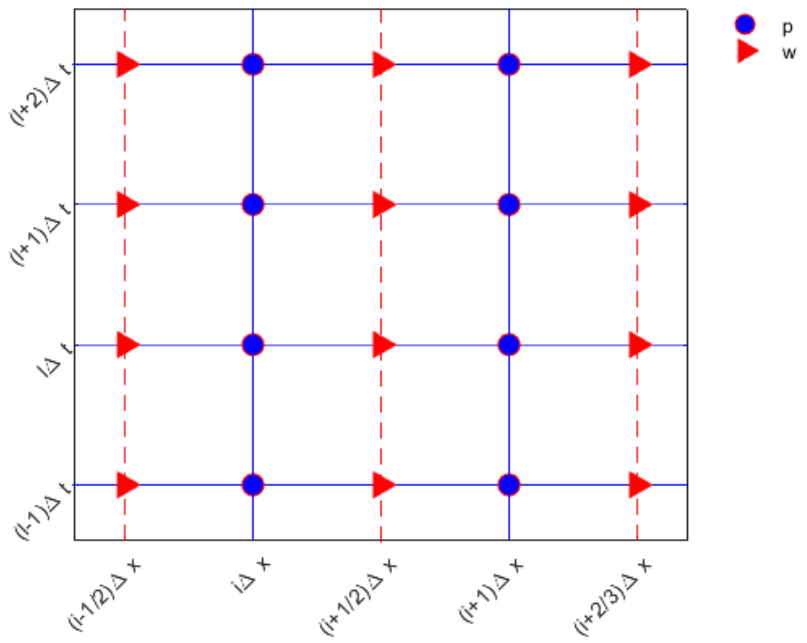

Figure 2.3: One spatial dimension FDTD time unstaggered finite grid of pressure and velocity for acoustic.

The unstaged leapfrog method centres finite differences over two-time integer step intervals. Hence, the updating equations describes as:

$$W_{l+1} = W_{l-1} + 2\Delta t \dot{W}_l \left(P_l, W_l\right), \tag{2.25}$$

$$P_{l+1} = P_{l-1} + 2\Delta t \dot{P}_l \left(P_l, W_l\right). \tag{2.26}$$

The solution for these equations is forward to $t = (l+1)\Delta t$. The pressure and particle velocity from time step $t = (l-1)\Delta t$ can be overwritten with the new values, while the solution for $t = l\Delta t$ needs to keep for the next time step. Due to this, the unstaggered leapfrog approach uses twice the memory of the staggering leapfrog method.

2.1.3 Courant condition

With a focus of to ensure numerical stability and sufficient simulation results, the introduction of an appropriate Courant condition is essential. Consequently, the Courant value C should be governed to $C < 1$[8]. However, [11] suggests setting the Courant number at 1 to minimalize the phase error of sound propagation along the diagonal of square cells. In [8], the Courant condition itself is defined as :

$$C = \frac{c_0 \Delta t}{\Delta r}, \tag{2.27}$$

where c_0 is speed of sound, Δt is time step calculated by

$$\Delta t = \frac{\Delta r}{c_0}, \tag{2.28}$$

and Δr is grid spacing and established as follows

$$\Delta r = \frac{1}{\sqrt{(\Delta x)^{-2} + (\Delta y)^{-2} + (\Delta z)^{-2}}}, \tag{2.29}$$

where Δx is a spartial step size in x direction, Δy and Δz are steps in y and z respectively. Spatial step evaluation needs to be adjusted for the maximum frequency of interest to obtain the wavelength of maximum frequency. The wavelength is obtained from

$$\lambda = \frac{c_0}{f_{max}}, \tag{2.30}$$

where f_{max} is the maximum frequency of interest. Therefore the spatial step size is calculated according to the following formula:

$$\Delta x = \frac{\lambda}{N}, \tag{2.31}$$

where N denotes the division per wavelength, this coefficient governs the accuracy of the simulation. In [11], the advised minimum N=10 is the minimum value for lowest-order discretization.
When moving medium is applied the Courant condition requires additional adaptation. Assuming speed of flow medium speed v the down-flow direction is $u_+ = u + v$ and up-flow describes $u_- = u - v$. Since the wavelength is smaller in the up-flow propagation the equation (2.30) should be provided for the wavelength in the up-flow direction and then applied the same procedures as equation (2.31) presents. The time step should be reduced to ensure simulation stability regarding the application of different materials, e.g. porous medium [11].

2.1.4 Ground/ Sediment Medium

One of the FDTD simulation features is the possibility of simulating different objects' properties. In principle, such objects' density or bulk modulus varies from the primary propagation medium. Hence, this results in impedance changes and partial reflection from the object's surface. An example of such a state condition would be the ground or seabed. By adjusting the tortuosity and porosity of the simulated material, the ground medium can be programmed using the bulk modulus and density. The ground layer is derived from a rigid-frame porous media model. As a first step, the bulk modulus is adjusted for the bulk modulus matrix that includes the properties of the sediment layer. The following equation shows the dependencies [8], [10] and [22]

$$K_0 = \frac{P_0}{\Omega}, \tag{2.32}$$

where the P_0 is ambient pressure and Ω denotes the porosity. In adition, the mass buoyancy factor b_0 has to be adjusted as well,

$$b_0 = \frac{\Omega}{\alpha\rho_0} = \frac{1}{\sigma_0\tau_0}, \tag{2.33}$$

where α is tortuosity, ρ_0 is sediment density, σ is static flow resistivity and τ_0 represents typical ground surface.
It results in a new bulk modulus K_0 for the pressure equation

$$\frac{\partial p}{\partial t} = -K_0 \frac{\partial w_x}{\partial x} - K_0 \frac{\partial w_y}{\partial y} - K_0 \frac{\partial w_z}{\partial z}, \tag{2.34}$$

and for the velocity equations

$$\frac{\partial w_x}{\partial t} = -b \frac{\partial p}{\partial x} - \frac{1}{\tau_0} w_x, \tag{2.35}$$

$$\frac{\partial w_y}{\partial t} = -b \frac{\partial p}{\partial y} - \frac{1}{\tau_0} w_y, \tag{2.36}$$

$$\frac{\partial w_z}{\partial t} = -b \frac{\partial p}{\partial z} - \frac{1}{\tau_0} w_z. \tag{2.37}$$

The $1/\tau_0 \cdot \mathbf{w}$ is added in all velocity equations, which expresses the loss term. When simulating the ground surface propagation, some additional adjustment has to be provided by increasing the time step. For example, the time step should be reduced with a factor of $\sqrt{3/2}$ to ensure the numerical stability due to a shorter wavelength in the ground medium [11].

2.1.5 Perfectly Matched Layers

The aim of Absorbing Boundary Condition (ABC) is to absorb the incident wave and reduce the reflections from the absorbing region. Over the decades, various ABC methods were developed, for simulating open boundary conditions or infinite domains, e.g. Liao's ABC [12] or Mur's ABC [13]. However, past research showed flaws in those methods. Therefore, the PML approach performs better results. The PML are artificial absorbing layers used in FDTD simulation to mimic the infinite space condition. Introduced by Berenger in 1994 for the first time [13]. The PML can be considered as an ABC, the exception between absorbing material and PML is that PLM technically does not reflect incoming waves due to impedance matching and uses an unnaturally high attenuation coefficient. Technically, the non-reflective PML region causes some reflection due to the discontinuity of the attenuation coefficient at the PML/non-PML interface and introduces some numerical reflections. The research in [9], suggests an alternative type of PML method, namely a Nearly Perfectly Matched Layer (NPML) for acoustic wave modelling. The 3-d NPML approach uses fewer auxiliary variables and fewer extraordinary differential equations. The NPML formulation shows advantages over the standard complex stretched coordinate. As result, the computational effort is lower for the NPML approach. The NPML region for the 3-d acoustic wave equation in the time domain is achieved by a set of equations presented below. The update equations for the velocity components in 3-d are obtained from the formulas

$$\frac{\partial w_x}{\partial t} = -b \frac{\partial \psi_{p_x}}{\partial x}, \tag{2.38}$$

$$\frac{\partial w_y}{\partial t} = -b\frac{\partial \psi_{p_y}}{\partial y}, \tag{2.39}$$

$$\frac{\partial w_z}{\partial t} = -b\frac{\partial \psi_{p_z}}{\partial z}, \tag{2.40}$$

where the ψ is auxiliary variable, expressed as

$$\frac{\partial \psi_{w_x^x}}{\partial t} = \frac{\partial \psi_{w_x}}{\partial t} - \phi_x \psi_{w_x^x}, \tag{2.41}$$

$$\frac{\partial \psi_{w_y^y}}{\partial t} = \frac{\partial \psi_{w_y}}{\partial t} - \phi_x \psi_{w_y^y}, \tag{2.42}$$

$$\frac{\partial \psi_{w_z^z}}{\partial t} = \frac{\partial \psi_{w_z}}{\partial t} - \phi_z \psi_{w_z^z}. \tag{2.43}$$

Then, the pressure equation is updated by

$$\frac{\partial p}{\partial t} = -K\frac{\psi_{v_x^x}}{\partial x} - K\frac{\psi_{v_y^y}}{\partial y} - K\frac{\psi_{v_z^z}}{\partial z} - KQ, \tag{2.44}$$

and the pressure auxiliary variables are prepared for the next simulation iteration

$$\frac{\partial \psi_p}{\partial t} = \frac{\partial \psi_{p^x}}{\partial t} - \phi_x \psi_p, \tag{2.45}$$

$$\frac{\partial \psi_p}{\partial t} = \frac{\partial \psi_{p^y}}{\partial t} - \phi_y \psi_p, \tag{2.46}$$

$$\frac{\partial \psi_p}{\partial t} = \frac{\partial \psi_{p^z}}{\partial t} - \phi_z \psi_p. \tag{2.47}$$

The ϕ variable represents the attenuation coefficient matrix for the NPML region. The value of the matrix is 0 zero outside the NPML region, while for NPML region decay should increase gradually through the NPML thickness to the domain boundaries.

2.2 Impedance

Acoustic impedance Z is a ratio between pressure and particle velocity. It can be completed for particular materials or mediums according to

$$Z = \rho_m c_m, \tag{2.48}$$

where ρ_m is the density of the given material and c_m is the speed of sound in the material. The acoustic reflection coefficient is needed to evaluate the Reflection coefficient between two different mediums. It is established by

$$R = \frac{Z_1 - Z_2}{Z_1 + Z_2}, \tag{2.49}$$

where Z_1 is the acoustic impedance of the first propagation medium and Z_2 is the acoustic impedance of the second propagation medium. The reflection factor is

used to simulate boundary conditions in the FDTD simulation. Respectively the absorption coefficient is obtained as follows:

$$\alpha = \frac{I_i - I_r}{I_i}, \tag{2.50}$$

where I_i is incident energy I_t is transmitted energy.

2.2.0.1 Relative pressure

Sound pressure level (SPL) is a logarithmic measure of the effective pressure of a sound relative to a reference value

$$L_p = 20log_{10}\left(\frac{p}{p_{ref}}\right) \tag{2.51}$$

where p_{ref} is 1 μPa for water. The sound pressure level is expressed in dB.
Relative ratio between two signals can be used to compare two analytical and numerical solution it is obtain by

$$\Delta L_p = 20log_{10}\left(\frac{R_2}{R_1}\right) \tag{2.52}$$

where the R_2 is the measured signal and R_1 is reference signal.

2.3 Analytical solution for wave equation

Comparison of analytical solution of the wave equation is a crucial indicator for validation of the numerical results and simulation accuracy. The scalar acoustic wave equation is

$$\partial_t^2 p\left(x,t\right) - c^2 \Delta p\left(x,t\right) = s\left(x,t\right), \tag{2.53}$$

where $p(x,t)$ is pressure, c is speed of sound and $s(x,t)$ is sound source field. Assuming constant velocity and infinite space, for the 3d space the initiation of waves propagation is simply obtain with assumption of $s(x,t) = 0$[24]. Solution for that problem is the Green's function, for inhomogeneous acoustic wave equation is given as

$$G\left(t\right) = \frac{1}{4\pi c^2 r}\delta\left(t - \frac{r}{c}\right), \tag{2.54}$$

for distance form the source $r = \sqrt{x^2 + y^2 + z^2}$, and δ is delta function deriving the equation solution at receiver position. To achieve the analytical results of the 3-d wave equation the source $q(t)$ term should be convoluted with Green's function as follows [24],

$$p\left(t\right) = \frac{\partial}{\partial t} q\left(t\right) * G\left(t\right). \tag{2.55}$$

2.4 FDTD sound sources

The sound sources in FDTD are modelled in many ways. The FDTD method allows for modelling monopole, dipole and quadrupole sound sources. Also, different signals can be applied pulses or harmonic signals etc. Although there are two primary sources of sound in terms of physical behaviour [14].

2.4.0.1 Hard sources

Hard sources are easy to implement. However, that source type's direct pressure application on a grid is artificial and seeds some drawbacks. It demonstrates that acoustic pressure appears without principal physical cause and does not obey the laws of fluid dynamics. Since a hard source node can scatter incoming waves, it can be defined as a sound radiating boundary node whose size corresponds to the spatial sample period. However, this assumption is not explicit because boundary condition elements are not evident in hard source formulation. In addition, the equations of mass and momentum are not satisfied at the source node. Thus, it will affect undesirable low-frequency contamination for some excitation signals. Moreover, the hard source contains the strong direct current (DC) component, which is unwanted in simulation because it causes a growing solution and makes solution visualization undecipherable [14].

2.4.0.2 Soft sources

The hard source's source-scattering and low-frequency can be controlled by applying the soft source instead. In such an approach, the excitation function overlaps at the pressure node and thus generates the grid's impulse response. Also, in Yee-based schemes the source function is differentiated by the staggered update equation, causing a steep roll-off at low frequencies. Whereas for strategies based on wave equations, sound sources should be filtered. Moreover, the sound source method significantly reduces the DC component from the signal [14].

2.4.0.3 Gaussian pulse

The Gaussian pulse is designed as following formula [7],

$$f_g(t) = e^{-\left(\frac{t-d_g}{w_g}\right)^2}, \tag{2.56}$$

where t is time, d_g is temporal delay, w_g is full width at half maximum (FWHM). This expression is only a function of time, function appeared only at the temporal step Δt.

2.4.0.4 Source control factor

A monopole sound source is easily generated by injecting a source of one grid size. However, by comparing the different mesh sizes the energy in the system varies. For this reason, a physical control system should be introduced.

$$Q(n) = p_{source}(n) \cdot e^{-A\left((n_{x_{source}}-n_x)^2+(n_{y_{source}}-n_y)^2+(n_{z_{source}}-n_z)^2\right)} \tag{2.57}$$

where, A is control coefficient $n_{x_{source}}$ is position of the source in expressed in nodes for x-direction and $n_{y_{source}}$, $n_{z_{source}}$ represents source positions in the y-axis and the z-axis in nodes respectively. The variables n_x, n_y ,n_z are domain dimensions in nodes.

2.5 Vessels' sound sources

The main contributors to sea noise pollution are seagoing ships [4]. There are several sources of sound on vessels, including electric motors, propellers, diesel generators, auxiliary machinery, and water flow. In most vessels, propellers and thrusters are the principal sources of noise [15].

2.5.1 Propeller noise

The propeller sound can be described as fluctuating harmonic noise associated with blade rotation caused by cavitation phenomena. When the propeller spins, it produces thrust through pressure changes. The low-pressure region is created on the blades, which causes the water to boil without heating up. This creates an immediate pressure change. This is because liquid static pressure is reduced below liquid vapour pressure. Due to the implosion process, steam bubbles pop out and generate noise. Usually, propeller rotation boosts cavitation. The maximum speed at which cavitation does not occur is called the cavitation inception speed. [5].
In some cases, propellers can generate very high-pitched noise, called propeller singing. It is caused by the shedding frequency of the trailing edge vortices coinciding with the structural natural frequency of the trailing edge of the propeller. Audible singing appears from 10 - 1200 Hz and could be as high as 12k Hz [5].

2.6 Cavitation tunnel

Cavitation tunnels are used to obtain propeller-radiated noise and pressure pulses and to determine cavitation patterns. Since numerical simulations of ship hydrodynamics have not provided accurate results, and scale tests of the model are still in use, this experimental method focuses on the model's performance. The cavitation tunnel is a closed channel through which water circulates. In some cases, especially for larger tunnels not only the propeller but the entire propeller rudder and ship's hull assembly is placed inside the cavitation tunnel. Some cavitation tunnels have too much background noise, which results in difficulties with sound measurement and noise-making or the hydro-acoustic properties of the propeller. To handle that several dedicated hydro-acoustic tunnels have been built worldwide to allow acoustical measurements [16].

2.7 Shallow water/ Canal

As [17] states, the definition of shallow water is not standardized and depends on the interpretation and field of science that defines it. Various scientists have defined shallow water in different ways. As found in nomenclature, e.g. shallow water is taken as the portion of the sea that extends from the shore to the continental shelf break and even can reach up to 500 m depth. Regarding acoustics, the most significant feature of shallow water is having boundaries, e.g. the surface and the bottom, which results in interference, diffusing and reflection of the sound wave. The surface boundary depends on the wind, the sea roughness spectrum and the seething layer of bubbles and bubble clouds, whereas the bottom can present irregular bathymetry, sub-bottom inclusions, variable materials, layering and internal structures.Further, sound speed profiles in water columns are often downward refracting. Waterways and canals are acoustically similar to shallow water. The difference is that the depth of such objects is smaller. The surface boundary between air and water and the sea bottom boundary is the same as for shallow water conditions. Moreover, the side boundaries in waterways or canals cause reflections.

2.8 Deep sea/Open sea

As opposed to shallow water, deep water has a distinct acoustic signature. The simulation is undemanding since acoustic interactions with the sea surface or the bottom are often avoided [17].

3
Methods

This section presents the code functions performed in Matlab with simulated model environments and covers the steps of validation procedures and simulation conditions.

3.1 Code

The code was written using Matlab in order to ensure suitable conditions for four different simulation environments. These environments included a cavitation tunnel, shallow water, a canal, and a deep sea. The program was implemented to present the results in an x-z plane projection and 3-D view at multiple time intervals. The implemented program provides different BC setups in all 3-directions, with the possibility to adjust various attenuation coefficients and thicknesses for PML regions or ground/sediment layers. It is possible to perform the signal injection in two different ways, namely by using a hard source or a soft source. Pressure measurements are performed by receivers placed within the tested area, which record pressure changes. The measuring probes should not be placed too close to the acoustic source because the developing sound source could cause imprecision in the measurement. Instead, the probes should be positioned in the far field.

3.1.1 Base code

The fundamental code was implemented as described in the theory section. The covered formulations embrace spatial and temporal discretization with a leapfrog approach in 3-D. The absorbing layers condition mimics the infinite domain performed by the NPML region. Reflective boundary conditions with reflection factor $R = 1$ are realized as rigid and fully reflective. When it comes to a seabed zone or the water canals, it was modelled as a semi-reflective boundary with the possibility of adjusting impedance, with the change of speed of sound, the density and the width of the seabed layer.

3.2 Validation

Sets of simulations were employed to validate the code's correctness. Four different setups were tested: free field, rigid boundary, semi- reflective impedance boundary and PML ABC. A set of common initial values for all cases was applied as follows. The density of water was set at 1000 kg/m^3 the sound speed was adjusted to

1500 m/s^2. The confirmation process was performed in still water, where the moving medium is omitted. The sound source is placed in the domain centre for all simulations. The hydrophone positions, as well as domain sizes, were changed depending on the simulations. The Courant number is equal to 1 for all simulations besides the validation of semi-reflective impedance boundary where the Courant number is decreased to ensure the simulation stability. The limit frequency of interest is 300 Hz for the validation simulation.

3.2.1 Source

The sound source used in the validation process is a Gaussian pulse, simulated as a monopole soft source. The Gaussian pulse delay is 3 ms with full width at half maximum (FWHM) 0.75 ms. To achieve the same peak width and energy in the system for different sampling accuracies, a control stagger coefficient of 2 was initiated. Figure 3.1 shows the injected signal in the time domain and the frequency spectrum.

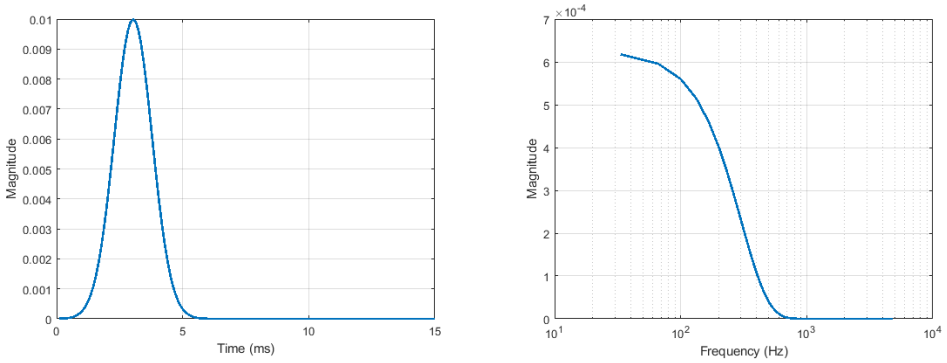

Figure 3.1: Source signal in time and frequency domain.

3.2.2 Free field

The first step of the simulation was to find which mesh size delivers accurate results with the least computational burden. The mesh size is achieved by dividing the wavelength of the frequency of interest into nodes. For this purpose, the simulation was checked in terms of acoustic propagation. For the most optimal results, as reported in [11], the four receivers were placed on the diagonal of the domain cube. The sound source was placed in the centre of the domain. Figure 3.2 shows the used domain graphically with dimensions 35 m by 35 m by 35 m and the location of the sound source and the receiver. The receiver nearest to the sound source is a reference point for the measurements, and it is 2 m away from the sound source in each of the three normal directions, which gives a direct distance from the sound source of 3.46 m. The consecutive receivers are situated 5.2 m, 6.93 m, and 8.66 m respectively away from the source.

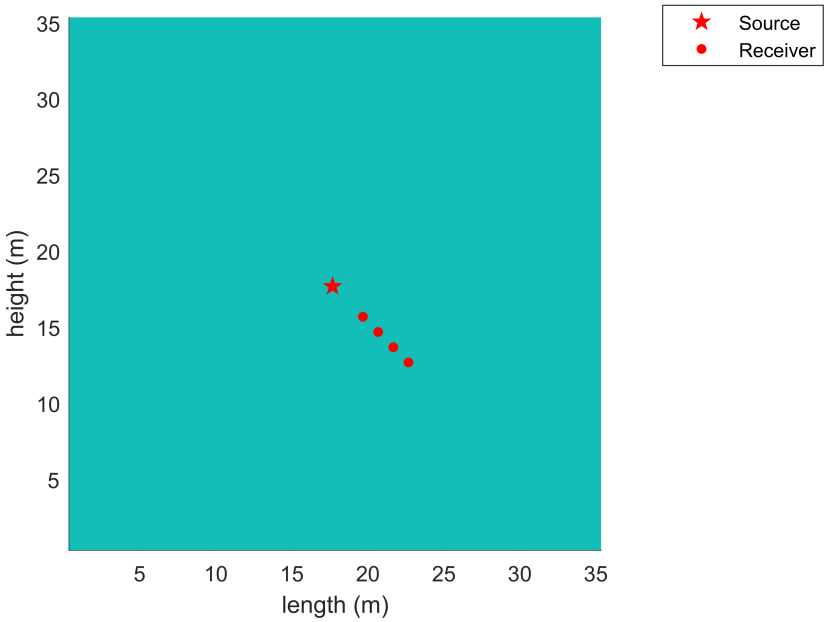

Figure 3.2: Schematic free field domain, star denotes sound source position, circles denotes receivers positions.

Subsequently, five different simulation samplings were tested concerning simulation speed propagation by dividing the wavelength by a given frequency limit. The wavelength was divided into 4, 5, 10, 15, 20, and 25 nodes. The Courant condition is the same for all tested steps and is $C_r = 1$. Figure 3.3 shows the snapshot of wave propagation in 4 different time intervals x-y projection for $\lambda/15$.

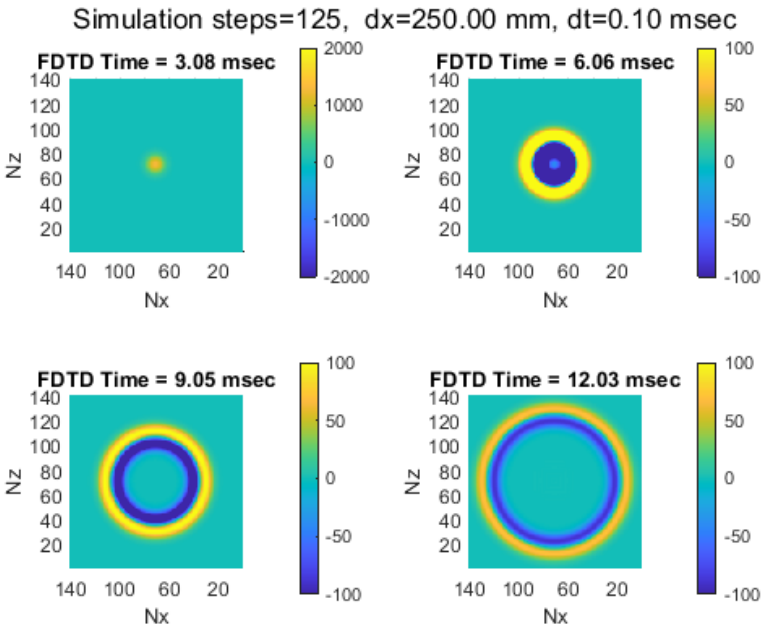

Figure 3.3: Wave propagation visualisation for λ /15.

Additionally, for the free field wave propagation validation, the 3-d analytical model and simulations with sound sources modelled as hard and soft were compared. For all tests, the receiver was located at the same distance. Two types of input signals were used in analyses: Gaussian pulses and Dirac's pulses. Figure 3.4 shows signals at the receiver position in the time and frequency domain for different models with input Gaussian pulse. Dirac pulses are shown in figure 3.5 in the time and frequency domain at the receiver's spot.

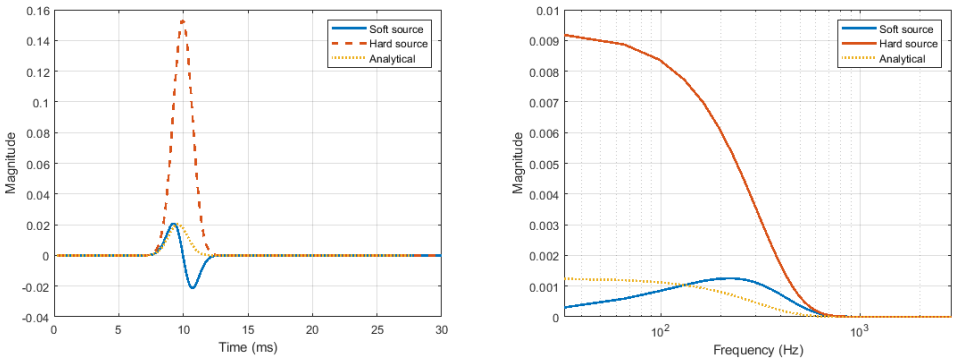

Figure 3.4: Signals at receiver positions for numerical simulation using hard and soft sources, and analytical approach using Gaussian pulses.

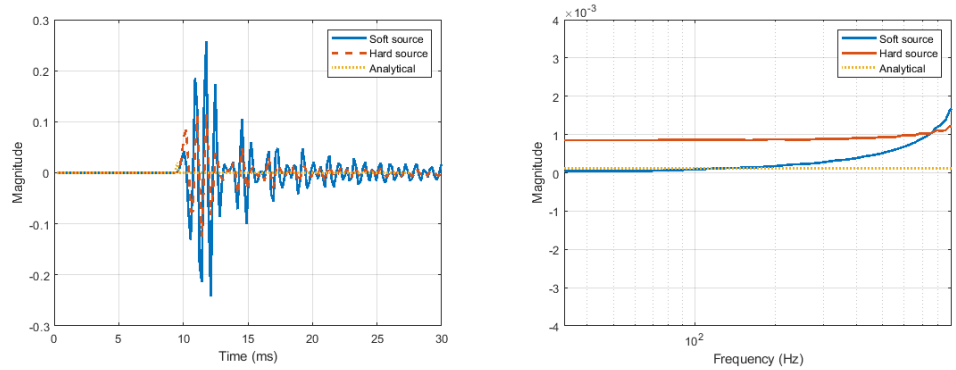

Figure 3.5: Signals at receiver positions for numerical simulation using hard and soft sources, and analytical approach using Dirac pulses.

By comparing the numerical and analytical approaches for the Gaussian pulse, it is seen that the hard source, both in frequency and time, differs significantly from the rest of the curves. The results from the numerical and analytical approaches are similar but not identical. As a result of the analytical calculations, the results have a higher energy level than the numerical simulation with a soft source, above about 100 Hz, and above 150 Hz, the numerical simulation has higher energy level than the analytical calculation.

3.2.3 Rigid boundary

The next test concerns the reflection of the acoustic wave from a rigid boundary condition. For these boundary conditions, the velocity at the boundary is 0. In other words, it ensures full reflection and corresponds to the reflection factor $R = 1$. The domain size and simulation length were chosen to capture the first wave reflection from the reflective boundary at the receiver position with no interference from the other edges. The domain dimensions are 80 m by 80 m by 40 m, and the simulation length is 30 ms. The source was located at the domain's centre, and the receiver is 10 m away in the normal direction from the source's Z-plane. The schematic arrangement is shown in figure 3.6.

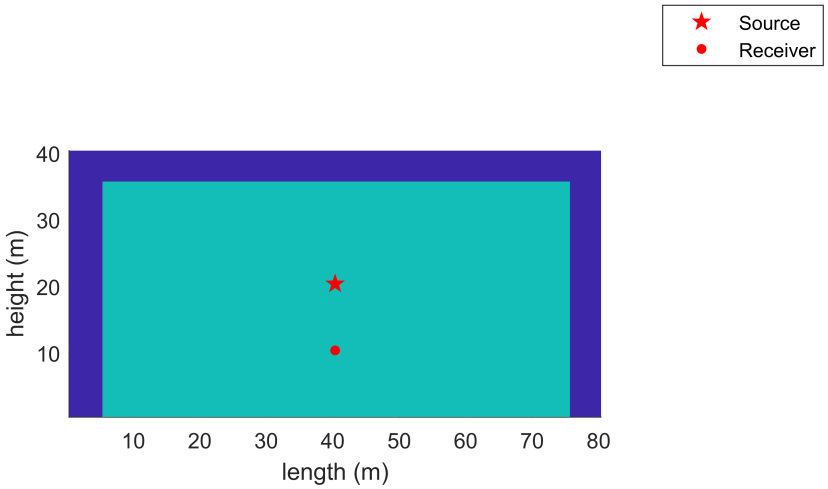

Figure 3.6: Graphics arrangement of reflection test.

Figure 3.7 shows wave propagation snapshots in four-time intervals in x-y plane projection .

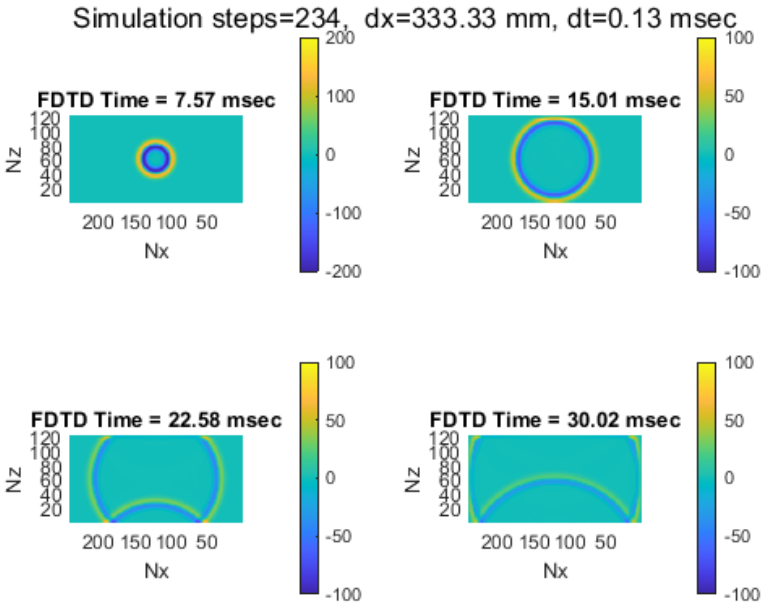

Figure 3.7: Visualisation of sound propagation in the x-z plane for a reflective boundary along the z-axis with $\lambda/15$.

3.2.4 Ground/Sediment boundary condition

The further validation procedure covers a sediment/ground boundary. The layer of sediment was applied along the z-axis on the bottom edge. The sediment thickness was set to 10 m for simulation step accuracy step $\lambda/15$. Additionally, to ensure code stability in the sediment region the C_r was multiplied by the factor 0.82. For the sediment layer having the constant density and sound velocity profile with depth growth, it draws as c_s= 1600 m/s and ρ_s= 1200 kg/m^3 [18]. The effect of hydrostatic pressure was omitted. The fully reflective surface is positioned under the sediment layer. The validation arrangement is shown in figure 3.8.

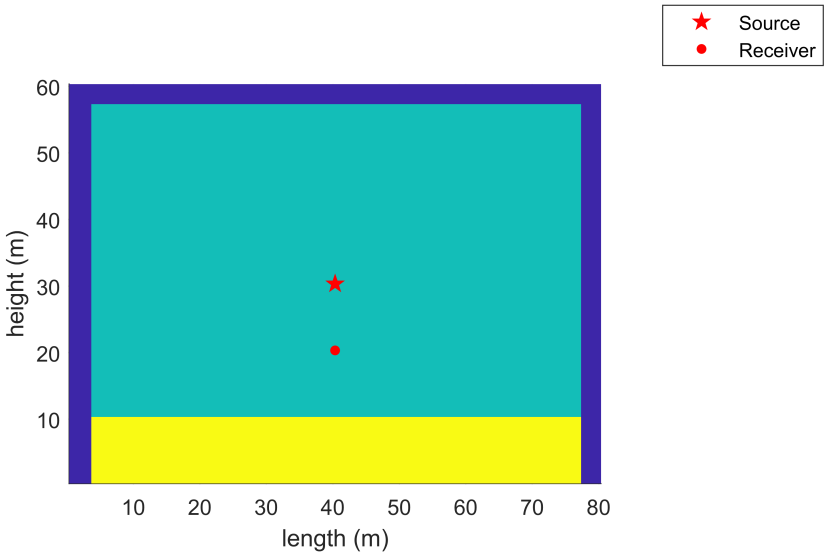

Figure 3.8: Setup of the ground/sediment b.c., the blue colour denotes the NPML region and yellow stands for the sediment thickness.

Figure 3.9 shows wave propagation snapshots in four-time intervals in x-y plane projection.

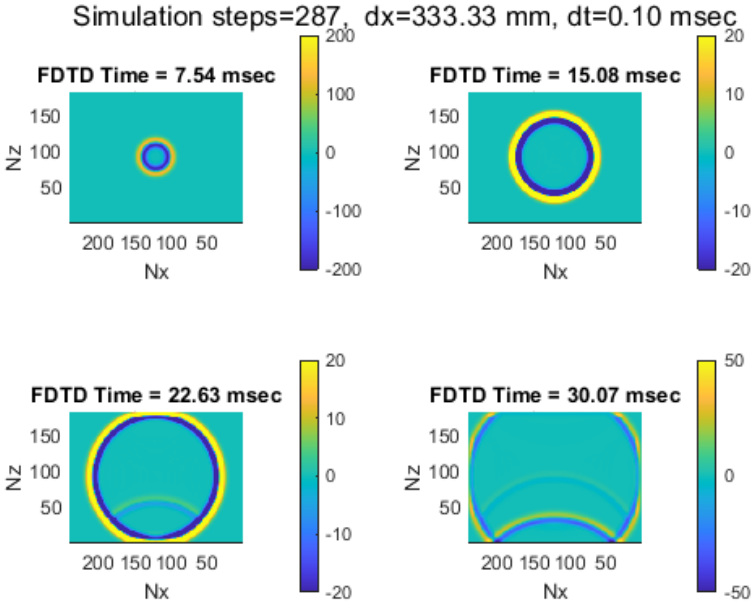

Figure 3.9: Visualisation of sound propagation in the x-z plane for sediment layer along the z-axis with $\lambda/15$.

3.2.5 Perfectly Matched Layers /Absorbing boundary condition

The last validation procedure treats Perfectly Matched Layers corresponding to the infinite domain. For this purpose a set of simulations was run. The main goal was to find out if the PML region produces any reflection, and if so, how it could be reduced. Therefore various widths and absorption coefficients were analyzed. The PML is applied on the boundary edges in all directions by setting the growing attenuation coefficient from the beginning of the PML region to the domain peripheries. Figure 3.10 presents attenuation coefficient distribution over the y-axis with maximum coefficient $\alpha_{max} = 5000$, and $PML_{width} = 20$ nodes. The PML validation procedure covers various PML regions' widths and different attenuation coefficients for $\lambda/15$.

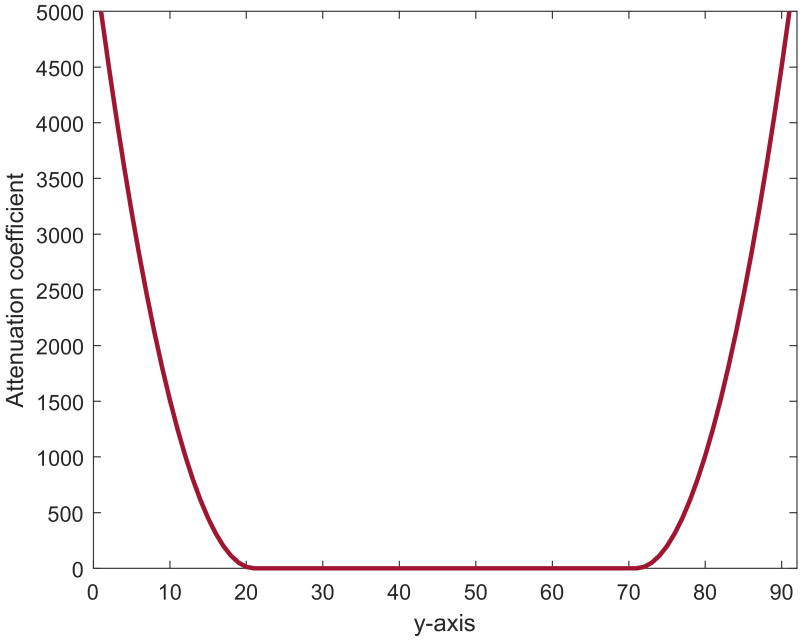

Figure 3.10: Attenuation coefficient distribution forλ /15 over the y-axis.

The schematic schematic arrangement of PML region is shown in the figure. 3.11.

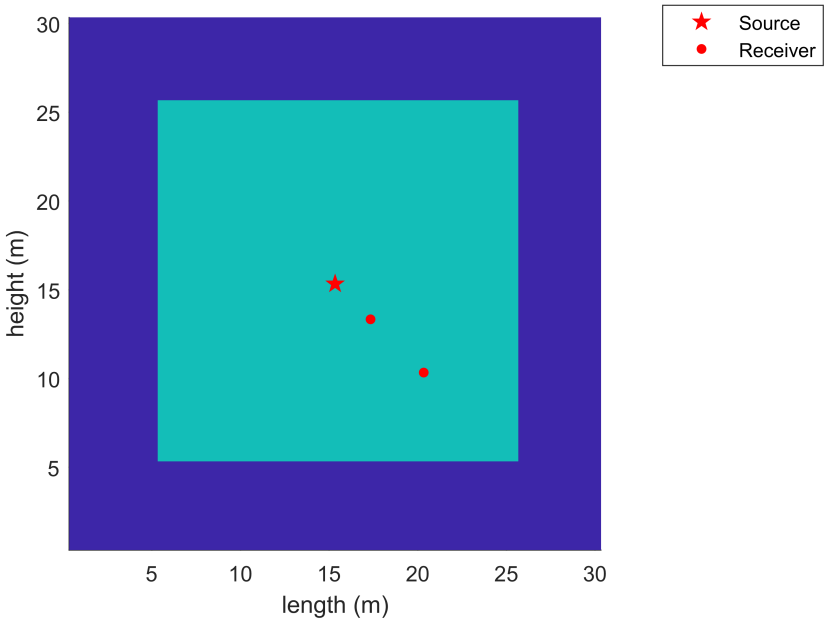

Figure 3.11: Schematic arrangement of PML validation; the blue colour denotes the PML region.

The sound source is located in the domain centre, and the receivers are positioned 3.46 m and 8.66 m away. Figure 3.12 shows wave propagation snapshots in four-time intervals in x-y plane projection used for PML validation.

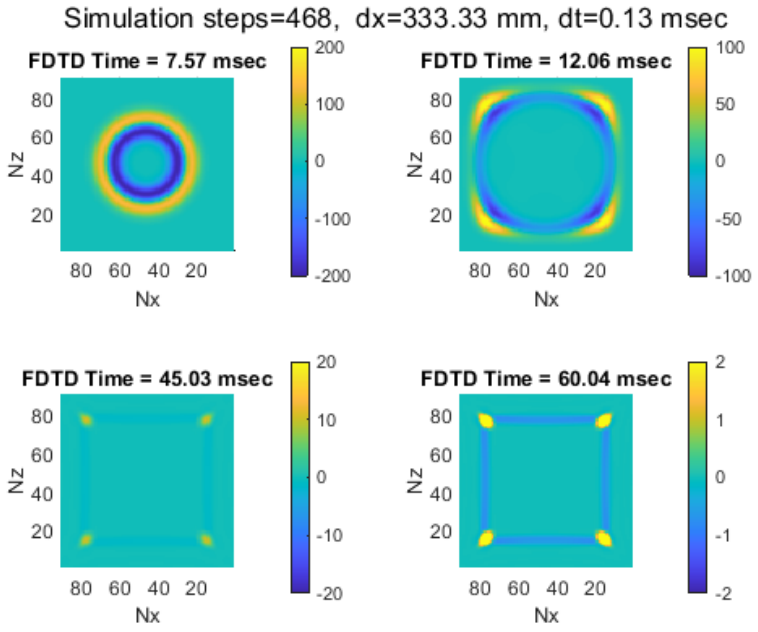

Figure 3.12: Visualisation of sound propagation in the x-z plane for PML with $\lambda/15$.

3.3 Simulation

This section describes the used parameters and conditions for replicating particular physical environments.

The first attempt was to set the maximum frequency of the limit to 2000 Hz to operate the simulation as used in [19]. The trial showed, however, that using such a high frequency while maintaining the dimensions of the domain is impossible to run and devotes massive amounts of RAM. Therefore, the maximum frequency of interest was decreased to 500 Hz while maintaining the exact domain dimensions. The tested domain is crucially vast due to it causing tremendous computational effort. Therefore, the simulation reckoning is provided with the Chalmers Vera cluster server.

3.3.1 Input signal

The input signal for the FDTD signal was the same as that used by M. Ge et al. [19], in the CFD simulation, which describes the sound source of a container vessel propeller. The propeller signal corresponds to a full-scale vessel with a draft of 11.3 m, a propeller's diameter of 7.9 m and a rotation speed equal to 28 *rps*. The

sampling frequency of CFD is 57344 Hz. To run the simulation the input signal must be resampled for the FDTD simulation. The FDTD sampling frequency is related to the simulation time speed. The time step is obtained from the maximum frequency of interest, which is 500 Hz and $C_r = 1$. The CDF input signal and resampled FDTD signal in time domain up to 20 ms and frequency spectrum of FDTD input signal are shown in figure 3.13.

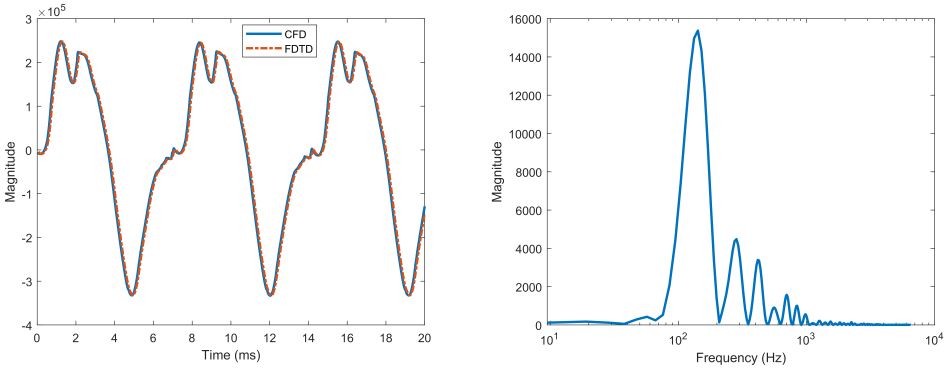

Figure 3.13: CFD and FDTD source signal in time and frequency domain of FDTD input signal.

What stands out in the figure is that the matching of the CFD signal and FDTD input signal are quite consistent in terms of time.
As a result of overlapping the input signal until 190 ms in length, it is ensured that sound propagates continuously throughout the simulation. However, the input CFD signal does not have an ideal fluctuation as this method can produce artefacts or inaccuracies.

3.3.2 Measurements procedures for ocean environment

Pressure change data is collected using hydrophones placed in the far field. The equipment shall sail past the hydrophone. There are different methods of measuring underwater sound emissions from ships. Classification societies such as DNVGL [20] and BV [21] provide sound estimation and measurement standards. In general, hydrophones can be found attached to the sea bed for shallow water environments and buoy hydrophones for deep water environments.
As reported in [21], the hydrophones for shallow water are vertically connected in series. The first hydrophone should be placed at least 15 m from the sea surface. The second probe shall be placed in the range of 15 - 20 m between the first one, and the third one is placed in a range of 15 - 20 m from the second probe but not less than 3 m and not more than 5 m from the sea bottom. Regarding deep water assessment, hydrophones shall be attached to the floating buoy. The first hydrophone should be placed at least 40 m from the sea surface, the second one at a distance greater than 30 m from the first one, and the third one at a distance greater than 30 m from the second one but the distance from the third probe to the seabed should be more than half of the basin depth.

According to [20], for deep water, the minimum water depth shall be 150 m. In shallow water, the testing applies to water depths between 30 and 150 m. The depth below the keel of a vessel shall not be less than the greater of 30 m or three times the draught of the vessel [20], while standard [21] determines assessment minimum depth to be greater than 60 m for shallow water cases.

The measurements shall be carried out within a source to a hydrophone distance range of 100 m to 200 m [20], while [21] suggests the three distances from the vessel to the hydrophones. The distance from the Closest Point of Approach (CPA) to the hydrophone should be at least one ship length of 200 m. For the next sets of measurements the nominal distance to hydrophones $\mathrm{d_{cpa}}$ should be in between $1.5 \cdot \mathrm{d_{cpa}}$ to 400 m and $2 \cdot d_{cpa}$ to 400 m.

3.3.3 Cavitation tunnel

The first tested environment concerns a cavitation tunnel. In [19], the tunnel dimensions imitate the real-scale environment. The purpose of this simulation is to keep the identical real-scale dimensions and BCs behaviour as a cavitation tunnel Accordingly, all dimensions were multiplied by a scaling factor. This led to an actual scale dimension of 260 m in length, 81.48 m in width and 46.56 m in height.

The mesh size was determined by dividing the maximum frequency wavelength by 15. Therefore, the spatial step is 0.2 m and the time step is 0.077 ms while maintaining the Courant factor of 1. The tunnel is programmed as a duct with four fixed total reflective BCs and two thoroughly absorbing PML BC along the x-axis. It has a width of 20 nodes and $\alpha = 5000$. The schematic model is shown in figure 3.14. The simulation length corresponds to the length of the applied signal of 190 ms.

The sound source is intended to reflect the scaled accurate model of a seagoing ship. It is positioned centrally along the x-axis and y-axis while at a depth of 4.8 m from the top surface along the z-axis. The sound source is simulated as a monopole. The hydrophones are placed according to standards [21],[20]. The visualisation of the 3-D cavitation tunnel is shown in figure 3.14. For visualization purposes, the top, side, and front surfaces are transparent.

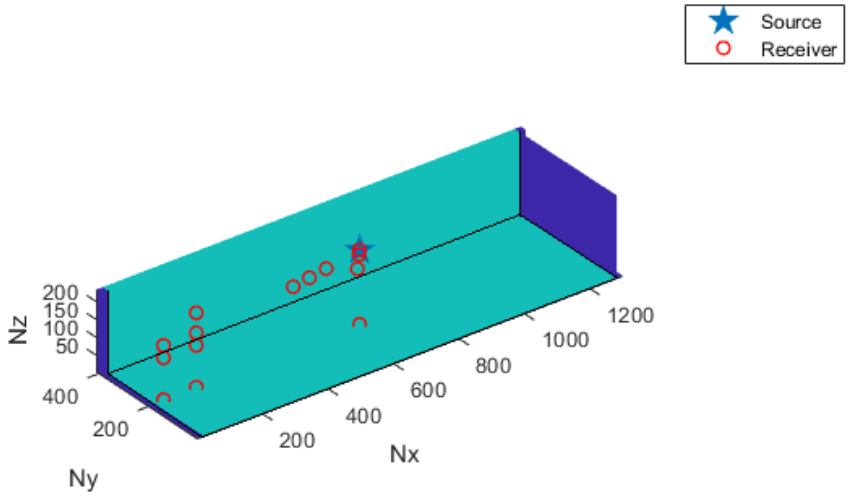

Figure 3.14: Setup of cavitation tunnel behaviour with physical scale dimensions, the blue colour denotes the NPML region, the turquoise color indicates reflective surfaces.

The receivers are situated within a radius of 1 m, 2.4 m, 10 m, 20 m, 30 m and 40 m from the sound source. The receiver placed 1 m from the source intending to normalize other results is the reference point. The reference point is at the top 45 ° from the sound source. This assumed position corresponds to the measuring point, which is located on the ship's hull. Additionally, two buoys are found at a distance of 100 m and 120 m, additional measurement points are placed on the source's axis at a distance of 100 m, and the z-axis is placed under the source. The positions of the hydrophones in all simulations are placed in the same setting for comparison.

3.3.3.1 Scaled Cavitation tunnel

As verification of propagation and to investigate the effect of setting the highest frequency of interest, i.e. 2000 Hz, but with scaled domain dimensions, simulations of the screened cavitation tunnel were applied. In this case, geometrical dimensions, the amplitude of the input signal, the position of the sound source and the receivers' positions were scaled by a factor of 29.1. The domain's dimensions are 18 m long, 2.8 m wide, and 1.6 m high. The tested simulation corresponds to the physical proportions of the cavitation tunnel. However, domain length was increased so that it was possible to implement the PLM absorbing region at the ends of the domain. The speed of sound propagation in water is 1500 m/s. The simulation setup is the same as in the previous cavitation tunnel simulation. It is shown in figure 3.14. For the scaled cavitation tunnel the time step is 0.019 ms and the spatial step is 0.05 m.

3.3.4 Shallow water

The second simulation environment is shallow water. The two conditions are employed to imitate the two different types of seabed. The first stage concerns the fully reflective bedrock under the sediment layer, while the second conditions mimic the infinite wave propagation after the transmission through the sediment layer.

3.3.4.1 Shallow water with bedrock

The domain dimensions are the same as in the cavitation tunnel simulation, except that the z-axis was increased by the thickness of the sediment layer, which results in sizes of 260 m, 81.48 m, and 56.56 m. The sound water speed propagation is c = 1500 m/s. The upper boundary between water and air has been simulated as a perfect reflecting surface because the reflection coefficient between seawater and the air is approximately 1. During this time, a sediment layer of c_s = 1600m/s and ρ_s = 1200kg/m^3 with a thickness of 10 m was placed on the bottom. Under the sediment layer, there is bedrock with full sound reflection properties. The outer surfaces along the x-axis and y-axis have been simulated as fully open by the PML region. The sound water speed propagation is c = 1500 m/s and the maximum limit frequency is 500 Hz. The mesh size was determined by dividing the maximum frequency wavelength by 15. This resulted in a spatial step of 0.2 m, and a time step of 0.0693 s while maintaining the Courant factor of C_r = 0.9. The hydrophones' location is the same as in the example of the cavitation tunnel. Graphical representation of tested domain shows figure 3.15.

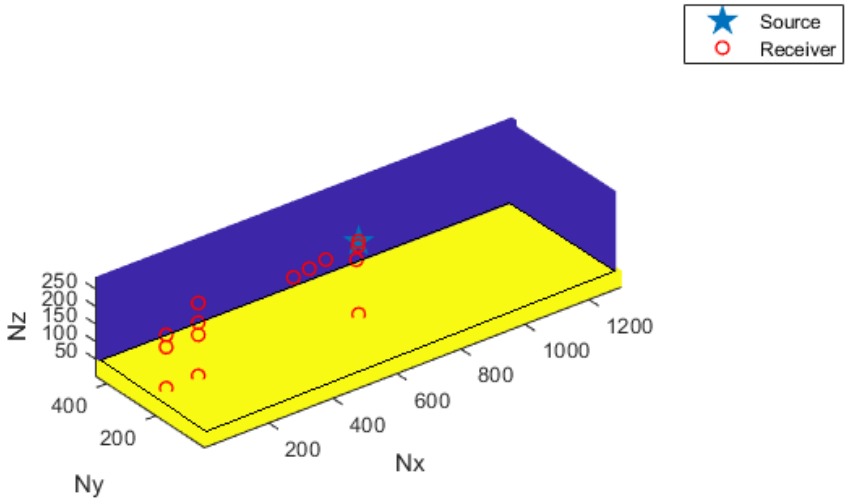

Figure 3.15: Setup of shallow water domain with reflective bottom under the sediment layer, the blue colour denotes the NPML region, the yellow area denotes the sediment region.

3.3.4.2 Shallow water with infinite propagation

The second shallow water simulation is a simplified model of the infinite propagation through the sea bed. It corresponds to the high absorption or infinite sediment layer. The sediment layer of $c_s = 1600$ m/s and $\rho_s = 1200$ kg/m^3 with a thickness of 10 m was used, under the sediment layer the PML region with a thickness of 20 nodes was applied with $\alpha = 5000$. The same properties are applied to the PLM region along the x-axis. To keep the same size of the water propagation basin, the z-axis of the simulation domain was increased by 4 m to cover the thickness of the PML absorption area. The schematic 3-d domain placement shows figure 3.16. For 3-d visualization purposes, the top, side, and front surfaces are transparent.

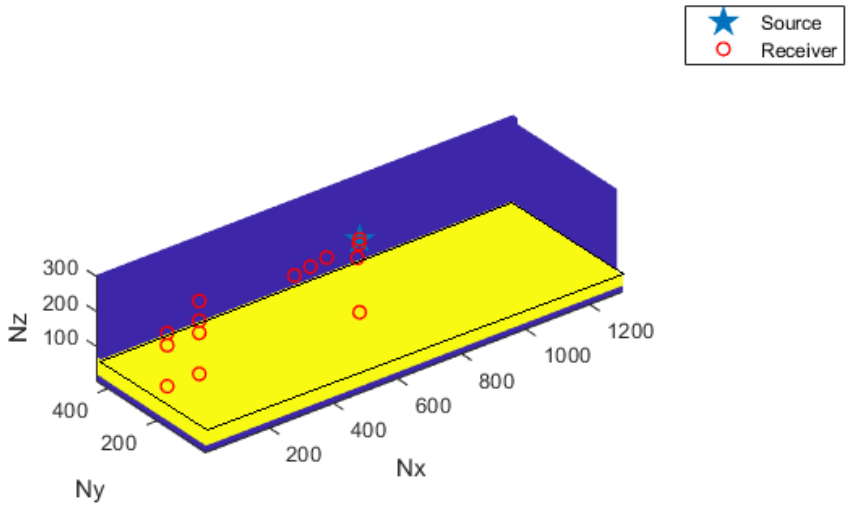

Figure 3.16: Setup of shallow water domain with absorption bottom under the sediment layer, the blue colour denotes the NPML region, the yellow area denotes the sediment region.

3.3.5 Deep water

As part of the further simulation, deep water represents the condition of the open sea. The upper boundary between water and air was simulated as an ideal reflecting surface as in the simulations before. For the other boundary edges, the PML ABC with a width of 20 nodes and α =5000 was applied. Due to the PML region increasing domain dimensions along the y-direction and the z-bottom. Therefore, the domain sizes are 260 m, 89.48 m and 50.56 m. The maximum limit frequency is 500 Hz. Sound water propagation is $c = 1500$ m/s. The same propagation domains can be analyzed more easily when the boundary conditions are different. The mesh is determined as before by dividing the maximum frequency wavelength by 15. This results in a spatial step of 0.2 m and a time step of 0.077 s while maintaining the

Courant factor of 1. In [21], it is suggested that the probes' position should be considered for open sea conditions. However, it is impossible to apply hydrophones at such depths since the open sea condition is achieved by employing the PML regions. Therefore, the same hydrophone locations as in the shallow water model were used in this simulation.
The schematic 3-d domain placement shows figure 3.17. For visualization purposes, the top, side, and front surfaces are transparent.

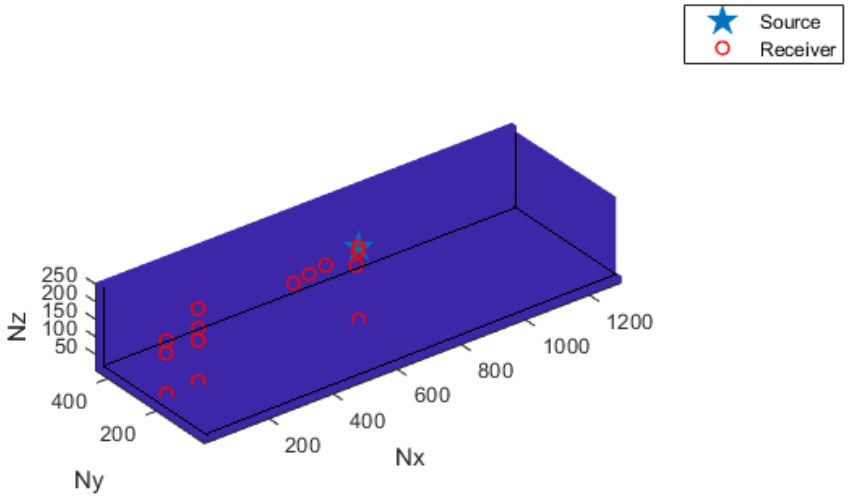

Figure 3.17: Setup of open sea condition, the blue colour denotes the NPML region.

3.3.6 Canal

The subsequent simulation concerns the waterways canal environment. Two various conditions are applied. The first is with fully reflective side retaining walls, and the second is with a sand layer on the canal's sides.

3.3.6.1 Canal with fully reflective retaining walls

Canal BC's are similar to the cavitation tunnel simulation, except the bottom surface where 10 m of sediment layer is applied with $c_s = 1600$ m/s and $\rho_s = 1200$ kg/m^3, under the sediment is placed fully reflective bedrock. The upper domain edge represents the fully reflective boundary between water and air. The boundary along the x-axis belongs to the PML region with a thickness of 20 nodes and $\alpha = 5000$. Sound propagation in water is $c = 1500$ m/s. The domain size is 260 m, 82.48 m, and 56.56 m. The domain peripheries and the y-axis act as fully reflective materials, which could represent concrete walls or steel retaining walls, which are common in canal construction. The maximum limit frequency is 500 Hz. The

mesh size was determined by dividing the maximum frequency wavelength by 15. This resulted in a spatial step of 0.2 m, and a time step of 0.0693 s while maintaining the Courant factor of C_r= 0.9. For experimental and analyzing purposes the hydrophones' location is the same as in the example of a cavitation tunnel.

The schematic of 3-D domain placement shows figure 3.18. For 3-D visualization purposes, the top, side, and front surfaces are transparent.

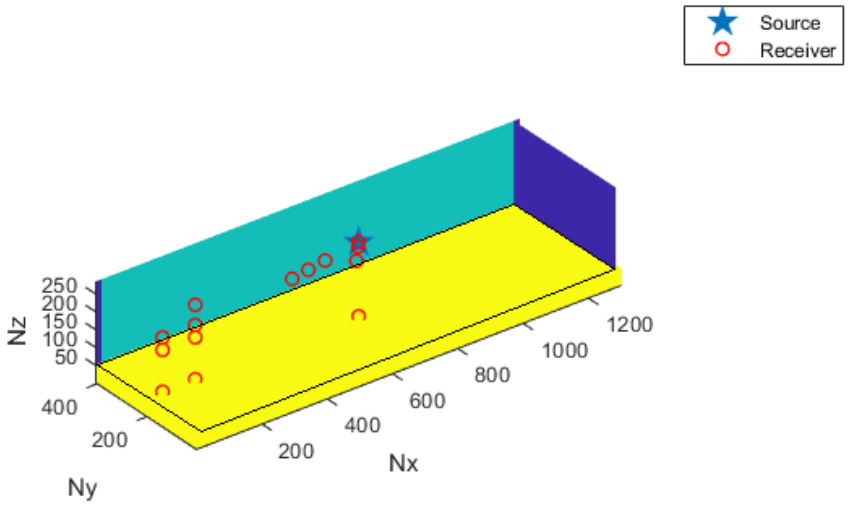

Figure 3.18: Arrangement of water canal simulation, the blue part denotes the NPML region, the yellow area corresponds to the sediment, and the turquoise colour represents the reflective walls.

3.3.6.2 Canal with sediment walls

The second condition for the canal simulation covers the canal with absorption walls. The sound water speed propagation is $c = 1500$ m/s. The upper boundary between water and air has been simulated as a perfect reflecting surface because the reflection coefficient between water and air is approximately 1. A sediment layer of $c_s = 1600$ m/s and $\rho_s = 1200$ kg/m^3 with a thickness of 10 m was placed on the bottom. Under the sediment layer, there is bedrock with full sound reflection properties. In the side walls according to [23], sediment layer of sand-silt-clay with properties $c_w = 1582$ m/s and $\rho_s = 1575$ kg/m^3 with a thickness of 10 m is used . The domain size is 260 m, 102.48 m, and 56.56 m. This arrangement can represent the natural waterways and canals/rivers without reinforcement sides.

The schematic 3-d domain placement shows figure 3.19. For 3-d visualization purposes, the top, side, and front surfaces are transparent.

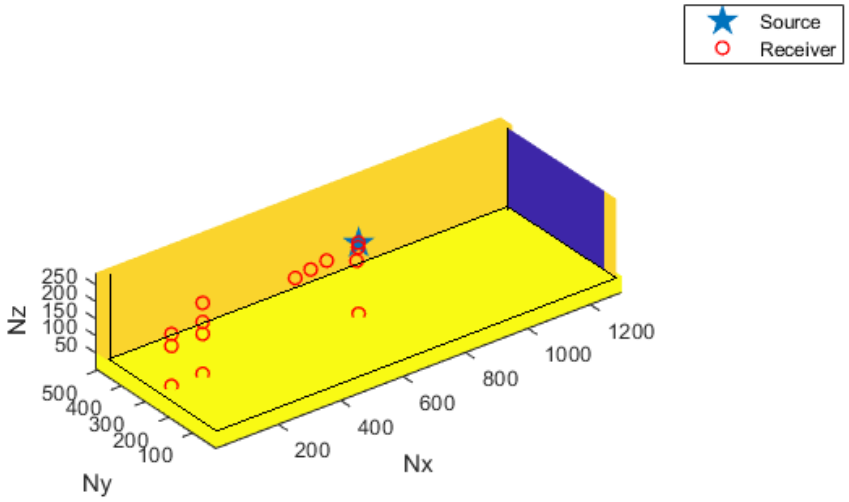

Figure 3.19: Setup of water canal with sediment walls.The blue part denotes the NPML region the yellow shaded area corresponds to the sediments materials

3.3.6.3 Canal with water profile

A simplified model of the canal environment was used to investigate the influence of various water properties. This time the sound water speed propagation is depth-dependent and varies from 1515 m/s in the top area to 1480 m/s in the bottom layers, while the water density changes from 1022.5 kg/m^3 to 1024.5 kg/m^3 [25]. The sound speed and density profiles show in figure 3.20.

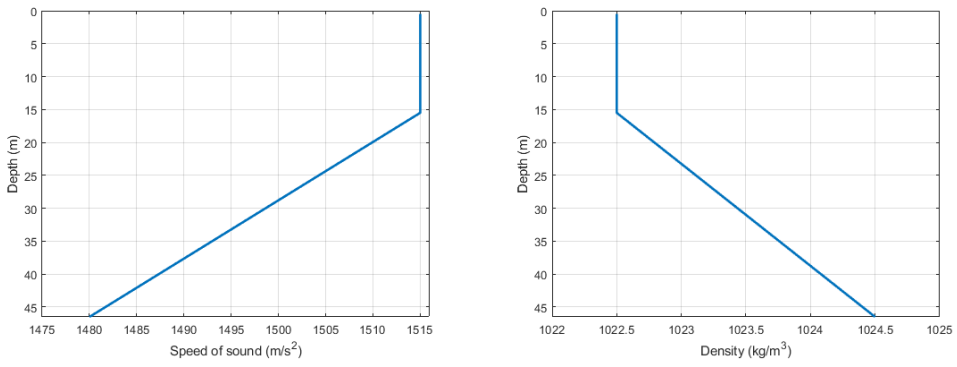

Figure 3.20: Sound velocity and water density water canal profiles gradients.

The water profile conditions correspond to the water temperature from 18 ° C close to the top boundary and 12 ° C at the seabed. That velocity temperature density relationship matches the salinity in the range of 31.2 practical salinity units (PSU) to 32 PSU. The simplified profile of velocity and density is present in the figure. That

simplified model can represent the waterways between two mixing water mediums, e.g. reservoirs with two different PSU properties.
The upper boundary between water and air is simulated as in Canal with sediment walls example. Therefore, a sediment layer of $c_s = 1600$ m/s and $\rho_s = 1200\ kg/m^3$ with a thickness of 10 m was placed on the bottom. Under the sediment layer, there is bedrock with full sound reflection properties. In the side walls according to [23], sediment layer of sand-silt-clay with properties $c_w = 1582\ m/s$ and $\rho_s = 1575$ kg/m^3 with a thickness of 10 m is used . The PML regions along the x-axis have a thickness of 20 nodes with $\alpha = 5000$. The domain size is 260 m, 102.48 m, and 56.56 m. This arrangement can represent the natural waterways and canals/rivers without reinforcement sides.

4

Results

The following section presents the FDTD simulation results from the code validation process and the environment simulations.

4.1 Validation

In this subsection, the validation procedure steps of the FDTD Matlab code and accuracy evidence conditions are presented. Furthermore, the following chapter covers the authentication of different boundary conditions with frequency spectrum plots and snapshot wave propagation visualisations.

4.1.1 Free Field

The first set of validations aimed to check the sound speed accuracy of various mesh sizes by dividing the wavelength into nodes. The simulation sound propagation speed was acquired by comparing the recorded time of the peak amplitude between the reference point and the receivers' positions. Table 4.1 shows the result of sound propagation between the reference point and the three receivers' positions.

Table 4.1: Speed propagation at the receiver's position for various mesh sizes.

	$\lambda/4$	$\lambda/5$	$\lambda/10$	$\lambda/15$	$\lambda/20$	$\lambda/25$
Receiver 1 (m/s)	2250	1500	1500	1500	1500	1500
Receiver 2 (m/s)	1800	1500	1500	1500	1500	1500
Receiver 3 (m/s)	1800	1500	1500	1500	1500	1500

What stands out in the table 4.1 is that the sound propagation speed in water does not converge for $\lambda/4$, while the results for the rest of the tested simulations got valid results. From this data, it can be noticed that the $\lambda/4$ does not deliver a good simulation performance. The next step consisted of a time contrast between the probes' recorded signals at the receiver positions for different accuracies. Figure 4.1 shows the recorded signal in the time domain for source and receiver positions.

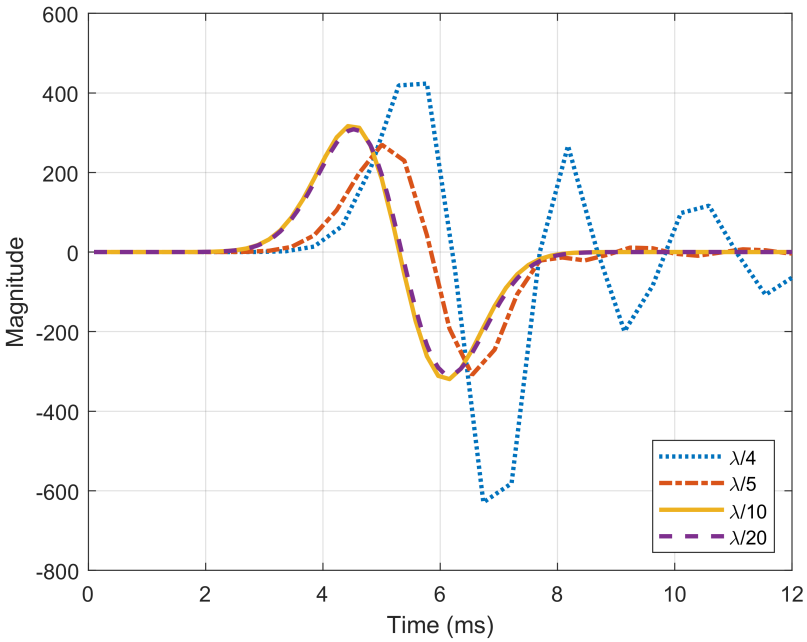

Figure 4.1: Signals at the receivers positions in time domain.

Further analysis showed that the results for $\lambda/10$ and $\lambda/20$ overlap and derived accurate outcomes. As expected, the $\lambda/4$ differs significantly from the rest of the results. Interestingly, the $\lambda/5$ was observed to slightly deviates from the correctness, which was not provided by comparison only the propagation velocity. Additionally, the analysis of the frequency spectrum of the signals was performed, and the results are shown in figure 4.2.

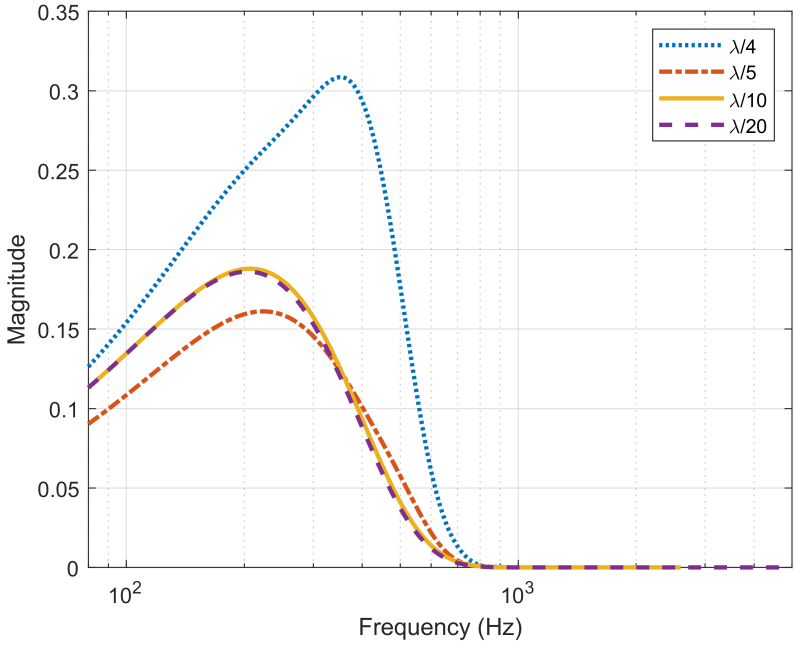

Figure 4.2: Receiver frequency spectrum.

As expected, the curve for the two coarse mesh sizes differs from the rest. The time domain analysis with the frequency analysis showed the same results and confirmed that conditions of $\lambda/4$ and $\lambda/5$ are imprecise.

4.1.2 Reflection rigid boundary

The second set of analyses examined the impact of rigid boundary conditions. For that purpose, an analytical approach is used to justify the numerical results. For the analytical solution, the conditions of the numerical simulation were recreated, i.e. the indent value of the sound speed in water c = 1500 m/s. The receiver was positioned at a distance of 10 m from the sound source. The Green's function for the 10 m and 30 m radius was used to estimate the pressure of the incident wave and the reflected wave. For a better comparison, the same procedure was performed also for the $\lambda/10$ and $\lambda/15$ simulations. Figure 4.3 shows the recorded signal in the time domain for receiver positions.

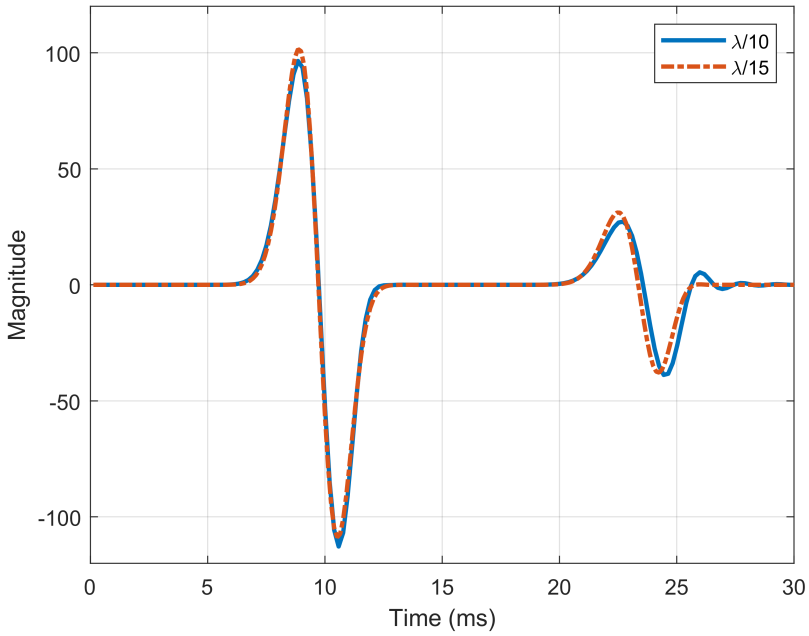

Figure 4.3: Signal at receivers position in time.

From the data in figure 4.3, it is seen that the incoming wave reaches the receiver position at approximately 8 ms and the signal is consistent for both $\lambda/10$ and $\lambda/15$. The reflected signal arrives at the receiver position at 23 ms. What is interesting about the data in this figure is that the simulation reflected signal for $\lambda/10$ has some additional harmonics.

In order to check if the rigid wall introduces any inconsistencies in the signal, the frequency spectrum of the incoming wave and the reflected one from the receiver were compared. The results are shown in figure 4.4.

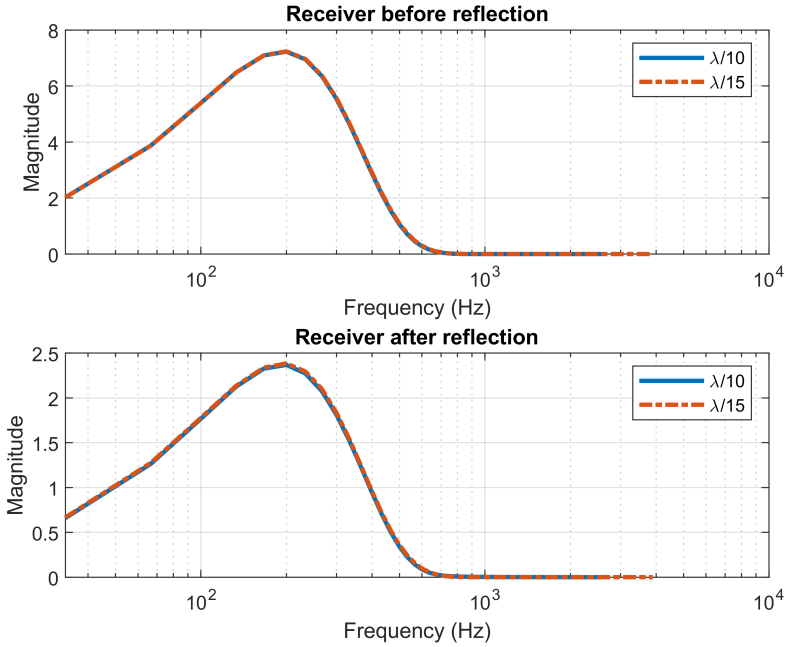

Figure 4.4: Frequency spectra of incoming wave reflected signal at receiver position.

As shown in the figure 4.4, it is notable that the energy spectrum has the same distribution over the frequency of incoming and reflective signals. By comparing the two signals, all frequencies included in the incoming signal are the same as the reflected signal frequencies.

Afterwards, the ratio of decay ΔL_p was calculated for both numerical and analytical approaches. Figure 4.5 presents the findings.

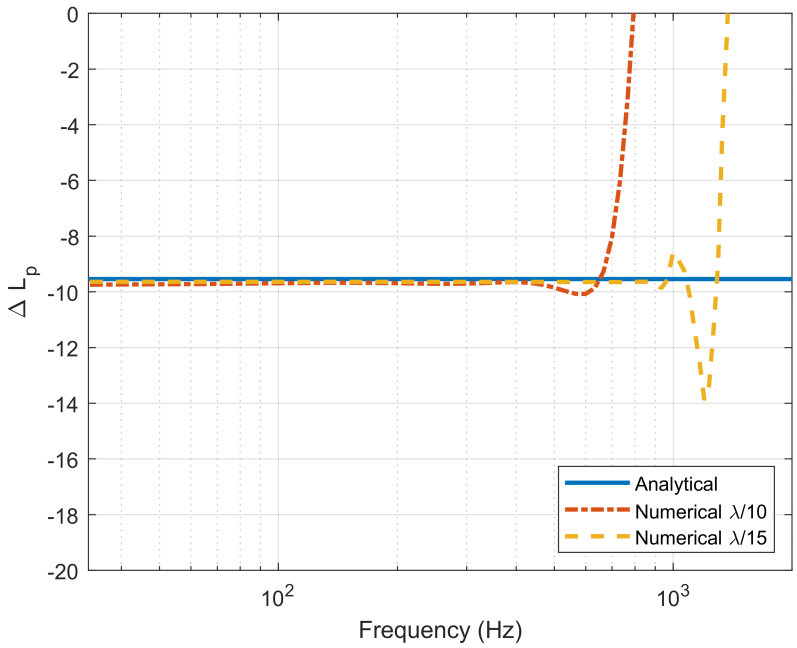

Figure 4.5: Comparison between analytical and numerical solutions

The results, as shown in the figure 4.5, indicate that the analytical and numerical results match quite well. However, the $\lambda/15$ is characterised by better fitting to the analytical approach than $\lambda/10$. The accurate results limit for $\lambda/10$ is up t 400 Hz, while the $\lambda/15$ curve fits well up to 800 Hz.

4.1.3 Ground/Sediment boundary condition

The next set of analyses examined the impact of semi-reflective boundary conditions. For that purpose, an analytical approach is used to justify the numerical results. For the analytical solution, the conditions of the numerical simulation were recreated. The receiver was positioned at a distance of 10 m from the sound source. The Green's function for the 10 m and 30 m radius was used to estimate the pressure of the incident wave and the reflected wave. For a better comparison, the same procedure was performed also for the $\lambda/10$ and $\lambda/15$ simulations. Figure 4.6 shows the recorded signal in the time domain for receiver positions.

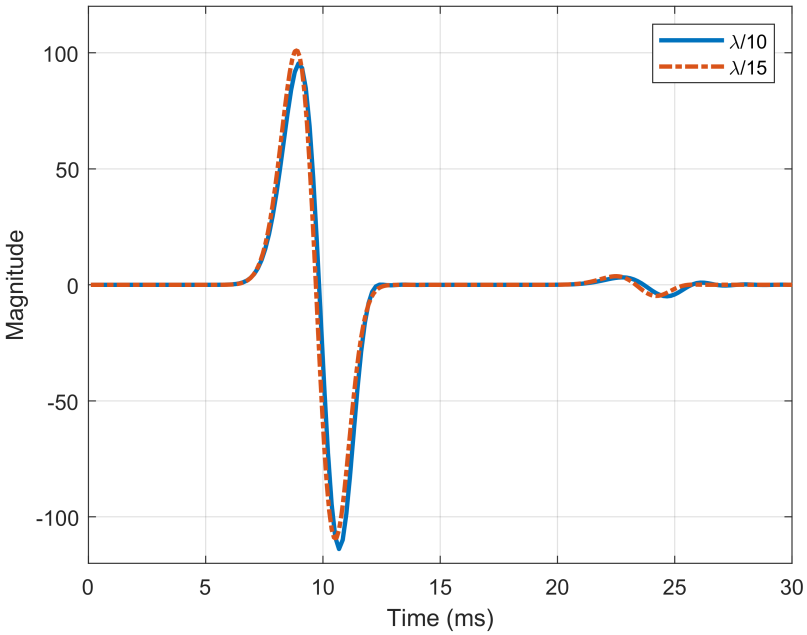

Figure 4.6: Source and receiver signals in the frequency domain; sediment simulation.

From the data in figure 4.6, it is apparent that the signal reaches the receiver at 10 ms of amplitude around 100, the deviation from 0 appears around 24 ms represents the reflected energy from the sediment layer, the reflected signal has significantly lower amplitude in comparison to perfectly the reflective case, presented in figure 4.3.

The next section of the test was concerned with the frequency spectrum. The energy distribution for the incoming and reflected signals over the frequency is plotted in figure 4.7 to establish whether the sediment layer initiates any inconsistencies in the frequency spectrum.

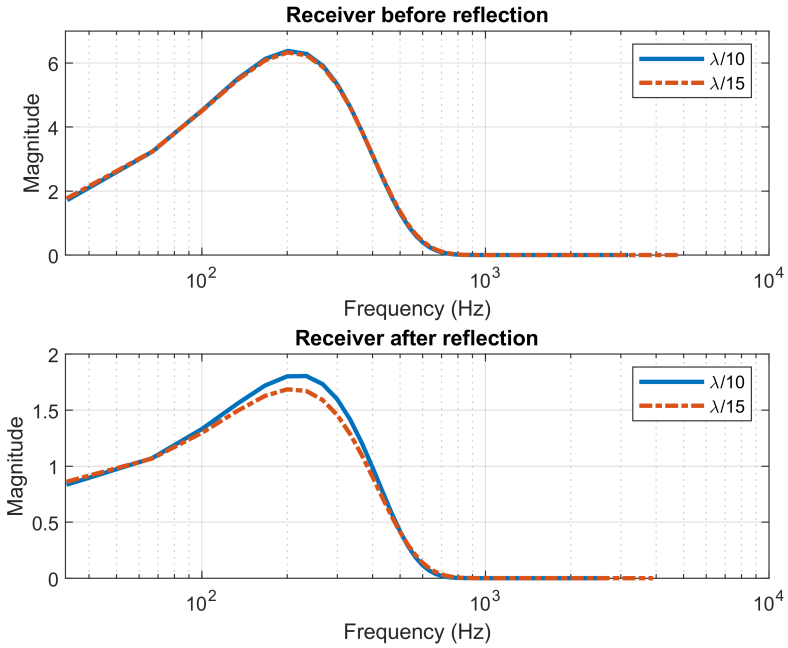

Figure 4.7: Source and receiver signals in the frequency domain; sediment simulation.

Both signals, incoming and reflected, have the same frequency curve distribution. The reflected signal has a lower magnitude. Overall, two mesh sizes $\lambda/10$ and $\lambda/15$ derived the same frequency results.

Afterwards, the ratio of decay was calculated ΔL_p for both numerical and analytical approaches. Figure 4.8 presents the results.

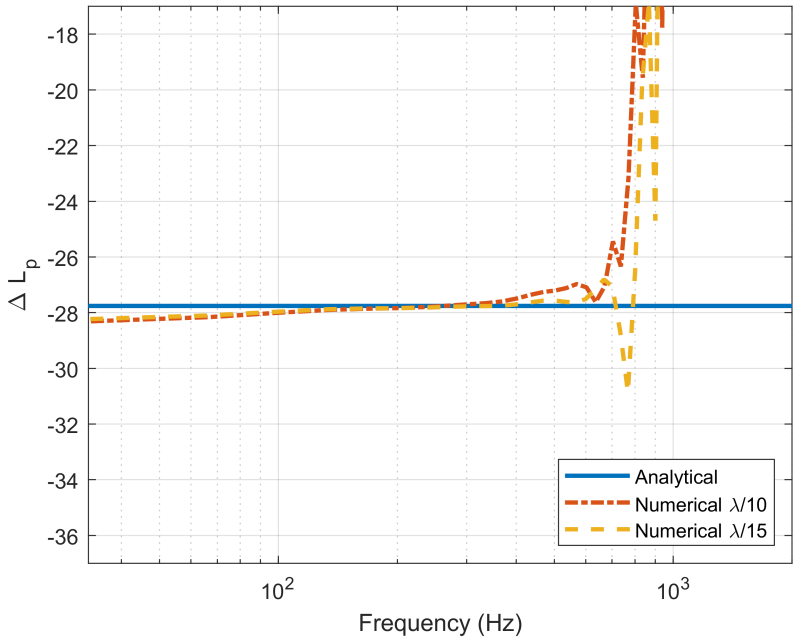

Figure 4.8: Comparison between analytical and numerical solutions.

Both spatial mesh sizes deliver consistent results in scope up to about 400 Hz with a maximum wavelength of 300 Hz. Above that range, the results for $\lambda/10$ become incoherent, while $\lambda/15$ is reasonable up to 600 Hz.

4.1.4 Perfectly Matched Layers

The last investigation covers the demonstration of PML with Absorbing Boundary Conditions. The aim of the PML simulation analysis was used to check the reflection intensification from the PML region. In figure 4.9 the signal at the receiver position and zoomed reflection from the PML in the time interval is presented for six different designs of PML regions.

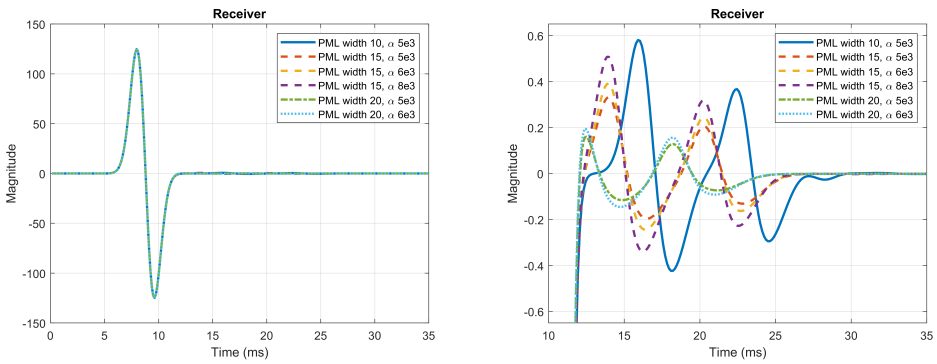

Figure 4.9: The amplitude at the receiver position for different PML properties.

The reflection amplitude from PML classifies in the range of 0.4 - 0.6. and it is noticeable at 12 - 30 ms.

What is interesting about the data in the figure 4.9 is that the highest attenuation coefficient $\alpha = 6000$ does not perform the greatest reduction. However, the increased PML width of up to 20 nodes delivers the best results in comparison to the shorter PML thicknesses.

Figure 4.10 shows the Sound pressure levels distribution of pressure in the time domain for the receiver position.

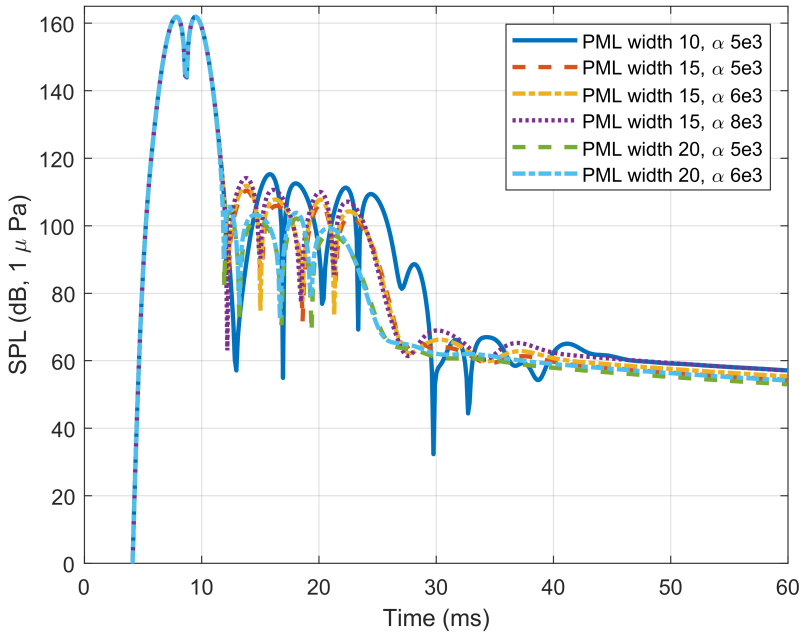

Figure 4.10: Sound pressure levels of various PMLs parameters.

As can be seen from the figure 4.10, the SPL decays after approximately 28 ms. The best reduction has the NPML with a width of 20 nodes, and the attenuation coefficient equals $\alpha = 5000$.

For further authentication, the NPML and fully reflective cases were compared of domains with dimensions of 40 m length, 40 m width and 40 m height with the source placed in the centre and the receiver placed at a 10 m distance from the sound source for both cases. The simulation accuracy for both cases is λ / 15. The NPML region was set PML with a width of 20 nodes, and the attenuation coefficient equals $\alpha = 5e3$. The frequency spectrum differences are presented in figure 4.11.

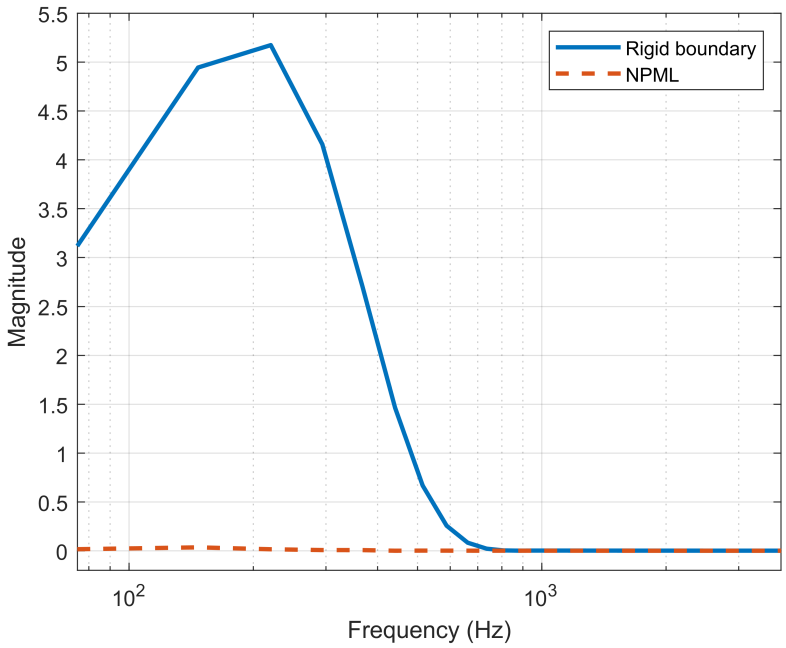

Figure 4.11: The frequency distribution of receivers for the rigid boundary and NPML.

By looking at the figure above, it shows that the energy over the frequency bands is significantly reduced while applying the NPML. Although there are some deviations within the limits of the numerical error, as seen in the figure, the NPML example curve is not perfectly straight over the low frequencies.

4.2 Simulation

The following section describes the results of the various FDTD simulation environments. Results from two floating buoys for three hydrophones assigned to each buoy are shown. The results of the subsequent simulations are presented in the temporal domain, Spectral density, normalized Sound Pressure Levels and pressure contour in cross-sections.

4.2.1 Cavitation tunnel

The first set of questions was to determine if FDTD could be representative of a simulation of CFD measurements for cavitation tunnel and the performance of the individual pressure distribution. To answer that, further considerations present the results and analysis of the cavitation tunnel simulation. Figure 4.12 shows recorded amplitude pressure from floating buoys placed 100 m and 120 m from the source.

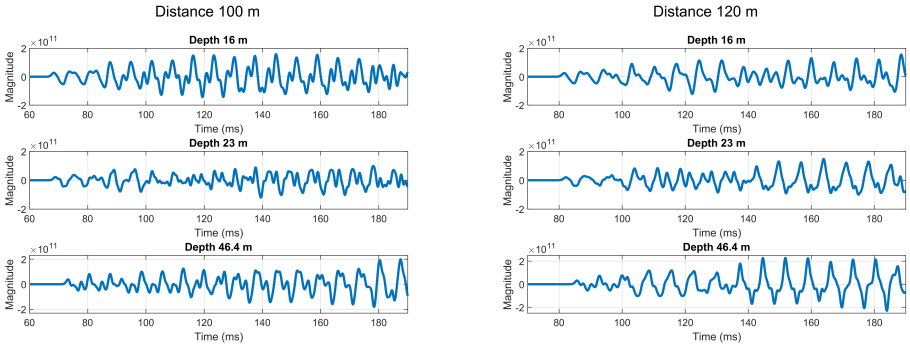

Figure 4.12: The amplitude at receiver positions at 100 m and 120 m in the simulation of a cavitation tunnel.

Figure 4.12 shows that the first wave front reaches the receiver at around 65 ms and around 80 ms for a 120 m distance. The hydrophones, which are closer to the upper and lower surfaces, have a higher amplitude than those in the middle. This behaviour may be associated with fully reflective BCs of a cavitation tunnel. Interestingly, the depth of 46.4 m for a 120 m distance was observed to be associated with a high amplitude. The reason may be wave interference and resonance at this receiver position.

By continuing the investigation, hydrophone frequency spectra were taken. The time signals were truncated to reduce the undesired signal output, then a Hanning window was used and the signals were zero-padded before applying FFT. The hydrophone frequency spectra are shown in 4.13.

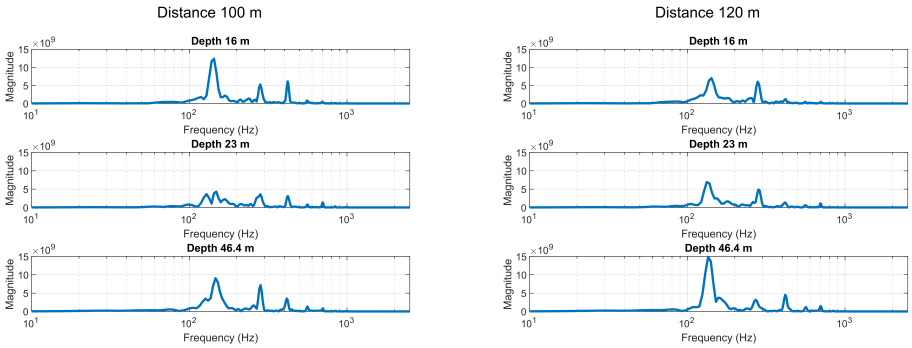

Figure 4.13: The cavitation tunnel frequency spectra at 100 m and 120 m.

In the frequency spectrum, there are prominent harmonic frequencies around 135 Hz, 270 Hz, 420 Hz, 560 Hz, and 700 Hz. This is shown in the figure 4.13.
By comparison of the input frequency spectrum from the figure 3.13 and figure 4.13 it can be concluded that the harmonic frequencies from the input signal are present at hydrophone positions. As in the time spectrum, the most energy is found in the top and bottom hydrophones, while the hydrophones in the middle have less energy. Multiple signal reflections and wave interferences result in some losses, for instance, in the range of 142 Hz to 284 Hz for the middle hydrophones. Surprisingly, the hydrophone placed close to the bottom at 120 m has a higher magnitude for harmonic frequencies than the probe placed at 100 m, which, as mentioned before, can be introduced by multiple wave reflections from the cavitation tunnel walls.

According to [21] the measurements results shall be presented as Sound Pressure Level with reference value $1\mu Pa$ normalized to 1 m measurement from the sources, such results for narrow bands (solid line) and 1/3 octave bands (dash-dotted line) are presented in figure 4.14 for 100 m.

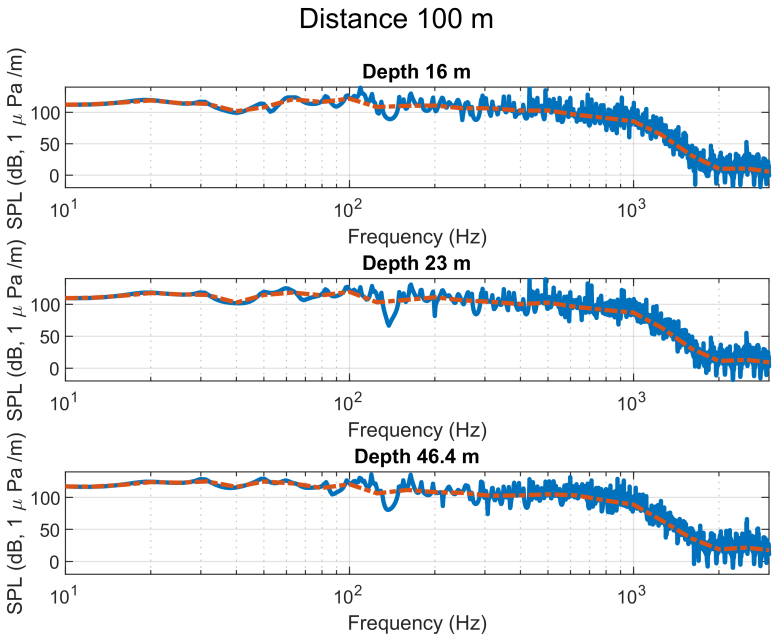

Figure 4.14: The cavitation tunnel normalized Sound pressure level for buoy located 100 m from the sound source in narrow and 1/3 octave bands.

In the same order the process was applied for the other hydrophones measurements, figure 4.15 shows the normalized sound pressure in 1/3 level for 100 m distance.

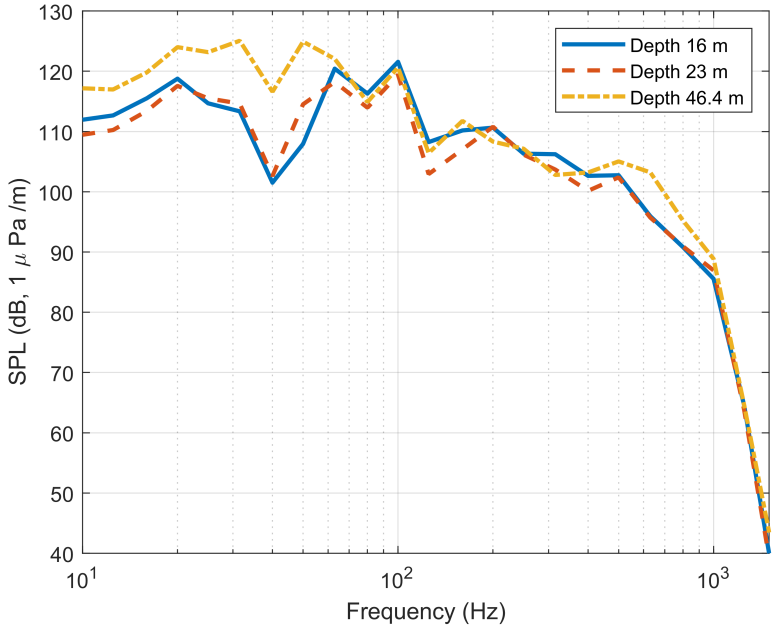

Figure 4.15: The cavitation tunnel simulation normalized sound pressure level in 1/3 octave bands for cavitation tunnel at 100 m

The normalized sound pressure level in 1/3 octave bands for probes at 120 m distance shows figure 4.16.

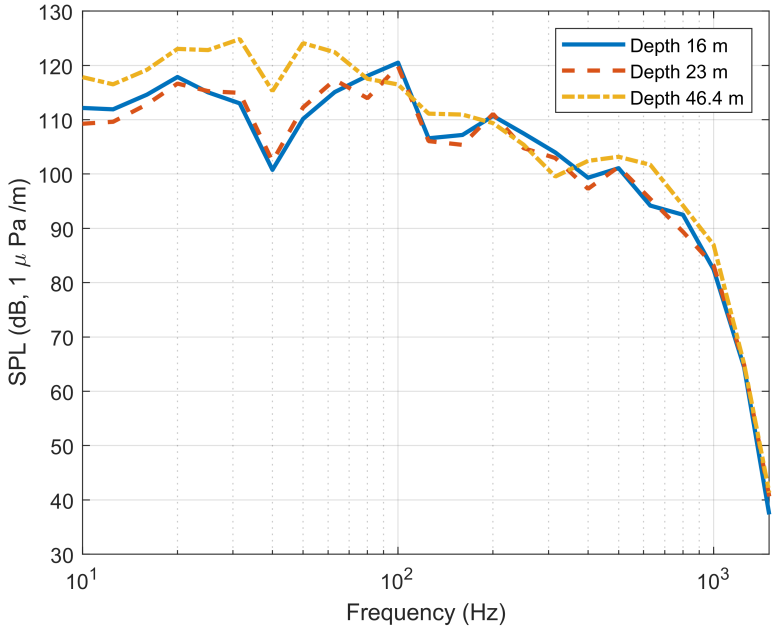

Figure 4.16: The cavitation tunnel simulation; normalized sound pressure level in 1/3 octave bands for cavitation tunnel at 120 m.

What can be seen in figure 4.15 and figure 4.16 is that the probes closer to the bottom boundary have the highest SPL in the range of 10 Hz to 70 Hz. In all curves,the SPL distribution appears deepest at 40 Hz. At both distances for the middle and upper hydrophones, the curve spreads are the most consistent.

The SPL RMS calculations were performed over the simulation time with normalizing to 1 m and the reference pressure. This was done for two cross-sections, longitudinal and transverse, to obtain an overview of the acoustic pressure distribution in the spatial domains. The results are presented as a contour projection with isobars in figure 4.17 for the x-z view and figure 4.18 for the y-z view.

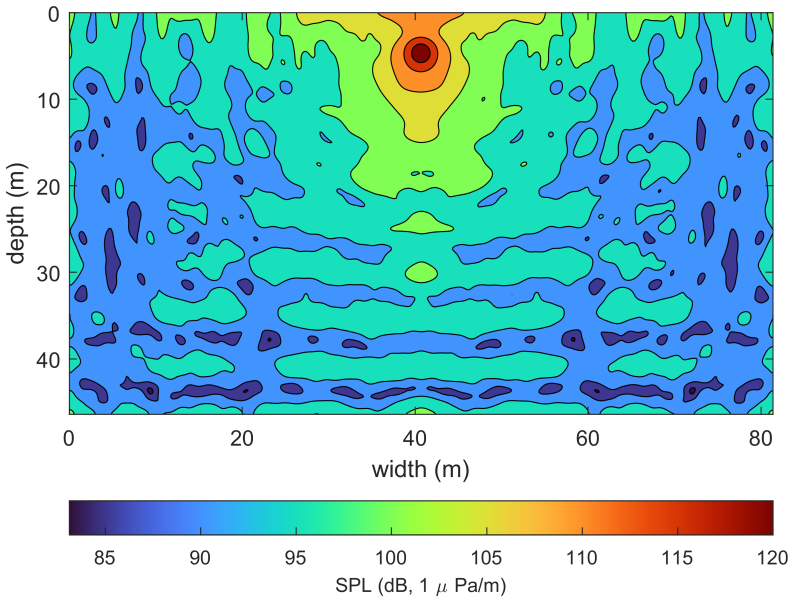

Figure 4.17: The cavitation tunnel simulation; RMS SPL contour with distance normalization for the y-z plane.

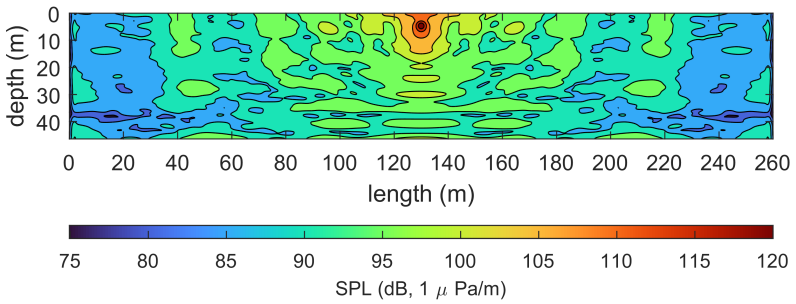

Figure 4.18: The cavitation tunnel simulation; RMS SPL contour with distance normalization for the x-z plane.

By investigating figures 4.17 and 4.18, it is seen unique pressure pattern for cavitation tunnel simulation. The pressure zones in the middle of the domain have a visible dome- shape, while with the increase in distance, the pressure is distributed parallel to the domain boundaries, which is observed in the y-z cross-section. There is also an interweaving of different pressure sectors with distorted isobars. Moreover, the pressure distribution is inconsistent.
The cavitation tunnel simulation outcome in normalized pressure levels for the rest of the measurement points i.e. points at 10 m, 20 m, 30 m, and 40 m, located at an angle of 45 ° from the plane of the source; the point lying on the axis of the sound source at a distance of 100 m; the receiver located centrally below the propeller at a depth of 46.4 m; the point located at the propeller's tip at the distance of 2.4 from the sound source; and a four-time simulations amplitude distribution snapshot for the two cross sections can be found in the Appendix A.1.

4.2.1.1 Near-field and Far-field propagation

An additional test for cavitation tunnel simulation was conducted to check sound propagation behaviour at a distance of 1 m and 30 m from the sound source. This was done in different directions in the cavitation tunnel environment.
For near-field purposes, four measuring points have been set. Point 1 at a distance of 1 m at an angle of 45 ° under the sound source. Point 3 is positioned perpendicular to point 1 in the x-y plane. Point 2 is symmetrical to Point 2 in the x-z plane. Point 4, at 1 m at an angle of 45 degrees in the upper part of the sound source over Point 2.
The results for these individual points in the time domain and SPL are shown in

figure 4.19.

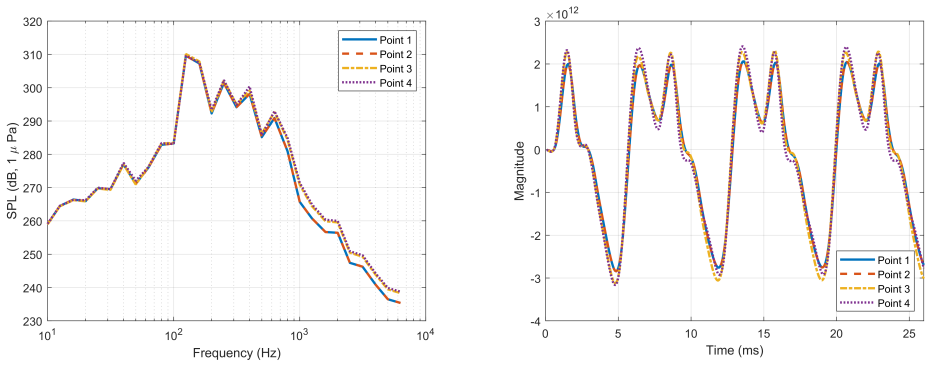

Figure 4.19: Measurement points 1 m away from the sound source in the time domain and their SLP records.

The results, as shown in figure 4.19 indicate that only points 1 and 2 are consistent. Point 3 and Point 4 delivered moderately deviation. Points 3 and 4 are similar layouts but not identical.
The far-field test concerns three points placed 30 m from the sound source. The measured data are at an angle of 45 degrees from the noise source. The measured points 1 and 2 are positioned symmetrically to each other relative to the z-x plane placed in the middle of the y-axis, while point 3 is symmetrical to point 2 on the y-z plane passing through the sound source. The results for these points in the time domain and SPL are shown in 4.20.

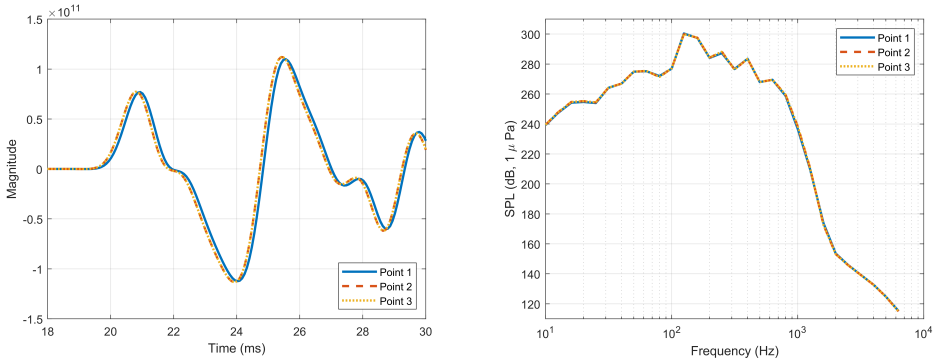

Figure 4.20: Measurement points 30 m away from the sound source in the time domain and their SLP records.

A closer inspection of the signals in the time domain shows that the signals' amplitudes are not coherent. Data integrity is observed at Points 1 and 2, while Point 3 differs slightly from what is observed at the other points. However, the SPL distribution for the examined samples does not show large deviations.

4.2.2 Scaled Cavitation tunnel

The additional scaled simulation focused on the behaviour of the sound waves within the spatial domain. The RMS average pressure over the whole simulation time with reference pressure value 1 μPa, normalized by the scaled distance of 1 m is shown for the y-z plane cross section in figure 4.21 and for the z-x plane in figure 4.22. The magenta dashed line represents the boundary between the non-PML and PML regions.

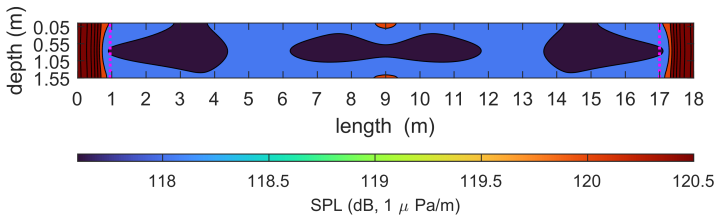

Figure 4.21: Scaled cavitation tunnel RMS SPL contour with distance normalization for the x-z plane.

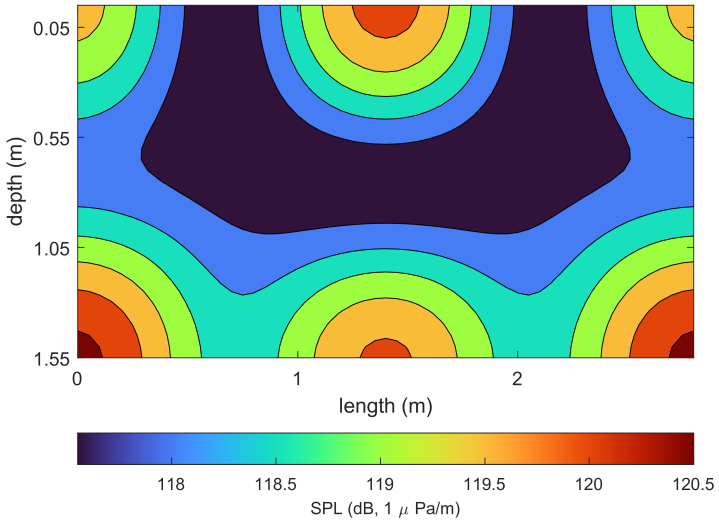

Figure 4.22: Scaled cavitation tunnel RMS SPL contour with distance normalization for the y-z plane.

The corresponding higher-pressure regions are in the y-z plane domain corners. The source zone and the domain bottom edge in the centre of the source have high-pressure characteristics. The relatively low-pressure region surrounds the sphere-shaped sound source, which appears in the middle of the domain. Moreover, two symmetric low-pressure patterns along the z-y plane are present close to the PML regions. The scaled cavitation tunnel results showed the simplified sound propagation model and showed an overall propagation pattern. It can help us to understand the sound propagation behaviour at higher frequencies of interest.

4.2.3 Shallow water

A set of two simulations was provided to compare the difference between the cavitation tunnel and the shallow water environment. The main question concerns the influence of boundaries under the layer of sediment.

4.2.3.1 Shallow water with bedrock

The first shallow water simulation treats the reflective surface under the layer of sediment. The measurement data were processed according to the same steps as described previously for the cavitation tunnel simulations for three different depths at two distances according to the standard measurements [21].
The sound pressure level with the 1 m normalisation in 1/3 octave bands for probes at 120 m distance is shown in figure 4.23,

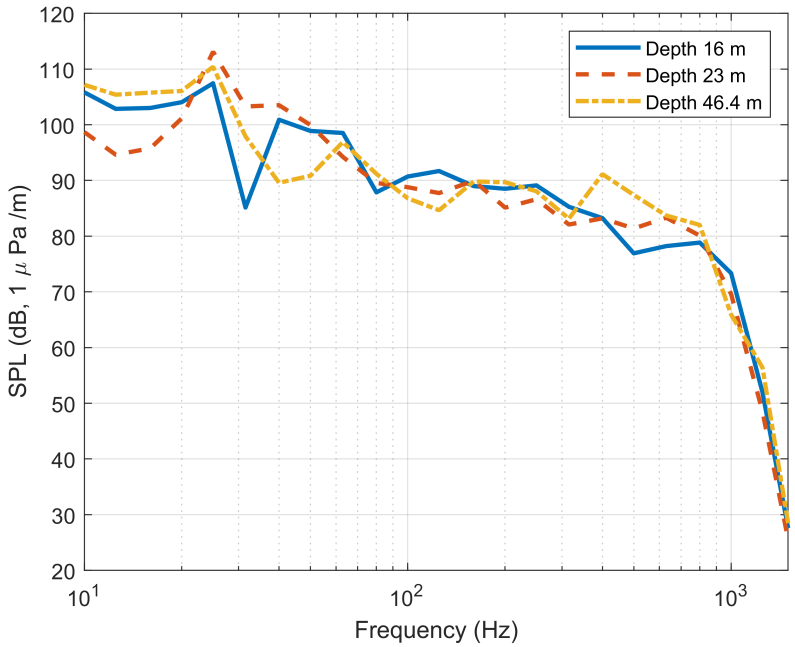

Figure 4.23: Normalized sound pressure of the shallow water simulation level in 1/3 octave bands at 100 m.

and for the 120 m distance shown in figure 4.24.

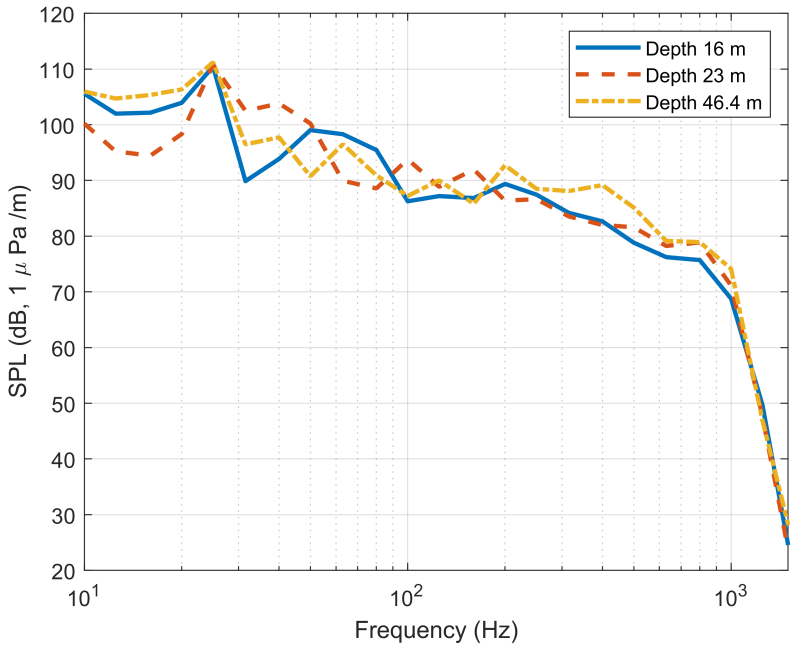

Figure 4.24: Normalized sound pressure of the shallow water simulation level in 1/3 octave bands at 120 m.

What can be concluded from the figures presenting the normalized SPL is that both plots have a similar distribution around 120 Hz. What is interesting is that the normalized SPL pressure at 120 m has approximately the same level around 25 Hz. However, at the depth of 100 m, the energy varies at a particular depth.

A closer inspection of the figures above shows that all measured depths peak at around 24 Hz. What stands out from the data is the sudden decrease in SPL appearing at 32 Hz for depths of 16 m for two measured distances. Generally, the results overview shows that the SPL is lower at all depths at 120 m than at 100 m.

.

The following step of investigation concerns the SPL spatial distribution. Figure 4.33 shows the acoustic pressure distribution with 1 m distance normalization over the y-z plane, while figure 4.34 illustrates the normalized pressure contour over the x-z plane. The magenta dotted line stands for the Boundary of the PML region, whereas the dashed black line represents the sediment boundary.

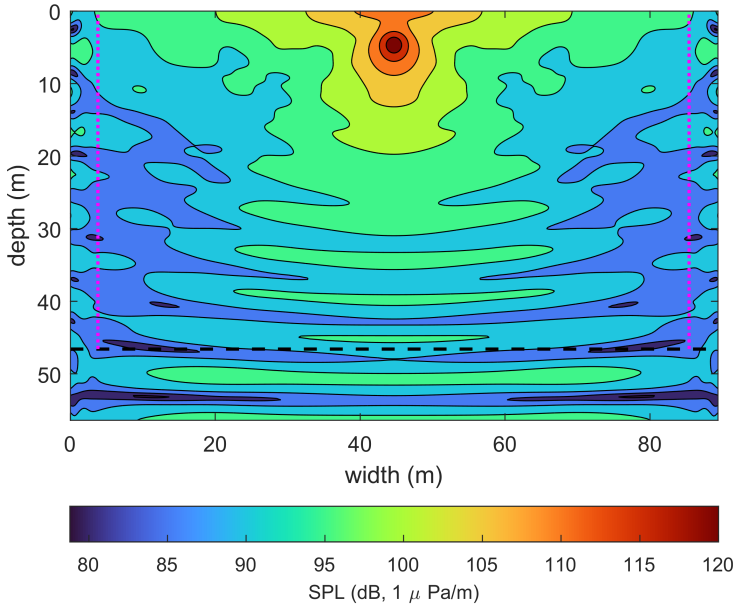

Figure 4.25: Shallow water environment with bedrock region under the sediment layer; RMS SPL contour with distance normalization for the y-z plane.

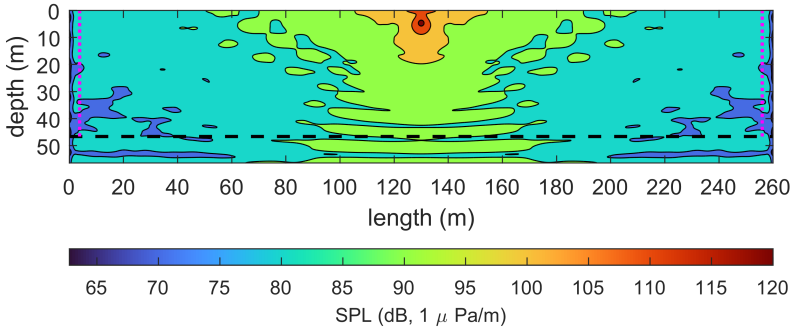

Figure 4.26: Shallow water environment with bedrock region under the sediment layer; RMS SPL contour with distance normalization for the x-z plane.

It is apparent from those figures that the highest pressure region appears around the sound source. It spreads along the upper boundary and the Z-axis through the sound source centre. The pressure distribution pattern is T-shaped. In the domain

corners along the length and width, the low-pressure zone of 70 dB appears. It is observed non-uniformity in individual zones, i.e. local pressure drops surrounded by a higher pressure area

The shallow water with bedrock under the sediment layer simulation outcome in normalized pressure levels for the rest of the measurement points i.e. points at 10 m, 20 m, 30 m, and 40 m, located at an angle of 45 ° from the plane of the source; the point lying on the axis of the sound source at a distance of 100 m; the receiver located centrally below the propeller at a depth of 46.4 m; the point located at the propeller's tip at the distance of 2.4 from the sound source; and a four-time simulations amplitude distribution snapshot for the two cross sections can be found in the Appendix B.1.

4.2.3.2 Shallow water with infinite propagation under a sediment

The second shallow water simulation covers the absorption layer under the sediment region, which mimics infinite propagation through the seabed.

The investigation covers the results presented in normalized Sound pressure levels in 1/3 octave bands. The 1 m distance normalized sound pressure level in 1/3 octave bands for probes at 120 m distance is shown in figure 4.27.

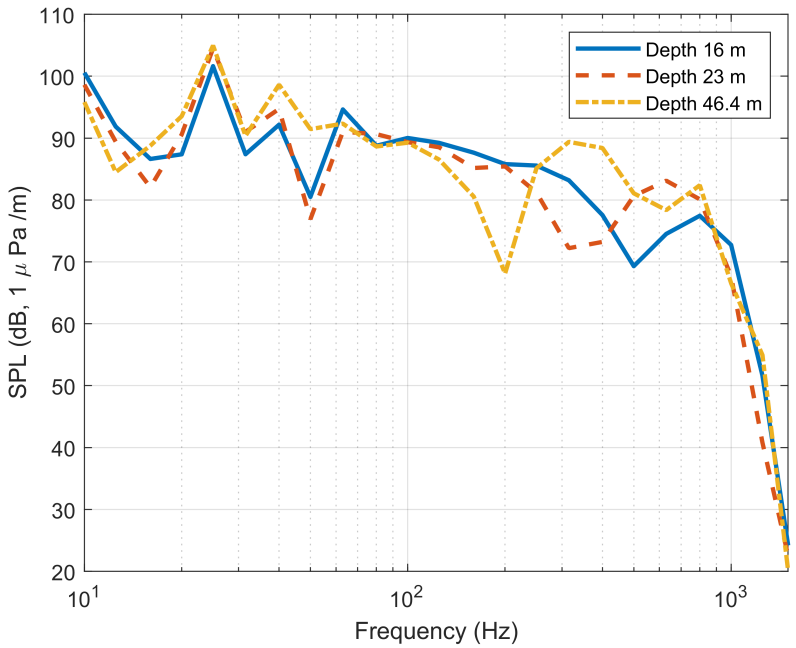

Figure 4.27: Normalized sound pressure level in 1/3 octave bands at 100 m

The normalized sound pressure level in 1/3 octave bands for probes at 120 m distance shows in figure 4.28

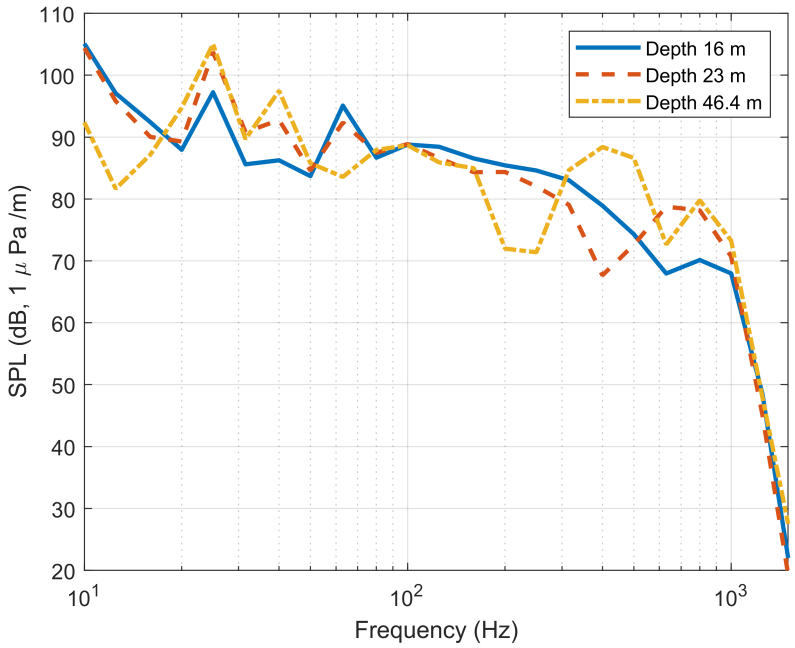

Figure 4.28: Normalized sound pressure level in 1/3 octave bands at 120 m

By analyzing the SPL figures presented above, it is visible that in both cases, the individual results of the hydrophones' depths are intertwined over bands of frequencies. There is no single-level dominant signal across all frequencies. For both measurement distances from the sound source, the measurements from the depth of 16 m and 13 m are characterized by a similar shape of the curves, while the draft of 46.4 m differs the most from the other curves' distribution. For this measuring depth, peaks and dips are visible in the distribution by frequencies that do not occur for the others depths.

The next simulation data concerns the SPL distribution over the spatial domain with a distance normalization of 1 m. The SPL along the x-y plane is presented in figure 4.29. Respectively, the cross-section in the x-z plane shows figure 4.30. The dashed black line in the figures corresponds to the sediment boundary, while the magenta-dotted line represents the boundary between the non-PML and PML regions.

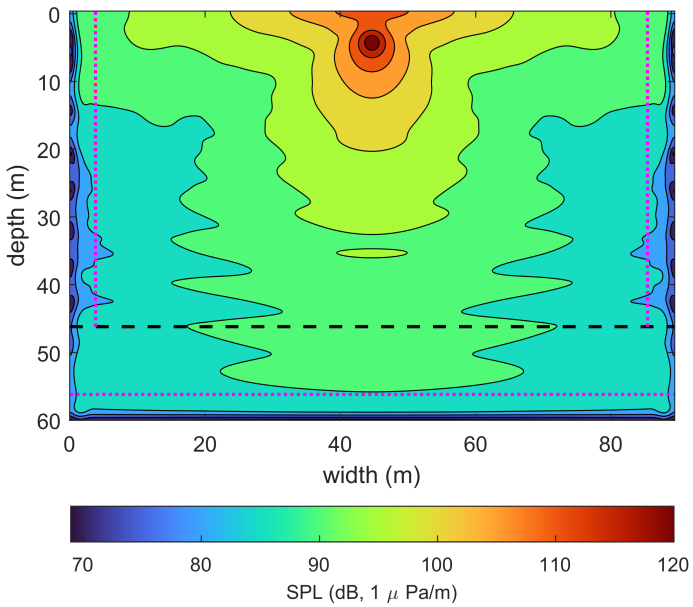

Figure 4.29: Shallow water environment with PML region under the sediment layer; RMS SPL contour with distance normalization for the y-z plane.

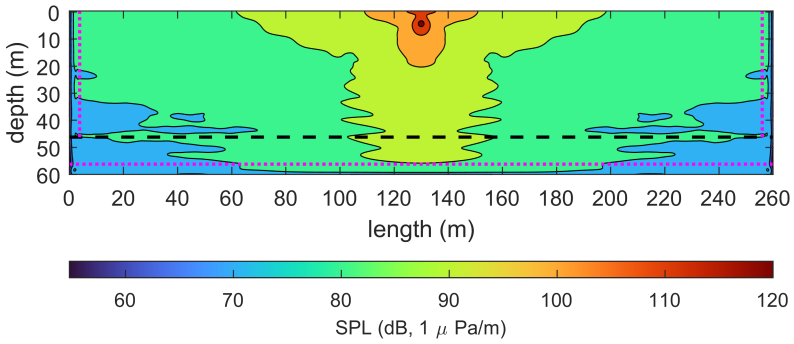

Figure 4.30: Shallow water environment with PML region under the sediment layer; RMS SPL contour with distance normalization for the x-z plane.

The results obtained from the figures above indicate a unique propagation pattern for the shallow water with infinite propagation under the sediment layer. The sound

source region has the highest SPL. The pressure is decaying with the distance increase. The pressure distribution close to the water surface is accumulated and spread over the width and length. An interesting pattern can be observed close to the sidewall from around the 12 depth to the domain z-direction peripheries. Namely, the low-pressure zone appears with a level of around 80 dB. Under the noise source, the mid-pressure level zone with a width of approximately 60 m performs up to the bottom of the PML layers. In contrast to the previous simulation, the reflective layer under the sediment is continuous.
The shallow water with infinite propagation simulation outcome in normalized pressure levels for the rest of the measurement points i.e. points at 10 m, 20 m, 30 m, and 40 m, located at an angle of 45 ° from the plane of the source; the point lying on the axis of the sound source at a distance of 100 m; the receiver located centrally below the propeller at a depth of 46.4 m; the point located at the propeller's tip at the distance of 2.4 from the sound source; and a four-time simulations amplitude distribution snapshot for the two cross sections can be found in the Appendix C.1.

4.2.4 Deep Water

The next experiment discusses the environment of deep water. The presented data follows the same calculation steps as in previous analyses. Progressing to the next test, the normalized SPL were used to analyse the relationship between hydrophones' depths and sound levels. The results for 100 m are shown in figure 4.31.

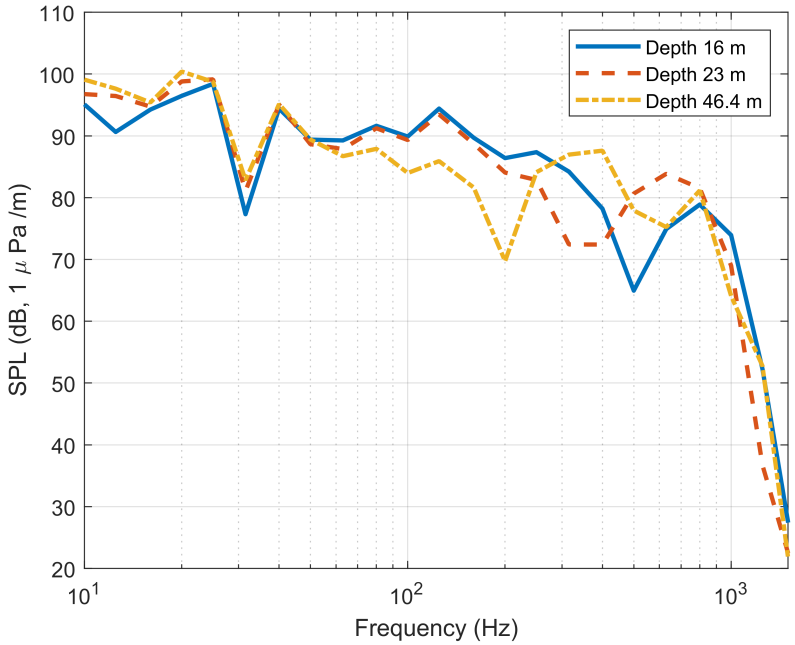

Figure 4.31: Normalized sound pressure level for open sea in 1/3 octave bands at 100 m

The normalized sound pressure level in 1/3 octave bands for probes at 120 m distance shows in figure 4.32.

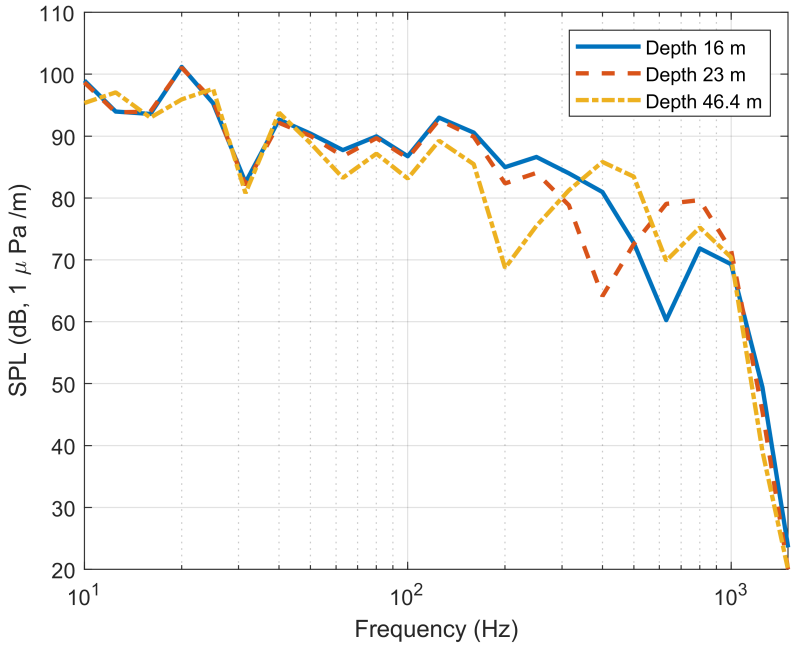

Figure 4.32: Normalized sound pressure level for open sea in 1/3 octave bands at 120 m

When analyzing the normalized SPL in 1/3 bands, it was observed that all probes delivered the same dip of about 35 Hz. In both cases, the measurement depths of 23 m and 16 m provided a similar curve shape. As already observed in the most recent simulations the depth of 46.6 deviates the most from the other measurement distances for the rounds. In both cases, measurements from a depth of 46.4 m are characterized by the lowest level in the range from about 50 Hz to 380 Hz. On the other hand, a sudden increase in energy from 200 Hz to 400 Hz has been observed.

As before, the last step of open sea research treats the pressure distribution over the spatial domain in two cross sections. The results for the y-z plane shows in figure 4.33 and for the x-z plane demonstrates in figure 4.34. The magenta dotted lines stand for the boundary of the PML region.

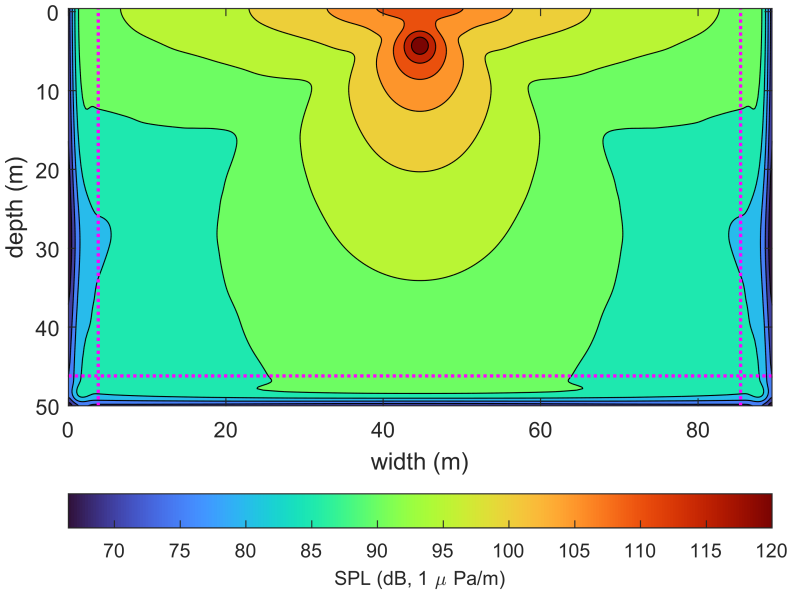

Figure 4.33: The deep sea simulation; RMS SPL contour with distance normalization for the y-z plane.

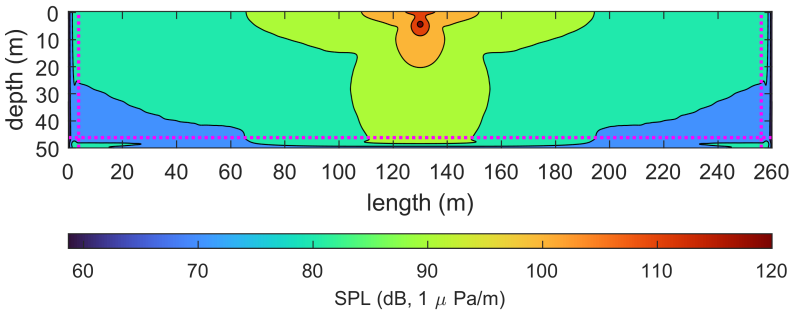

Figure 4.34: The deep sea simulation; RMS SPL contour with distance normalization for the x-z plane.

Overall, the open sea model differs from previous data. Mid and high pressure, i.e. from 90 dB to 120 dB, are distributed along the z-axis and over the centre of the sound source. In addition, when analyzing the x-z plane, the spread distribution

over the water surface is present. The values of the individual pressure sectors have flat contours boundaries between the pressure values, which results in a uniform distribution of the SPL. The 3-d sphere shape is observed with the centre at the source position and decaying pressure zones with the increase of distance. The pressure under the sound source in a band of about 55 m accumulates and spreads to different zones with various radii than in the x-z plane. Low-pressure areas around 60 dB appear in the corners of the x-z plane.

The deep water simulation outcome in normalized pressure levels for the rest of the measurement points i.e. points at 10 m, 20 m, 30 m, and 40 m, located at an angle of 45 ° from the plane of the source; the point lying on the axis of the sound source at a distance of 100 m; the receiver located centrally below the propeller at a depth of 46.4 m; the point located at the propeller's tip at the distance of 2.4 from the sound source; and a four-time simulations amplitude distribution snapshot for the two cross sections can be found in the Appendix D.1.

4.2.5 Canal

The following section deals with the results of the water canal environment. For the purpose, three different simulation conditions are presented. The purpose of that experiment was to analyse the influence of the various side wall properties, such as reflective walls and walls with sediment layers. In addition, the simulation with a water profile was provided to inspect the impact of various water properties.

4.2.5.1 Canal with fully reflective retaining walls

The first canal simulation covers the simulation of reflecting walls. The collected signals at the positions of the receivers of the two buoys at 100m in SPL normalized 1/3 frequency bands are shown in figure 4.35.

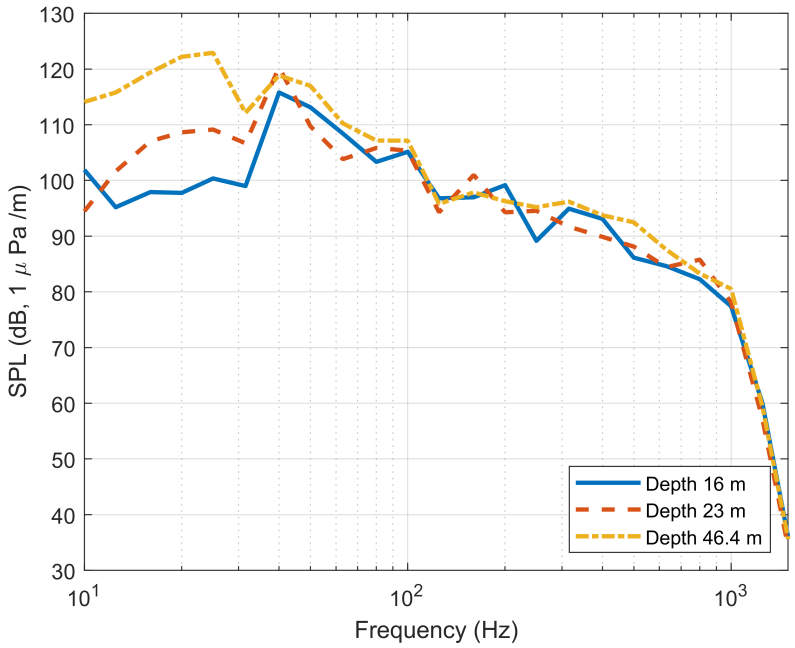

Figure 4.35: Normalized sound pressure level in 1/3 octave bands at 100 m

The normalized sound pressure level in 1/3 octave bands for probes at 120 m distance shows figure 4.36

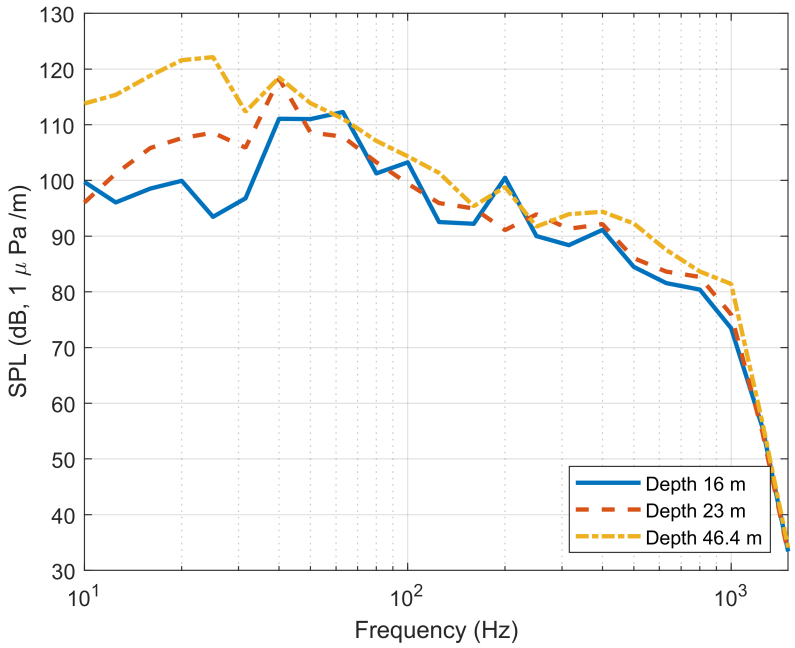

Figure 4.36: Normalized sound pressure level in 1/3 octave bands at 120 m

From the normalized SPL figures 4.35, 4.36, it can be seen that the depth of 46.6 has the highest level in the range of 10 Hz to 105 Hz for 100 m and from 10 Hz up

to 50 Hz for 120. Moreover, some peaks are present in the 16 m depth probe for 120 m, which do not appear at 100 m distance.

In terms of examining the acoustic pressure map distribution, the RMS SPL with distance normalization is executed and illustrated in figure 4.37 for the y-z plane and figure 4.38 for the x-z plane. The magenta dotted line represents the PML region threshold, whereas the dashed black line represents the sediment boundary.

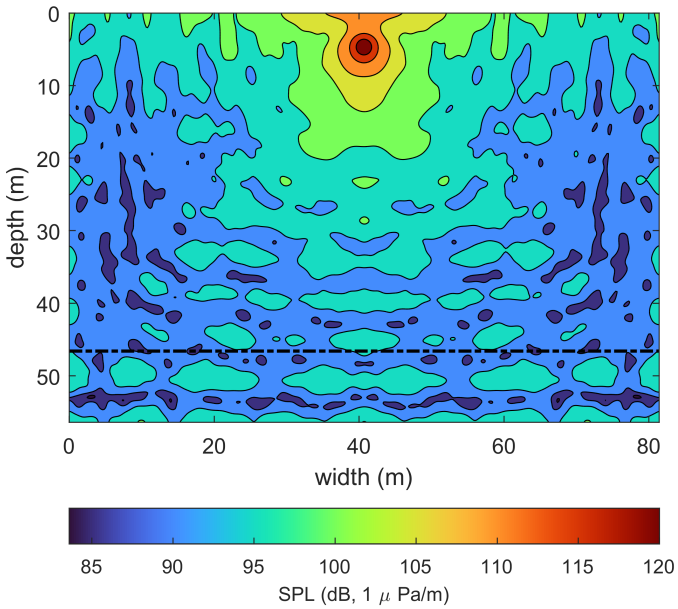

Figure 4.37: Canal with fully reflective walls; RMS SPL contour with distance normalization for visualization of the y-z plane.

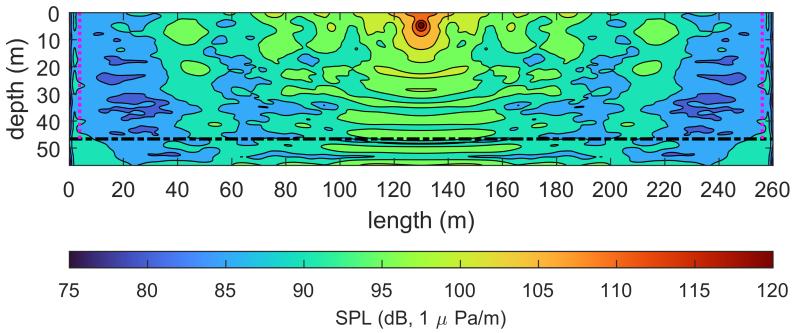

Figure 4.38: Canal with fully reflective walls; RMS SPL contour with distance normalization for visualization of the x-z plane.

Further analysis showed that medium and low-pressure areas are intertwined. Therefore, sector boundaries have jagged characteristics. The flattening pattern of the pressure areas in the sediment layer and close to the walls is noticeable. By comparing the data with the results from previous simulations, it is visible that when considering the water channel, the pressure areas are more mixed.

The water canal simulation with reflective side walls outcome in normalized pressure levels for the rest of the measurement points i.e. points at 10 m, 20 m, 30 m, and 40 m, located at an angle of 45 ° from the plane of the source; the point lying on the axis of the sound source at a distance of 100 m; the receiver located centrally below the propeller at a depth of 46.4 m; the point located at the propeller's tip at the distance of 2.4 from the sound source; and a four-time simulations amplitude distribution snapshot for the two cross sections can be found in the Appendix E.1.

4.2.5.2 Canal with sediment walls

The second canal setup covers the test when a sediment layer is applied to the walls.

The results from hydrophones at 100 m performed in Sound Pressure Level shows in figure 4.40.

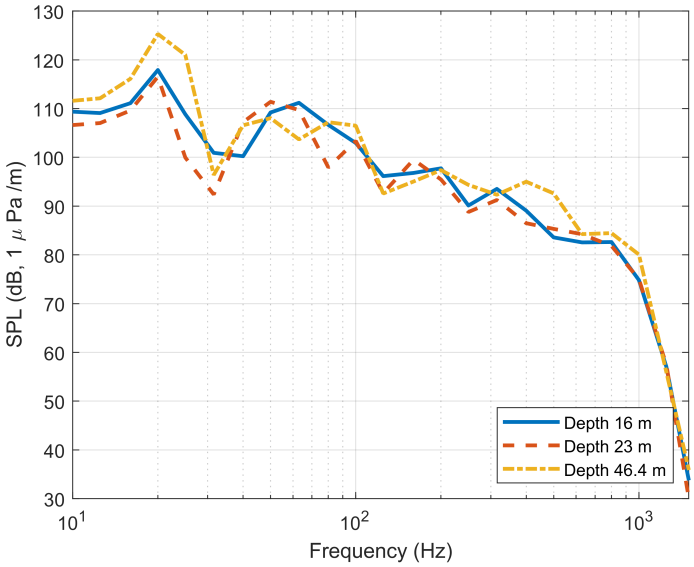

Figure 4.39: Normalized sound pressure level in 1/3 octave bands at 100 m

The normalized sound pressure level in 1/3 octave bands for probes at 120 m distance shows figure 4.40.

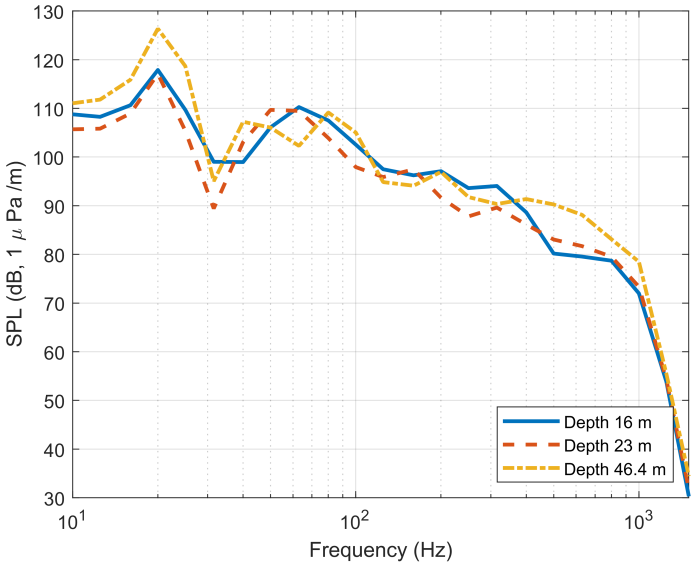

Figure 4.40: Normalized sound pressure level in 1/3 octave bands at 120 m

When considering the low-frequency range, the hydrophone is located at 23 m for both buys. The dip for all hydrophones shows a positive correlation between 20 Hz and 40 Hz. It is apparent from the figures above how the records from the buoy placed at 120 m have spikey curves. In contrast, the buoy located closer to the sound source has smooth distribution.
The next analysis step concerns acoustic pressure maps. Figure 4.41 shows the RMS SPL with distance normalization for the y-z plane, while figure 4.46 visualises the

pressure map for the x-z plane. The magenta dotted line stands for the boundary of the PML region, whereas the dashed black line represents the sediment boundary. The yellow dashed line denotes the sediment wall.

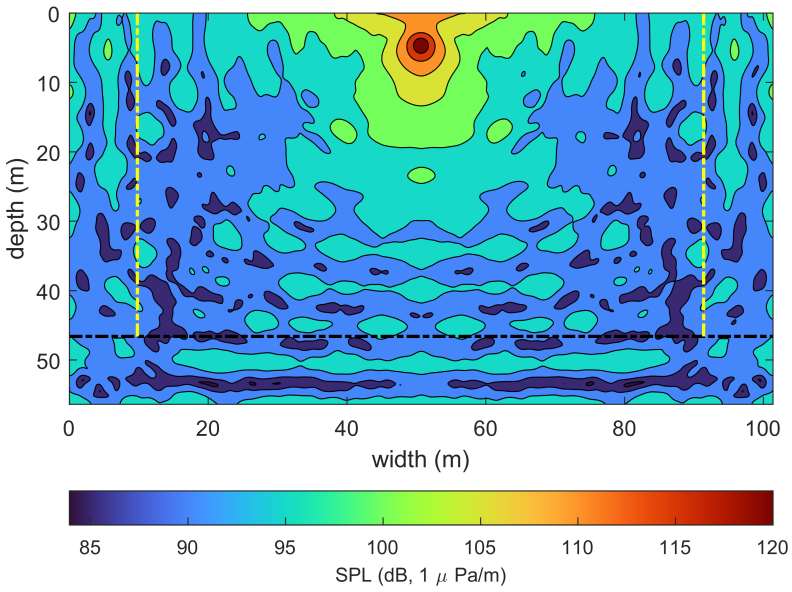

Figure 4.41: Canal with sediment walls; RMS SPL contour with distance normalization for visualization of the y-z plane.

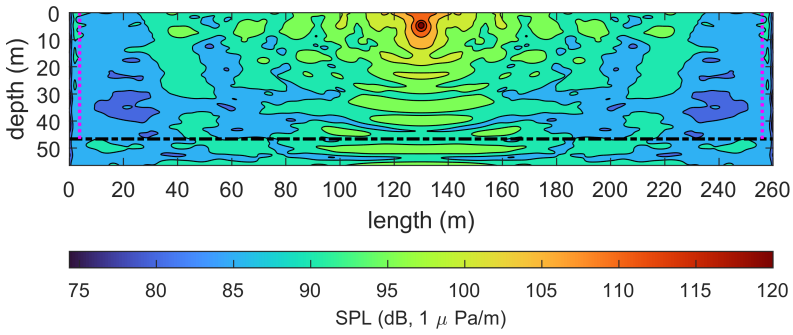

Figure 4.42: Canal with sediment walls; RMS SPL contour with distance normalization for visualization of the x-z plane.

What stands out from the pressure distribution plots is that the pressure pattern for the reflective canal is similar to that of the canal with sediment walls. The same dependencies appear in the interweaving of spheres of low and medium pressure. It is also visible in the pattern flattening phenomena in the sediment walls and canal bed.

The water canal with sediment walls simulation outcome in normalized pressure levels for the rest of the measurement points, i.e. points at 10 m, 20 m, 30 m, and 40 m, located at an angle of 45 ° from the plane of the source; the point lying on the axis of the sound source at a distance of 100 m; the receiver located centrally below the propeller at a depth of 46.4 m; the point located at the propeller's tip at the distance of 2.4 from the sound source; and a four-time simulations amplitude distribution snapshot for the two cross sections can be found in the Appendix F.1.

4.2.5.3 Canal with sediment walls and various water properties

The last canal simulation setup discusses the various water profile.

As in previous research, the normalized sound pressure levels are compared. The normalized SPL for 100 m distance receivers is shown in figure 4.43

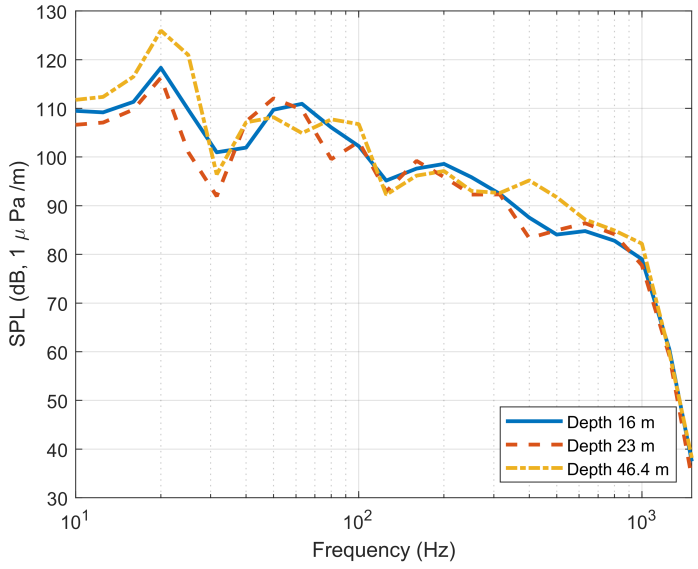

Figure 4.43: Normalized sound pressure level in 1/3 octave bands at 100 m

The normalized sound pressure level in 1/3 octave bands for probes at 120 m distance shows figure 4.44

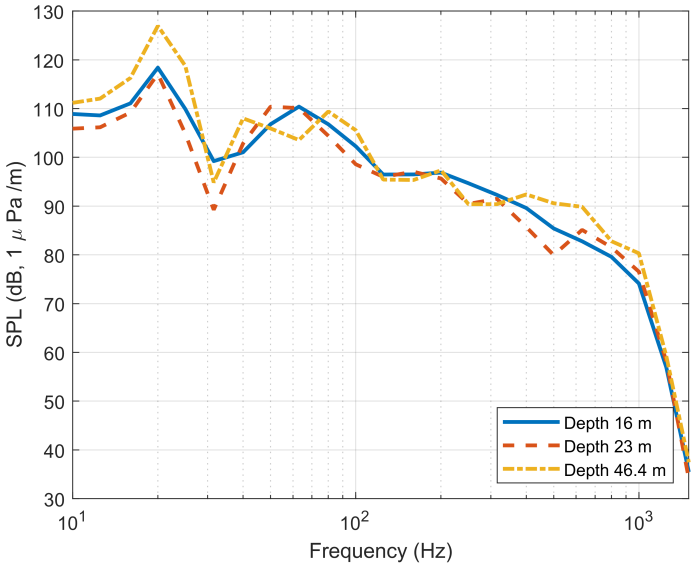

Figure 4.44: Normalized sound pressure level in 1/3 octave bands at 120 m

By looking at the normalized SPLs for 100 m and 120 m distances, it can be noticed that all measurements delivered dips around 30 Hz. At both distances, the lowest pressure with a noticeable dip comes from the probes placed at 23 m depth.
No significant change is observed in comparison to the previous simulation case with sediment layer walls. However, slight inconsistencies can be noticed. For instance, moderately more noise is observed.

As before, the further step of water tunnel research treats the pressure distribution over the spatial domain in two cross sections. The results for the y-z plane are shown in figure 4.45 and for the x-z plane is demonstrated in figure 4.46. The magenta dotted line stands for the boundary of the PML region, whereas the dashed black line represents the sediment boundary. The yellow dashed line denotes the sediment wall.

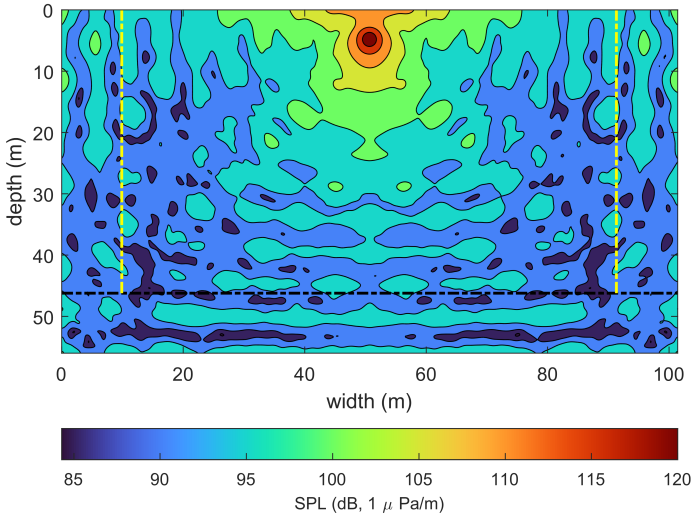

Figure 4.45: Canal with sediment walls and various water profile; RMS SPL contour with distance normalization for visualization of the y-z plane.

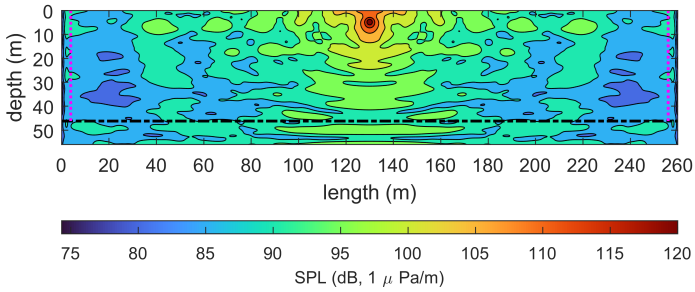

Figure 4.46: Canal with sediment walls and various water profile; RMS SPL contour with distance normalization for visualization of the x-z plane

An analysis showed that the medium and low-pressure areas are intertwined. There-

fore, the jagged characteristics of the sector boundaries are present. The flattening pattern of the pressure areas in the sediment layer, close to the walls, and around the depth of 15 m is noticeable.
The water canal with sediment walls and various water profile simulation outcomes in normalized pressure levels for the rest of the measurement points, i.e. points at 10 m, 20 m, 30 m, and 40 m, located at an angle of 45 ° from the plane of the source; the point lying on the axis of the sound source at a distance of 100 m; the receiver located centrally below the propeller at a depth of 46.4 m; the point located at the propeller's tip at the distance of 2.4 from the sound source; and a four-time simulations amplitude distribution snapshot for the two cross sections can be found in the Appendix G.1.

4.2.6 Average Sound Pressure Levels

The preceding chapters focused on each simulation result for the overall analysis of the data collected in table 4.2. The measurement positions were taken at various depths and distances. The table consists of the buoys at 100 m and 120 m; a point of recorded pressure positioned at the bottom directly under the sound source; and two radii 20 m and 40 m from the sound source symmetrically to the x-z plane in the middle of the y-axis. The presented SPLs are normalized by 1 m and p_{ref}= $1\mu Pa$ by using the RMS over the whole simulation time.

Table 4.2: Average Sound Pressure Levels.

Location		Cavitation tunnel (dB)	Shallow water with bedrock (dB)	Shallow water with PML (dB)	Open sea (dB)	Canal with reflective walls (dB)	Canal with sediment walls (dB)	Canal with variable water profile (dB)
Bouy 100 m	depth 16 m	90.26	86.62	83.75	83.68	90.01	90.17	89.61
	depth 23 m	86.32	81.67	82.75	82.38	85.69	86.69	87.53
	depth 46,4 m	90.46	80.21	81.56	78.63	86.11	85.53	85.48
Bouy 120 m	depth 16 m	87.63	80.58	82.25	82.00	86.33	87.61	87.16
	depth 23 m	87.55	83.55	80.21	80.93	85.38	87.10	87.60
	depth 46,4 m	91.88	82.50	80.27	77.72	89.30	89.76	90.27
Propeller centre	depth 46,4 m	100.96	93.40	93.14	92.14	97.47	91.84	92.58
100 m	depth 4,8 m	91.98	83.92	85.44	85.23	91.12	91.16	92.02
Point 1	r=20m	100.31	96.11	94.53	94.13	97.47	98.81	99.98
Point 2	r=20m	100.44	96.25	94.67	94.26	97.52	99.03	99.99
Point 3	r=40m	96.98	90.10	87.59	87.30	90.76	93.39	93.50
Point 4	r=40m	97.10	89.92	87.73	87.38	90.86	93.04	93.49

General trends in pressure distribution in the simulated environment can be found by examining the table 4.2. In most cases, the highest levels are observed at points located at the bottom of the source or centred on the bottom.
What is most interesting, based on the table above, is that not all simulations follow the rule of pressure decay with distance.
Further analysis shows that in cavitation tunnel simulation, shallow water with bedrock, canal with reflection walls, and canal with sediment walls equipped with variable water profile simulations, the probes at depth 46.4 at 120 have slightly higher SPL than the probe at the same depth placed closer to the sound source. Therefore, there is a correlation between 10 m of sediment and the reflecting surface below. That influence is distinguishable at a depth of 46.6 m at a distance of 120 m. When analyzing the shallow water with bedrock, the difference is around 2 dB, whereas, for the canal simulations, it oscillates in a range of 3-4 dB. By focusing on

canal simulation cases where the domain edges along the y-axis are reflective, the sediment with specific properties could technically decrease pressure. Nevertheless, a significant increase in energy has been observed at many measurement points following the application of the sediment region on the sides. Regarding the various water profiles in comparison to the homogeneous water, there is a decrease in SPL that appears only at 16 m depth for 100 m and 16 m and 23 m depth for 120 m distance.
A similar pattern of motion is observed in the cavitation tunnel and the shallow water with bedrock for probes at 23 m. The pressure increase at 120 m is probably due to the reflections and interference between the sediment and bedrock at the depth of 23 m. The Sound pressure level increases around 1 dB for 120 m related to 100 m.
At a depth of 16 m, all results have a higher level at 100 m than at 120 m and the decay grows with the distance.
The highest levels for individual simulations indicate the point placed centrally under the sound source, except for water canal simulations, where excessive pressure has points located at radii 20 m or 40 m from the propeller positions.
In terms of shallow water simulations, surprisingly, the results for the shallow water simulation with infinite propagation do not provide lower pressure for all measurement points when the bedrock under the sediment is applied.
Interestingly, when analyzing the series measurement of points located 20 m and 40 m from the source, it can be seen that the SPL results from the same distance are slightly different. The difference in levels is about 0.12-0.14 dB.

5

Discussion

The current study found that the applied FDTD approach for 3-dimensional underwater simulation works and provides appropriate results within the examined range of interest. Employing absorbing PML layers allows for simulated infinite propagation, which supplies minor numerical reflections. Apart from that, the code implementation for propagation through various materials, such as seabed or canal walls, permits the simulation of simplified models of different physical environments, such as water canals or shallow water. The performed simulation method showed that it can be used for underwater sound propagation analysis. However, despite positive results, this research confirmed many FDTD limitations. The most prominent drawback concerns the computational burden and grid sizes. That factor is strongly related to the accuracy and the maximum frequency of interest. The initial assumption referred to the high frequency of this study was not completed due to the impossibility of simulating due to the computer memory limitation. Implementing the physical domain dimensions for recreation of the physical environment proportion and simultaneously keeping the high resolution of the maximum frequency, e.g. 2000 Hz, was not computationally feasible even for a high-memory computer cluster. Prior studies that have noted the importance of having the accuracy feature correlated to the wavelength of the maximum frequency should be at least divided by 10 to determine the spatial step. That assumption arises to be accurate in what was tested in this paper too. As a rule of thumb, bearing in mind the sufficient division of wavelength and having the high frequency of interest and tested domain dimensions generate a massive node amount through domain dimensions. Such dependencies initiate great computational effort and usage of RAM resources. In addition, extra simulation attributes applications such as propagation through various mediums or materials and PML conditions significantly increase the simulation time.

The results of this study confirmed that numerical dispersion is one of the main disadvantages of FDTD methods. It is because FDTD uses second-order accuracy in time and space, which causes the speed of the sound to be not constant but frequency dependent. The phenomenon is most visible when receivers are placed along the Cartesian grid. However, positioning the receivers along the diagonals can significantly reduce the effects of speed propagation inconsistency. Additionally, the errors associated with the dispersion are present in the high-frequency range, in other words, above the limit frequency where the spatial discretisation steps are too coarse. To reduce artefacts and numerical dispersion source function, for example, a Gaussian pulse can be used. This causes significantly fewer dispersion effects than the Dirac source.

The measuring point positions were established using two standards. However, not

all probes were possible to position in the analyzed domains, which results from domain sizes. Moreover, the standards determine the receiver positions depending on environmental conditions measurement. Therefore, due to the behaviour investigation in different environments and the impact of individual simulation conditions on the results, identical probes positions were used for all the simulations tested, which is inaccurate for all probe positions under the following standards.

Another crucial factor that may influence the analysis of physical measurements or computer simulations is the reference point. As shown in the results section, the points placed at a distance of 1 m from the source are not identical. They could deviate from the results while considering normalization values. It determines when further analysis is needed and involves reference points. The discrepancies between the points are likely from the distance to the water surface and the reflections or sound source interference at the receivers' positions. In addition, the same propagation issue of acoustic waves in FDTD is observed for points placed in the far field. While the sound source is ideally situated in the middle of the domain concerning the x and y axes, the measurement points set at identical distances did not provide the same results. That indicates that FDTD simulation propagation is not perfectly symmetrical, and the wave does not propagate equally in all directions.

By analyzing the results of the radiated sound from individual simulations, it is noticeable that there are some trends present. From the measurements of the results from 100 m and 120 m, it is seen that, in general, the pressure curves' distribution is getting smothered at a distance of 120 m, which results from the fact that the wave front before it reaches further distant measurement points, undergoes dispersion and energy decay distribution in frequency bands has a lower value. The current study found that the cavitation tunnel results provide the highest sound levels for most of the tested hydrophones' positions in comparison to the other simulations. In contrast, as expected, the lowest pressure levels have the simulation of the deep sea. It is certainly related to the reflections and the amount of energy scattering in the system.

Technically, considering canal simulations, layers of sediment should absorb energy. This is usually manifested by a decrease in energy in the range of 20-50 Hz while analysing the SPL in the frequency range. Indeed, the waterway average SPLs from given measurement positions are lower in most of the positions compared to the fully reflective cavitation tunnel simulation. On the other hand, there are slight deviations at a few measuring points when the examined canal is covered with sediment layers and has a variable water profile.

The cross-section pressure contours show that the area of the region of medium pressure (95 dB) at 20 m depth to the bottom is decreasing, when bottom sediment is present, relating to the cavitation tunnel. The current data find that sediment on the side walls does not decrease the overall area of acoustic pressure by assuming this particular domain geometry. In addition, there is denser material on the side walls than the bottom material. To sum up, it is most likely that particular sediment properties do not change the overall pressure distribution to a significant extent.

The water profile shows a slight decrease in SPL. The sudden change in water properties at 15 m is visible through the flattening of the pressure regions.

In contrast, the water canal with reflective sidewalls has relatively low-pressure

regions (around 75 dB) at 60 m from the sound source. However, regions with a pressure range of around 85 dB have a much greater influence than simulation cases with applied sediment layers.
In summary, by comparing the shallow water with a reflective layer under the sediment and with the PLM region. The energy is not lower for all measurement positions when the PML layers are applied. The pressure distribution over the two domains varies quite significantly. The results for shallow water with a reflective layer under the bedrock deliver the pressure gradient from low to mid values close to the sediment layer. In contrast, the pressure distribution for the shallow water with PML, especially in the z-x plane, is similar to the pressure distribution for the deep water simulation. However, the influence of the sediment layer is noticeable, e.g. by scattering, which is manifested by the jagged contours, principally in the region close to the water surface.
Surprisingly, higher pressure, when using sediment at the walls, was found for a radius of 20 m and 40 m from the propeller centre. This finding was unexpected and indicates that the sidewalls' sediment slightly amplifies the pressure at 20 m and 40 m. However, the contour maps of pressure explain this phenomenon. Where, for example, at a distance of 20 m there are local pressure drops.
It should be noted that the simulation method used is not the most efficient method and some more optimization and improvement could enhance the computational time. However, this method implementation could be a helpful tool and an excellent base for development regarding underwater sound propagation in constrained domains. Similar attempts were made by G. Petris et al. [26] using open sea and channel simulations examining the influence of a fully reflective boundary condition and a fully absorbent boundary condition on the open sea and the channel. That research treats the simplified model with approximately five times bigger spatial steps than this study. It also uses a hard-source approach, which is not the most appropriate choice for describing sound propagation due to its unphysical characteristics. Thus, as a result, the authors [26] provided pressure distribution patterns over the spatial domain. Despite different simulation circumstances some similarities in the pressure distribution are observed, although generally, the pressure contours in this study are more jagged and distorted.

5.1 Improvement and further studies

Naturally, the study did not cover all possible application features or simulation setups. Further consideration, optimization may result in code improvement and performance.
First of all, the most outstanding development is computational speed. In this study, the unstaggered leapfrog approach was used, which is not the most convenient in terms of memory use. However, it is straightforward in implementation and building on additional code features. On the other hand, the NPML method was applied, which is a less computational burden in contrast to standard PML implementation. With that in mind, some code optimization is required and certainly would help speed up the computation process and performance. Another upgrade could be, among others, carrying out variable profiles of the mediums by adding deviations

of structure properties and mixed shapes, e.g. additional random absorbing or reflecting regions in the sediment layer or non-regular changes in the cross-section of the water. Another factor may be the simulation of turbulent flow. A next development may be the involvement of different profiles and shapes of the river/canal or the mixed surface of the seabed. Another customization can be simulating the hull geometry, which certainly can introduce more reflections in the first phase of sound propagation. Moreover, the employment of immersed boundaries method with variable intermediary properties on the media boundary is probably another upgrade.
The comparison of the simulation of the cavitation tunnel and the simulation with a scaled cavitation tunnel shows that the pressure distribution across the cross-section differs significantly. Regardless, the scaled model can be useful for understanding the main pressure distribution patterns.

6
Conclusion

The main goal of the current study was to determine the behaviour of different simulation environments and compare it to the set of identical geometrically located measurement points for various simulation environments.
In general, using the 3-d FDTD underwater simulation provides appropriate results up to the tested limit frequency. The differences between simulated conditions are noticeable in waveforms, frequency spectra and sound pressure levels. The simulated physical environment delivered the unique SPL distribution patterns for each case. In conclusion, it demonstrated that the sediment layer could not always provide pressure reduction. However, this issue depends on the location of the receivers because the influence of sediment or combination with side walls could result in a local decrease or increase in energy. Moreover, a crucial factor for acoustic reflection, scattering and interference and hence increase or decreased energy, is the domain geometry and domain sizes. In particular, the impact on acoustic propagation and energy distribution has sediment properties such as thickness, density or speed of sound in the sediment.
The studied environments showed that the planning of measuring points should include the unexpected pressure distribution consideration, e.g. measuring points placed in the far field or for the sample placed on the bottom.
The research has also shown that the measuring points should be set individually for each tested environment due to the regions where the pressure is higher than expected. Therefore, the sediment properties should be considered for planning the hydrophones' positions. To sum up, unique pressure distribution patterns are present and measurement point readings could vary depending on the environment. In conclusion, the FDTD solver improvement and optimization are needed to get a fully accurate and reliable tool.

Bibliography

[1] L. Sheng. Wang, K.D. Heaney, P.D Theobald, et al., "Review of underwater acoustic propagation models", *National Physical Laboratory*, 2014.

[2] S. Wang, "Finite-difference time-domain approach to underwater acoustic scattering problems", *The Journal of the Acoustical Society of America* 99(4), 1996.

[3] E.T. Methratta, A. Hawkins, B.R. Hooker,A. Lipsky, J.A. Hare, "Offshore Wind Development in the Northeast US Shelf Large Marine Ecosystem: Ecological, Human, and Fishery Management Dimensions", *Oceanography*, vol.33, No.4, pp.16-27, 2020.

[4] J. A. Hildebrand, "Anthropogenic and Natural Sources of Ambient Noise in the Ocean", *Marine Ecology Progress Series*, 395, pp. 5-20, 2009.

[5] J. Carlton, "Marine Propellers and Propulsion", *Butterworth-Heinemann*, Third edition, Great Britain,pp.255-260, 2012.

[6] G. Tani, M. Viviani, M. Felli, F. H. Lafeber, T. Lloyd, B. Aktas, M. Atlar, S. Turkmen, H. Seol, J. Hallander, et al., "Noise measurements of a cavitating propeller in different facilities: Results of the round robin test programme", *Ocean Engineering* 213 ,2020

[7] J. B. Schneider,"Understanding the Finite-Difference Time-Domain Method", *School of Electrical Engineering and Computer Washington State University*,2010 www.eecs.wsu.edu/ schneidj/ufdtd (accessed 22.01.2022)

[8] V. E. Ostashev, K. Wilson, "Wave-based time-domain methods," in Acoustics in Moving Inhomogeneous Media. *Taylor and Francis Group*, 2 edition, pp 427-447, 2016.

[9] W. Hu, A. Abubakar, T. M. Habashy, "Application of the nearly perfectly matched layer in acoustic wave modeling", *GEOPHYSICS,VOL. 72, NO. 5* September-October 2007.

[10] D. K. Wilson. L. Liu. "Finite-Difference, Time-Domain Simulation of Sound Propagation in a Dynamic Atmosphere" *US Army Corps of Engineers*, 1 edition, 2004.

[11] T. Van Renterghem "Efficient outdoor sound propagation modeling with the finite-difference time-domain (FDTD) method: a review" *Acoustics Group, Department of Information Technology, Ghent University*, Belgium 2014.

[12] Q.H. Liu, J. Tao,"The perfectly matched layer for acoustic wavesin absorptive media", *The Journal of the Acoustical Society of America 102*, 2072, 1997.

[13] X. Yuan, D. Borup; J.W. Wiskin, M. Berggren, R. Eidens, S.A. Johnson, "Formulation and Validation of Berenger's PML Absorbing Boundary for the FDTD Simulation of Acoustic Scattering" *IEEE Transactions on ultrasonics, ferroelectrics, and frequency control* vol. 44, no. 4, July 1997.

[14] J. Sheaffer, M. Van Walstijn, B. Fazenda, “A physically-constrained source model for FDTD acoustic simulation" , *Conference on Digital Audio Effects*, 2012.

[15] K. Abrahamsen, “The ship as an underwater noise source", *Proceedings of meetings on acoustics Acoustical Society of America*, 2012

[16] V.Bertram, “Experimental Approach" in Practical Ship Hydrodynamics, *Elsevier Science*, Second edition.pp 60-62 2011

[17] B. Katsnelson, V. Petnikov, J. Lynch, “What Is Shallow Water Acoustics?" in Fundamentals of Shallow Water Acoustics, *Springer*,pp 1-16, 2012.

[18] L. Jin-Yuan, H. Chen-Fen, S. Shiahn-Wern, “Effects of seabed properties on acoustic wave fields in a seismo-acoustic ocean waveguide", *Ocean Engineering 28*, 1437–1459, 2001.

[19] M. Ge, U. Svennberg, R.E.Bensow, “Investigations on prediction of ship noise using the FWH acoustic analogy with incompressible flow input", *Ocean Engineering*,257,2022.

[20] Det Norske Veritas Germanischer Lloyd, Class guideline for “Measurement procedures for noise emission ",2019

[21] Bureau Veritas “Underwater Radiated Noise" *RULE NOTE NR 614*, 2018.

[22] D. K. Wilson, V. E. Ostashev, S. L. Collier, N. P. Symons, D. F. Aldridge, D. H. Marlin, “Time-domain calculations of sound interactions with outdoor ground surfaces" *Applied Acoustics 68*, 2007.

[23] L.Bjørnø, “Scattering from the seabed?" in Applied Underwater Acoustics, *Elsevier*,pp 318-337, 2017.

[24] H. Igel, “Analytical solutions: scalar wave equation" in Computational Seismology: A Practical Introduction, *Oxford University Press*,First edition,pp. 19-22 2017.

[25] B.A. Jones, “Echo statistics of aggregations of scatterers in a random waveguide: Application to biologic sonar clutter", *Naval Postgraduate School*, 2012

[26] G. Petris, M. Cianferra, V. Armenio, “Marine Propeller Noise Propagation within a Shallow Water Environment", *Marine 2021*, 2021

A

Appendix 1: Cavitation Tunnel

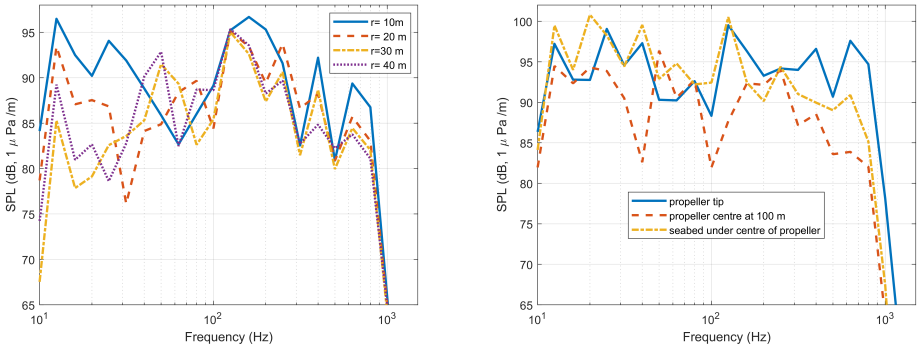

Figure A.1: Cavitation tunnel Sound pressure levels for additional points in 1/3 bands.

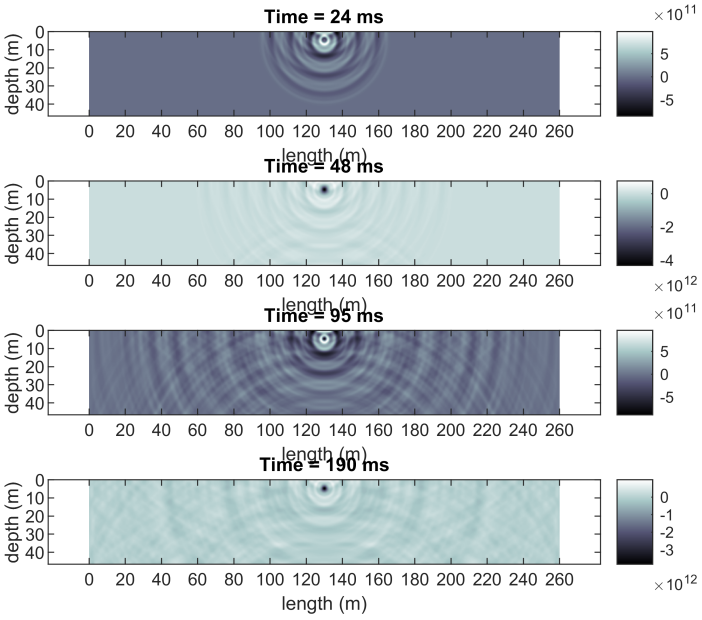

Figure A.2: Cavitation tunnel simulation; visualisation of sound propagation of four-time intervals in the x-z plane.

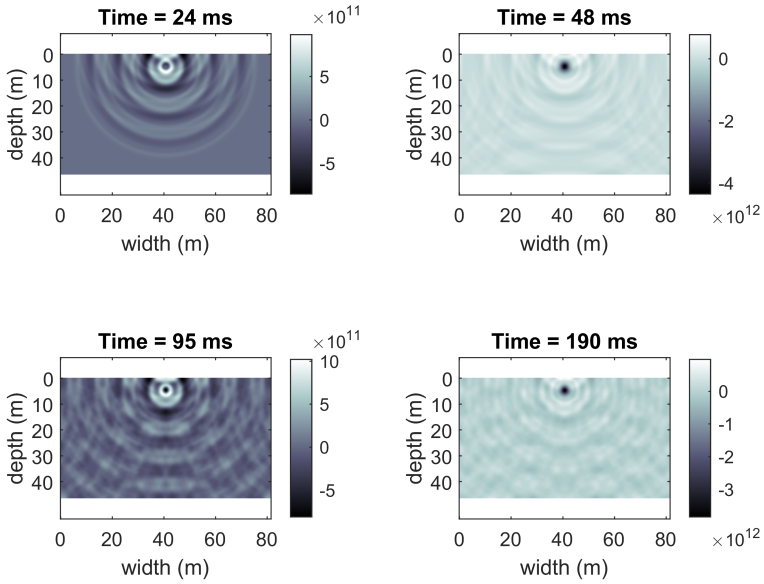

Figure A.3: Cavitation tunnel simulation; visualisation of sound propagation of four-time intervals in the y-z plane.

B

Appendix 2: Shallow water with bedrock

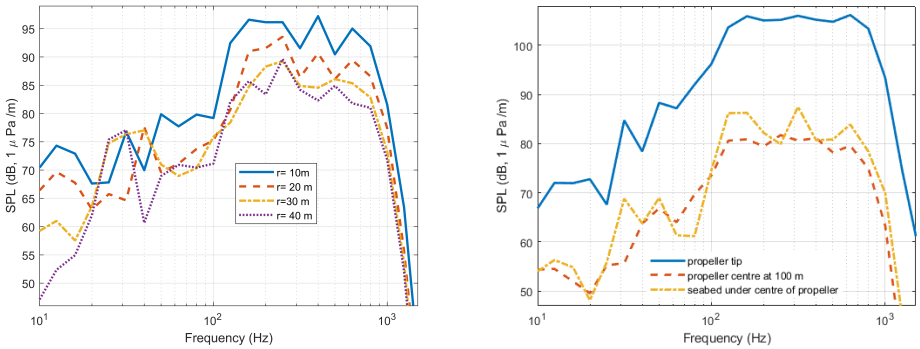

Figure B.1: Shallow water with bedrock; Sound pressure levels for additional points in 1/3 bands.

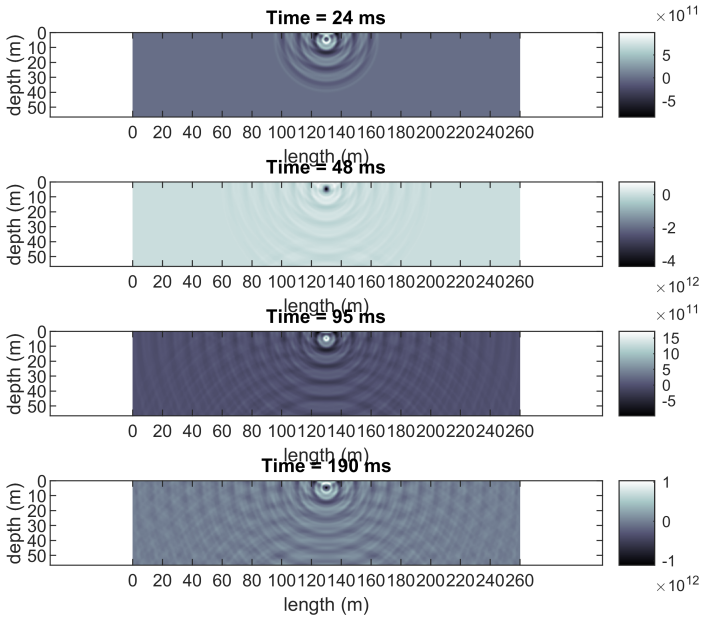

Figure B.2: Shallow water with bedrock; visualisation of sound propagation of four-time intervals in the x-z plane.

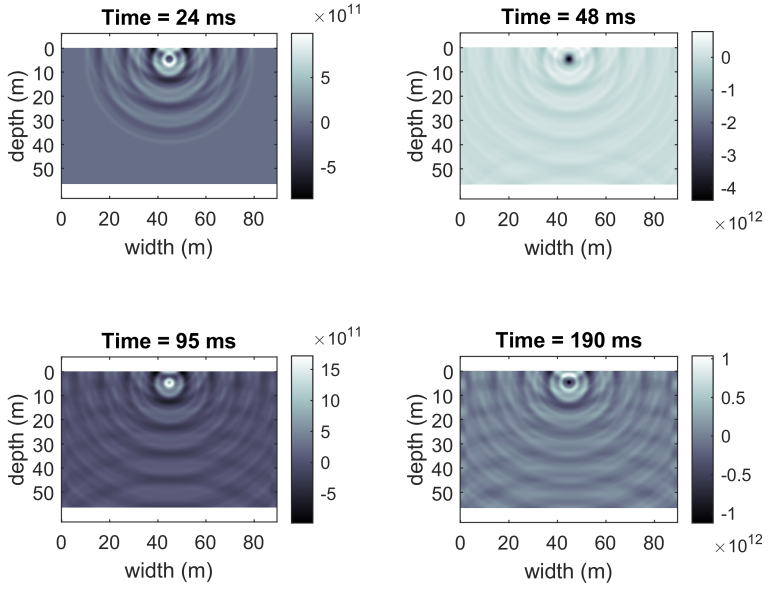

Figure B.3: Shallow water with bedrock; visualisation of sound propagation of four-time intervals in the y-z plane.

C

Appendix 3: Shallow water with infinite propagation under a sediment

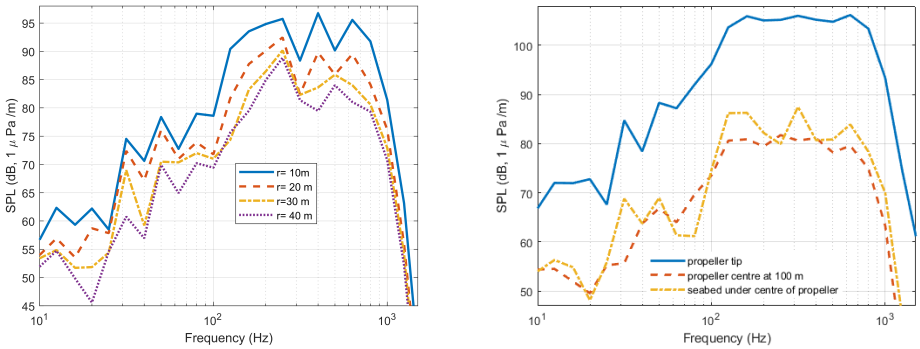

Figure C.1: Shallow water with infinite propagation under a sediment;Sound pressure levels for additional points in 1/3 bands.

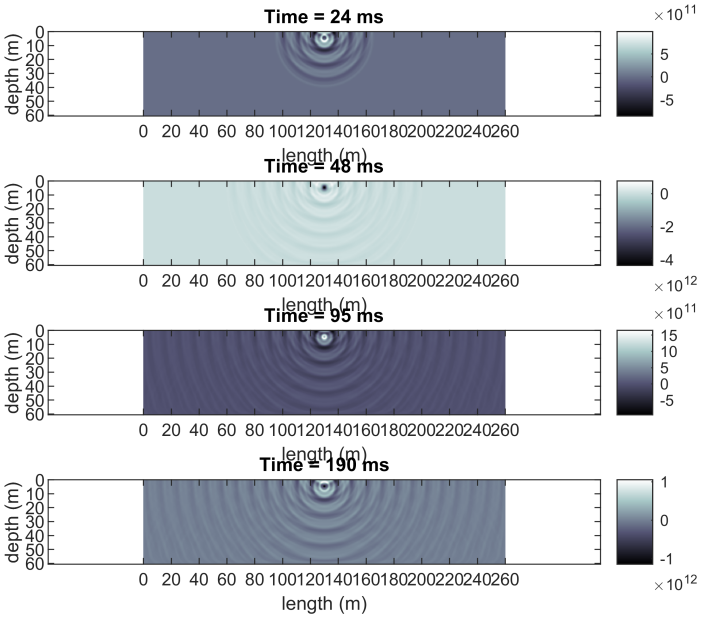

Figure C.2: Shallow water with infinite propagation under a sediment; visualisation of sound propagation of four-time intervals in the x-z plane.

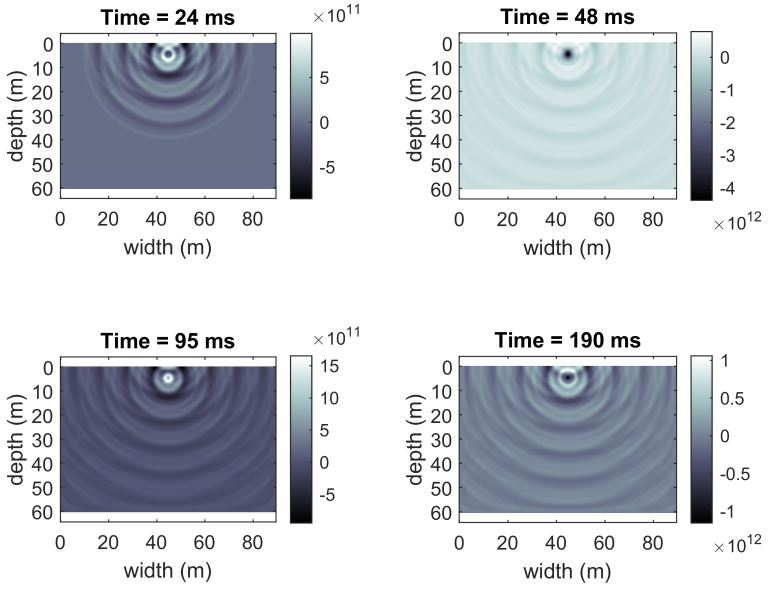

Figure C.3: Shallow water with infinite propagation under a sediment; visualisation of sound propagation of four-time intervals in the y-z plane.

D

Appendix 4: Deep Water

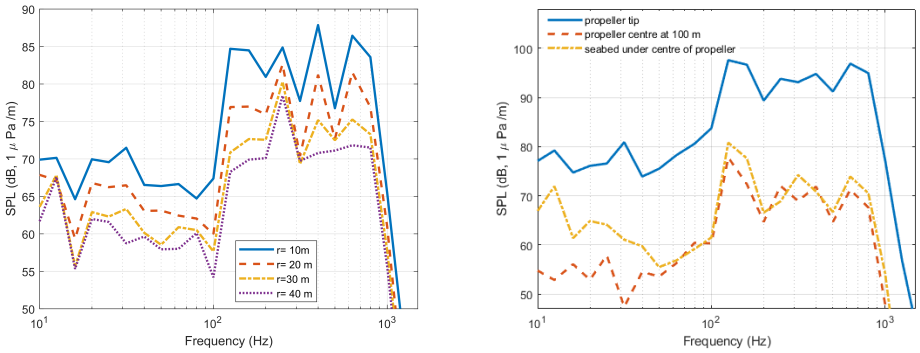

Figure D.1: Sound pressure levels of deep water simulation for additional points in 1/3 bands.

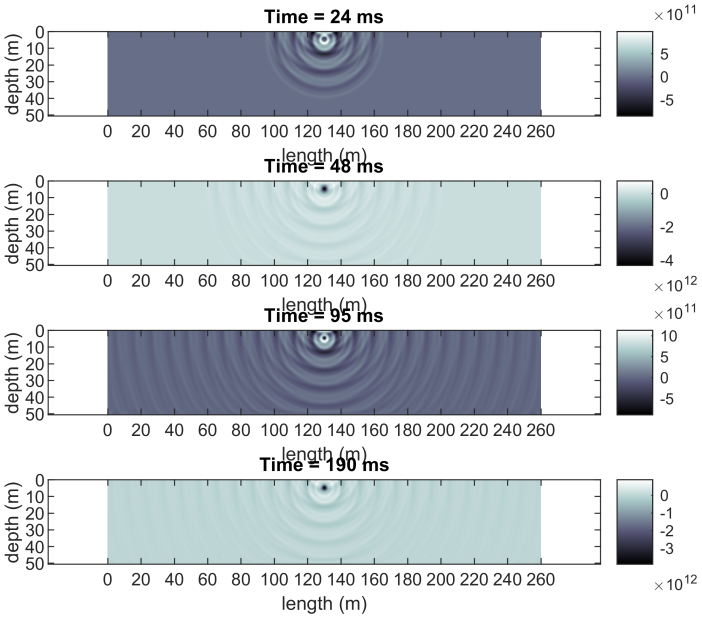

Figure D.2: Deep Water; visualisation of sound propagation of four-time intervals in the x-z plane.

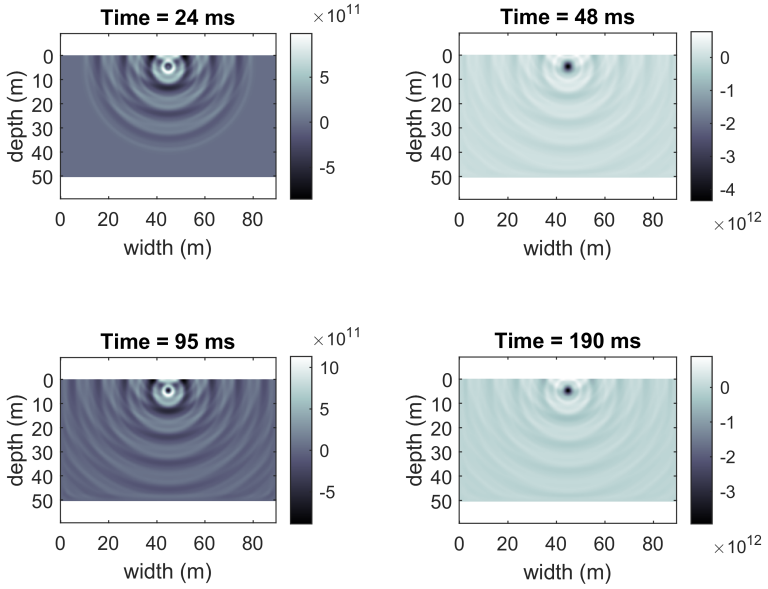

Figure D.3: Deep Water; visualisation of sound propagation of four-time intervals in the y-z plane.

E

Appendix 5: Canal with fully reflective retaining walls

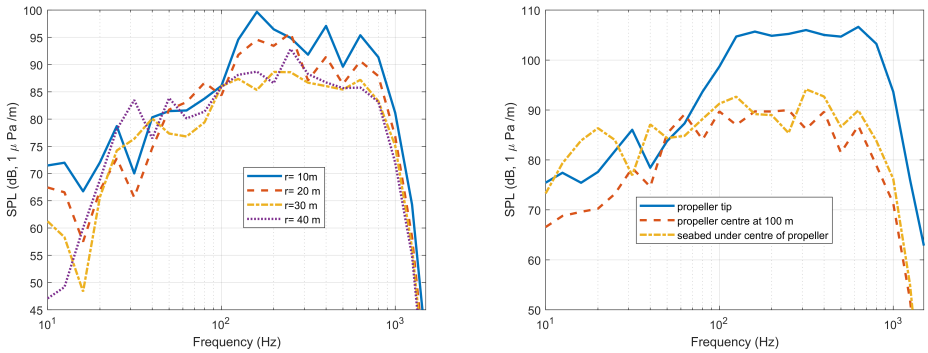

Figure E.1: Canal with fully reflective retaining walls; Sound pressure levels for additional points in 1/3 bands.

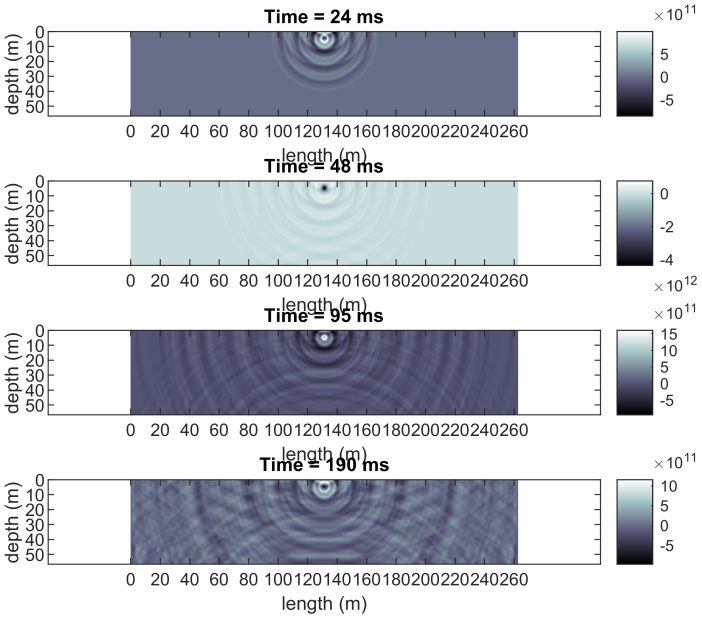

Figure E.2: Canal with fully reflective retaining walls; visualisation of sound propagation of four-time intervals in the x-z plane.

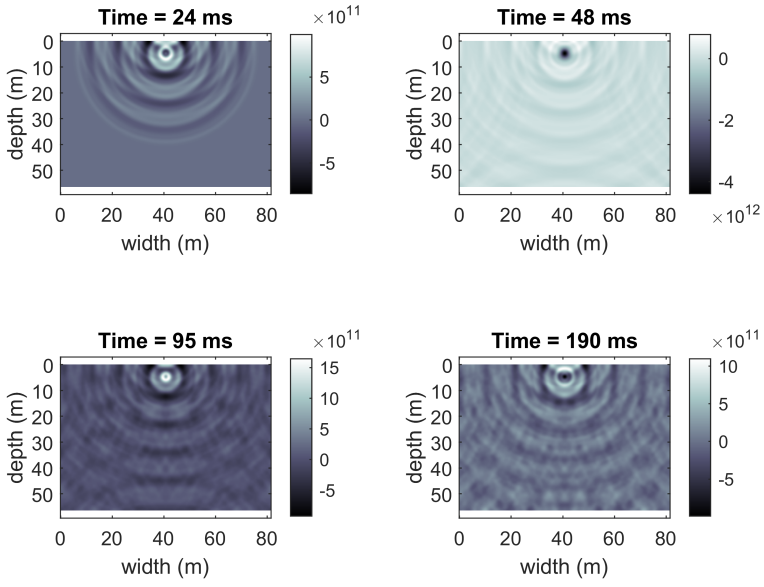

Figure E.3: Canal with fully reflective retaining walls; visualisation of sound propagation of four-time intervals in the y-z plane.

F

Appendix 6: Canal with sediment walls

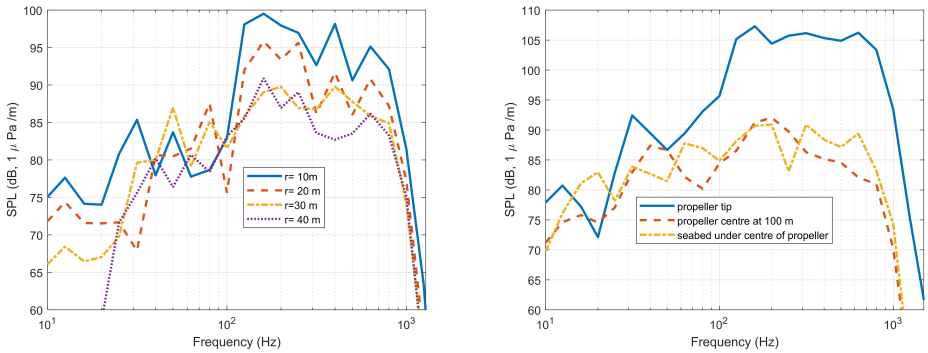

Figure F.1: Canal with sediment walls; Sound pressure levels for additional points in 1/3 bands.

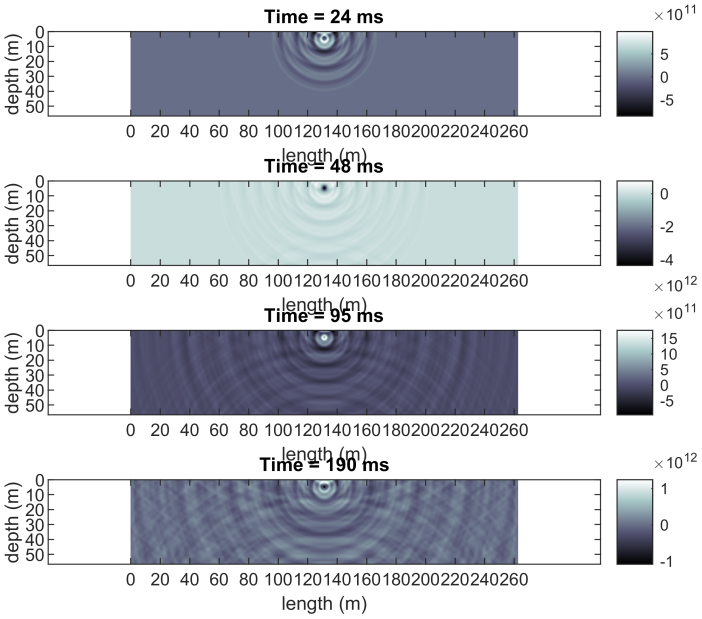

Figure F.2: Canal with sediment walls; visualisation of sound propagation of four-time intervals in the x-z plane.

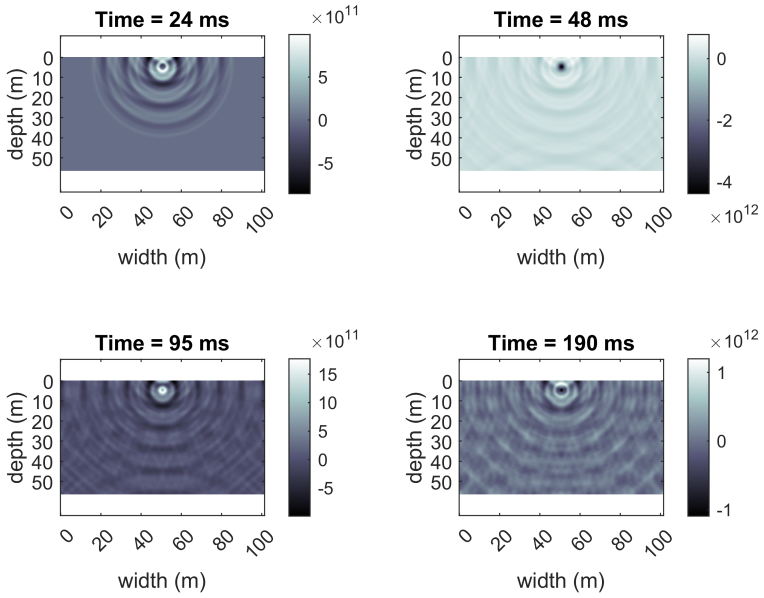

Figure F.3: Canal with sediment walls; visualisation of sound propagation of four-time intervals in the y-z plane.

G

Appendix 7: Canal with sediment walls and various water properties

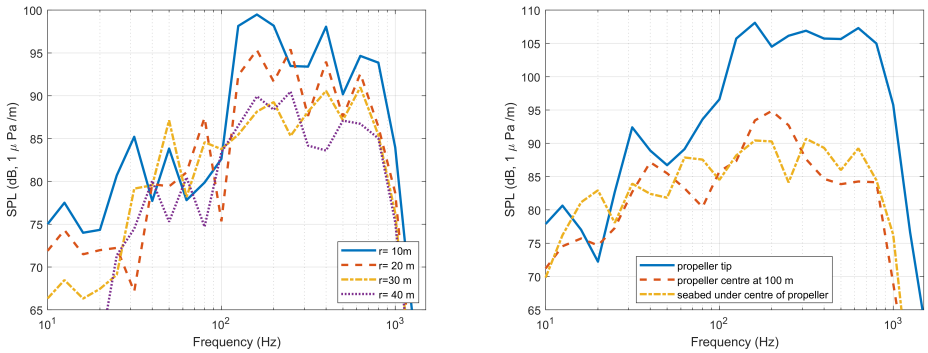

Figure G.1: Canal with sediment walls and various water properties; Sound pressure levels for additional points in 1/3 bands.

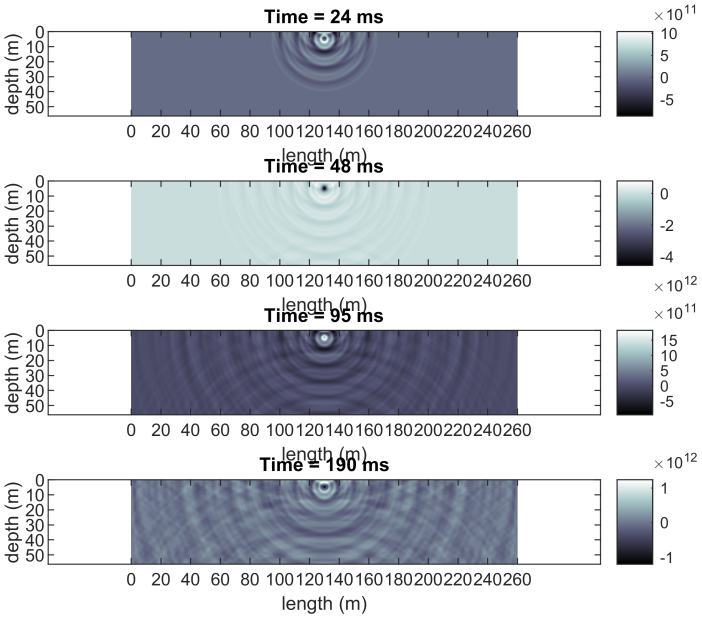

Figure G.2: Canal with sediment walls and various water properties; visualisation of sound propagation of four-time intervals in the x-z plane.

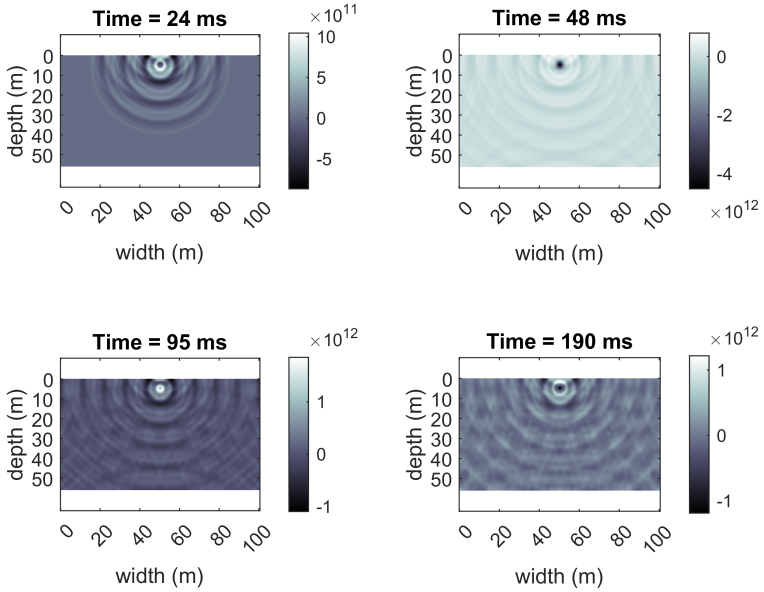

Figure G.3: Canal with sediment walls and various water properties; visualisation of sound propagation of four-time intervals in the y-z plane.

DEPARTMENT OF APPLIED ACOUSTIC
CHALMERS UNIVERSITY OF TECHNOLOGY
Gothenburg, Sweden
www.chalmers.se

CHALMERS
UNIVERSITY OF TECHNOLOGY